

UNIVERSITY OF CALIFORNIA

Santa Barbara

Molecular Assembly and Device Physics of High-Mobility Organic Field-Effect Transistor

Fabricated from Donor-Acceptor Copolymers

A dissertation submitted in partial satisfaction of the  
requirements for the degree Doctor of Philosophy  
in Chemistry

by

Hung Phan

Committee in charge:

Professor Thuc-Quyen Nguyen, Chair

Professor Guillermo C. Bazan

Professor Steven Buratto

Professor Bradley F. Chmelka

June 2016

The dissertation of Hung Phan is approved.

---

Guillermo C. Bazan

---

Steven Buratto

---

Bradley F. Chmelka

---

Thuc-Quyen Nguyen, Committee Chair

May 2016

Molecular Assembly and Device Physics of High-Mobility Organic Field-Effect Transistor  
Fabricated from Donor-Acceptor Copolymers

Copyright © 2016

by

Hung Phan

## ACKNOWLEDGEMENTS

Firstly, I would like to express my gratitude for all the supports, advices and encouragements of my advisor - Professor Thuc-Quyen Nguyen. Prof. Nguyen works very hard to make sure that we have all the necessary resources to do research in the lab. She also often introduces me to many experts in the field of organic electronics so that I can discuss the science and ask them for advices. I also highly appreciate Prof. Nguyen for establishing an incredible atmosphere in the lab, by recruiting kind, smart, dedicated and hard-working lab members.

I am also grateful to Dr. Ming Wang and Professor Guillermo Bazan for the collaboration that makes this thesis work possible, especially for kindly providing the materials with high purity for all the study in the thesis. The thesis work belongs to a bigger project (IRP9) funded by Mitsubishi Chemicals Center for Advanced Materials (MC-CAM). I appreciate MC-CAM for financially supporting me in the last four years, giving me the opportunity to go to several conferences to share my research to the community. I truly value all the constructive and informative discussion with the researchers of IRP9, especially with Dr. Ming Wang, Dr. Mike Tseng, Michael Ford, Alexander Lill and Tyler Postle from UCSB and Dr. Akira Ohno, Dr. Tomohide Murase from Mitsubishi Chemical Research Center. I also want to thank the PIs of IRP9, Professor Thuc-Quyen Nguyen, Professor Guillermo Bazan, Professor Edward Kramer, Professor Alan Heeger and Professor Rachel Segalman, for all the fruitful discussions and brainstorming.

I am very thankful for all the help, critic, and kind treat of my labmates. They no doubt make my life at UCSB more useful and joyful. Among them, I especially want to thank Dr. Xuan-Dung Dang, Dr. Peter Zalar, Dr. Oleksandr Miknenko, Dr. Martijn Kuik, Kenny Liao,

Sam Collins and Niva Ran for a great deal of insightful scientific chats and technical supports. I appreciate Peter for being a fun office-mate and for his confidence in my capability to overcome challenging research problems. Recently, mentoring Alex and Tyler really helps me a lot in re-thinking and re-evaluating several aspects of the research project. Despite of being their mentor, Alex and Tyler's hard work and enthusiasm greatly motivate me to work harder and think deeper. While I am focusing on writing this thesis, Alex, Tyler and Michael Ford cover for me some of my research work and group responsibilities, for which I highly appreciate.

I am very glad to have Professor Bradley Chmelka and Professor Steven Buratto in my PhD thesis committee. They gave me many critical comments and suggestions during my candidacy exam and annual committee meeting. I am especially grateful to Professor Chmelka for his recommendations for some of my award applications.

I want to have a special thank for my wonderful wife, Huyen Nguyen, for sharing with me all the happiness and sadness in the last five years in the US. With the graciousness and tolerance, Huyen inspire me studying harder and living nicer. I remain indebted to my parents, my two younger brothers, family members in Binh Dinh, Viet Nam for supporting me in any circumstance.

Finally, I would like to thank all of my friends for their help, support. Thanks Tung for crossing more than 2000 miles from Chicago to visit me several times; and travel with me to many interesting places. Thanks the Vietnamese Students at UCSB for giving me a homeland-like life of an international student sometimes.

For any error or inadequacy that may remain in this work, the responsibility is entirely my own.

VITA OF HUNG PHAN  
May 2016

**EDUCATION**

- 2011-present **PhD in Materials Chemistry**, University of California, Santa Barbara (UCSB); Advisor: Prof. Thuc-Quyen Nguyen; GPA 3.88/4
- 2007-2009 **MS in Environmental Engineering**, Gwangju Institute of Science and Technology (GIST); Advisor: Prof. Seung Hyeon Moon; GPA 4.41/5
- 2002-2006 **BS with Honors in Chemistry**, Hanoi University of Science (HUS); GPA 8.83/10

**PROFESSIONAL EMPLOYMENT**

**2011-present, Graduate Student Researcher and Teaching Assistant at UCSB**

- Designed experimental setup and investigated  $\mu\text{m}$ -scale charge transport mechanism of electrically conductive microbial biofilms.
- Fabricated high-mobility polymer field-effect transistors (PFETs) and elucidated their molecular assembly, charge transport mechanism and electrical instability via I-V measurement and high-resolution AFM.
- Designed, optimized and characterized advanced hybrid materials for solar cells and photodetectors: conducting and photoconducting AFM (c-AFM, pc-AFM), TOF-SIM, UV-VIS absorption.
- Interpreted the structure-property relationship of  $\text{TiO}_2$ -graphene composite anode used in dye-sensitized solar cells; and dopant distribution in molecular-doped organic semiconductors using c-AFM and pc-AFM.
- Four-year of experience in clean-room: Photolithography, E-beam, ALD, sputtering, dicing.
- Collaborators: Prof. Guillermo Bazan, Prof. Alan Heeger, Prof. Bradley Chmelka, Prof. Craig Hawker, Prof. Rachel Segalman, Prof. Alberto Salleo (Stanford), Prof. Timothy Tan (NTU, Singapore), Mitsubishi Chemical Research Center, Dr. Leonard Tender (Naval Research Lab.).

**2010-2011, Quality Production Leader, Decathlon Vietnam**

- Managed the development and quality-control of skiing jackets and pants from  $I_d\epsilon\text{as}$  to mass production.
- Determined chemical compatibility of fabrics as the cause of color staining problems of mixed color jackets.

**2007-2010, R&D and Graduate Student Researcher at GIST**

- Developed and validated a program that accurately predicts boron rejection through

reverse osmosis (RO) membranes: RO module, absorption column, ICP-MS, ICP-OES, IC.

- Resolved organic fouling mechanism of RO membranes at molecular level via HPLC-MS<sup>n</sup>, NMR, ATR-FTIR.
- Collaborators: Prof. Joon Ha Kim, Prof. In Soo Kim, Dr. Shaoyuan Shi (CAS, China).

### **2005-2007, Researcher at Centre for Environmental Technology and Sustainable Development at HUS**

- Studied air pollution caused by volatile organic compounds (VOCs) in Hanoi: gas sampling, titration, GC-MS.
- Operated and trouble-shot membrane-supported bioreactor (MBR) pilot for wastewater treatment.

## **PUBLICATIONS & ORAL PRESENTATIONS**

### **Peer-reviewed papers**

1. **H. Phan**, M. Wang, M. J. Ford, A. Lill, G. C. Bazan, T.-Q. Nguyen, Mechanistic Study and Generalization of the Electron-Trapping-Induced Instability of p-type Field-Effect Transistors Fabricated from Low Band-gap Polymers, **in preparation (2016)**
2. **H. Phan**, T. Postle, A. Lill, M. Wang, M. J. Ford, G. C. Bazan, T.-Q. Nguyen, Polymer Chain Alignment and Its Impacts on Charge Transport in Field-Effect Transistors, **in preparation (2016)**
3. **H. Phan**, M. M. D. Yates, N. D. Kirchhofer, G. C. Bazan, L. M. Tender, and T.-Q. Nguyen, Biofilm as a redox conductor: a systematic study of moisture and temperature dependence of its electrical properties, *Phys. Chem. Chem. Phys.*, **accepted (2016)**.
4. M. J. Ford, M. Wang, **H. Phan**, T.-Q. Nguyen, G. C. Bazan, Fullerene Additives Convert Ambipolar Transport to p-Type Transport while Improving the Operational Stability of Organic Thin Film Transistors, *Adv. Funct. Mater.*, **accepted (2016)**.
5. M. Wang, M. J. Ford, **H. Phan**, J. Coughlin, T.-Q. Nguyen, G. C. Bazan, Fluorine substitution influence on benzo[2,1,3]thiadiazole based polymers for field-effect transistor applications, *Chem. Commun.* 52, 3207-3210 **(2016)**.
6. M. J. Ford, M. Wang, S. N. Patel, **H. Phan**, R. A. Segalman, T.-Q. Nguyen, G. C. Bazan, High Mobility Organic Field-Effect Transistors from Majority Insulator Blends, *Chem. Mater.* 28, 1256-1260 **(2016)**.
7. C.-Y. Chiu, H. Wang, **H. Phan**, S. Kazuya, T.-Q. Nguyen, C. J. Hawker, Twisted olefinic building blocks for low bandgap polymers in solar cells and ambipolar field-effect transistors, *J. Polym. Sci. Part A: Polym. Chem.* 54, 889-899 **(2016)**.

8. **H. Phan**, M. Wang, G. C. Bazan, T.-Q. Nguyen, Electrical Instability of p-type Field-Effect Transistors from Low Band-gap Donor-Acceptor Polymer Induced by Electron Trapping, *Adv. Mater.* 27, 7004–7009 (2015).
9. H.-R. Tseng, **H. Phan**, C. Luo, M. Wang, L. A. Perez, S. N. Patel, L. Ying, E. J. Kramer, T.-Q. Nguyen, G. C. Bazan, A. J. Heeger, High-Mobility Field-Effect Transistors Fabricated with Macroscopic Aligned Semiconducting Polymers. *Adv. Mater.* 26, 2993–2998 (2014).
10. **H. Phan**, J. P. Jahnke, B. F. Chmelka, T.-Q. Nguyen, Structural and optoelectronic properties of hybrid bulk-heterojunction materials based on conjugated small molecules and mesostructured TiO<sub>2</sub>. *Applied Physics Letters*. 104, 233305 (2014).
11. D. T. Duong\*, **H. Phan\***, D. Hanifi, P. S. Jo, T.-Q. Nguyen, A. Salleo, Direct Observation of Doping Sites in Temperature-Controlled, p-Doped P3HT Thin Films by Conducting Atomic Force Microscopy (c-AFM). *Adv. Mater.* 26, 6069–6073 (2014). (\* *equal contribution*)  
*H. Phan performed c-AFM and analyzed data; D. T. Duong prepared films and performed other tests.*
12. Y. Li, C.-K. Mai, **H. Phan**, X. Liu, T.-Q. Nguyen, G. C. Bazan, M. B. Chan-Park, Electronic Properties of Conjugated Polyelectrolyte/Single-Walled Carbon Nanotube Composites. *Adv. Mater.* 26, 4697–4703 (2014).
13. Z. Li, J. D. A. Lin, **H. Phan**, A. Sharenko, C. M. Proctor, P. Zalar, Z. Chen, A. Facchetti, T.-Q. Nguyen, Competitive Absorption and Inefficient Exciton Harvesting: Lessons Learned from Bulk Heterojunction Organic Photovoltaics Utilizing the Polymer Acceptor P(NDI2OD-T2). *Adv. Funct. Mater.* 24, 6989–6998 (2014).
14. Y. Zhang, M. Wang, S. D. Collins, H. Zhou, **H. Phan**, C. Proctor, A. Mikhailovsky, F. Wudl, T.-Q. Nguyen, Enhancement of the Photoresponse in Organic Field-Effect Transistors by Incorporating Thin DNA Layers. *Angew. Chem. Int. Ed.* 53, 244–249 (2014).
15. J. Liu, Y. Zhang, **H. Phan**, A. Sharenko, P. Moonsin, B. Walker, V. Promarak, T.-Q. Nguyen, Effects of Stereoisomerism on the Crystallization Behavior and Optoelectrical Properties of Conjugated Molecules. *Adv. Mater.* 25, 3645–3650 (2013).
16. Z. He\*, **H. Phan\***, J. Liu, T.-Q. Nguyen, T. T. Y. Tan, Understanding TiO<sub>2</sub> Size-Dependent Electron Transport Properties of a Graphene-TiO<sub>2</sub> Photoanode in Dye-Sensitized Solar Cells Using Conducting Atomic Force Microscopy. *Adv. Mater.* 25, 6900–6904 (2013). (\* *equal contribution*)  
*H. Phan performed c-AFM and analyzed data; Z. He prepared graphene-TiO<sub>2</sub> anode and performed other tests.*



17. **H. Phan**, B.-S. Oh, B. X. Tung, S.-G. Oh, K.-S. Kim, K.-J. Kim, S.-H. Moon, I. S. Kim, A. Jang, Reflection of the structural distinctions of source—different humic substances on organic fouling behaviors of SWRO membranes. *Desalination*. 318, 72–78 (2013).
18. **H. Phan**, S.-H. Cho, J.-J. Woo, S.-H. Moon, Behaviors of commercialized seawater reverse osmosis membranes under harsh organic fouling conditions. *Desalination and Water Treatment*. 15, 48–53 (2010).
19. B.-C. Kim, **H. Phan**, S.-H. Moon, Boron removal from seawater by combined system of seawater reverse osmosis membranes and ion exchange process: a pilot-scale study. *Desalination and Water Treatment*. 15, 178–182 (2010).
20. S. Shi, Y.-H. Lee, S.-H. Yun, **H. Phan**, S.-H. Moon, Comparisons of fish meat extract desalination by electrodialysis using different configurations of membrane stack. *Journal of Food Engineering*. 101, 417–423 (2010).
21. **H. Phan**, S.-H. Cho, S.-H. Moon, Prediction of boron transport through seawater reverse osmosis membranes using solution–diffusion model. *Desalination*. 247, 33–44 (2009).

### Patent

Chien-Yang Chiu, Hengbin Wang, **Hung Phan**, Fulvio G. Brunetti, Craig J. Hawker, and Fred Wudl, United States Patent: US 14/589,798, Building block for low bandgap conjugated polymers.

### Oral Presentations

1. Transport Characteristics of Fullerene:Polymer Blend OFETs & Polymer Alignment by Mechanical Rubbing, Annual Review, Mitsubishi Chemical - Center for Advanced Materials, UC Santa Barbara, USA, May, 2016.
2. Understanding Electron-Induced Instability of p-Type Field-Effect Transistors fabricated from Low Band-Gap Donor-Acceptor Polymers, MRS Spring Meeting, Phoenix, USA, April, 2016.
3. Electrical Instability of p-type Field-Effect Transistors from Low-Bandgap Donor–Acceptor Polymer Induced by Electron Trapping, F $\pi$ - 12, Seattle, USA, July, 2015.
4. Understanding nanoscale morphological and electrical properties of molecular-doped organic semiconductor films by conducting atomic force microscopy, F $\pi$ - 12, Seattle, USA, July, 2015.
5. Understanding Electrical Stability in High Mobility p-type Polymer FETs, Annual Review, Mitsubishi Chemical - Center for Advanced Materials, UC Santa Barbara, USA, April, 2015.

6. Molecular Assembly and Charge Transport in High-Mobility Polymer Field-Effect Transistor, Chemical Sciences Student Seminar, UC Santa Barbara, USA, October 20, **2014**.
7. Understanding Molecular Assembly and Charge Transport in High Mobility p-type Polymer FETs, Oral Presentation, Annual Review, Mitsubishi Chemical - Center for Advanced Materials, UC Santa Barbara, USA, April, **2014**.
8. Structural and optoelectronic properties of hybrid bulk-heterojunction materials based on conjugated small molecules and mesostructured TiO<sub>2</sub>, 11th International Symposium on Functional  $\pi$ -electron systems, Arcachon, France, June 2-7, **2013**.
9. Complete prediction of reverse osmosis performance using solution-diffusion transport theory, The 1st IWA Asia- Pacific Young Water Professionals Conference, Gwangju, Korea, December 8-10, **2008**.
10. Assessing the air-polluted level caused by volatile organic compounds in Hanoi, Joint workshop "Vision for international study in higher education for 2020", HUS-GIST-UOG, Hanoi, **2007**.

#### **AWARDS & SCHOLARSHIP**

- 2016 Mananya Tantiwivat Fellowship Award, UCSB
- 2015 Dissertation Fellowship, UCSB
- 2015 First Prize, Art of Science Competition, UCSB
- 2014-2016: Materials Research Laboratory (MRL) Travel Fellowship, UCSB
- 2013 UCSB Doctoral Student Travel Grant
- 2010 Winner of Green Talents, Federal Ministry of Education and Research, Germany
- 2007-2009: POSCO Asia Fellowship for Master student, POSCO, Korea
- 2006 Chancellor Certificate for Outstanding Graduates, HUS
- 2005 Scholarship of Rencontres du Vietnam, France
- 2002-2006: Vietnamese government full scholarship for undergraduate students in Honors Program, HUS
- 2003, 2004: Distinguished Youth of Vietnam National University, Hanoi
- 2003 Third prize in National Chemistry Olympiad for undergraduate students
- 2001, 2002: First and second prize in National Contest for high-school student in chemistry

#### **COMMUNICATION, MANAGEMENT & OTHER SKILLS**

**Technical writing:** 19 papers in top-tier scientific journals, 5 Research proposals.

**Mentoring:** 3 PhD students, 1 MS student, 2 BS students

**Teaching:** General, Organic, and Advanced Analytical chemistry labs

**Computer and Programming:** FORTRAN, C, Mathematica, Igor, OriginLab, AutoCAD, Office

**Management and Leadership:** Manager of the probe station and three AFM systems in the lab; Managed three garment factories for Decathlon; Coordinator of Vietnamese students at GIST, Coordinator of Chemistry Youth Club at HUS.

**Volunteering:** DCB Student Recruitment Committee; Elementary school science outreach (MRL-UCSB); Family Ultimate Science Exploration (FUSE) for Junior high school (CNSI-UCSB); Judge of Santa Barbara County Science Fair for high school students; UCSB Beyond Academia Programming Committee; National Nano Days Festival, Santa Barbara.

## ABSTRACT

Molecular Assembly and Device Physics of High-Mobility Organic Field-Effect Transistor  
Fabricated from Donor-Acceptor Copolymers

by

Hung Phan

The Field Effect Transistor (FET) is inarguably the most important circuit element in modern electronics. Metal-Oxide FETs (MOSFETs), the most common type of FET, are integrated in microprocessors in almost all electronic devices: mobile phones, computers, digital cameras, and digital printers, to name a few. MOSFETs are normally fabricated on top of rigid single crystalline silicon, which requires high temperature processing (~1000 °C). Recently, a need has emerged for flexible electronics in a variety of applications. Examples include form-fitting healthcare-monitoring devices, flexible displays, and flexible radio frequency identification tags (RFID). Organic FETs (OFETs) are viable candidates for flexible electronics because they are based on semiconducting  $\pi$ -conjugated materials, including small molecules and polymers, which can be solution-processed at low temperature on flexible substrates. Solution-processing may enable the use of high throughput methods such as roll-to-roll coating and inkjet printing for low-cost manufacturing. In the molecular perspective, the limitless ability to tune the properties of these materials just by a small modification of the conjugated backbone or sidechains makes them attractive to both academic research and industrial manufacturing. Between the two

materials, semiconducting polymers offer better potential for the formation and mechanical properties of thin films, compared to their small molecule counterparts.

For OFETs to be industrially viable, however, they must first have high charge carrier mobility. Recent advances in molecular designs and device engineering have seen significant increases in the mobility of OFETs fabricated with conjugated polymer (or PFETs). In this dissertation, it is shown that obtaining polymer-chain alignment is critical to improve the mobility of PFETs. In addition, the charge transport mechanism is investigated to explain the high mobility in PFETs with aligned polymers. Most importantly, the mechanism of electrical instability and non-ideality (i.e. the double-slope) of high mobility PFETs with a certain degree of ambipolarity is unraveled.

Firstly, the alignment of polymer chains inside polymer fiber bundles is revealed by high-resolution atomic force microscopy (AFM). This alignment is enabled by nano-grooves of ca. 50 nm wide and 2-5 nm deep on SiO<sub>2</sub> substrates used for fabricating the PFETs. Mobility of charge transport along the direction of the polymer fiber is an order of magnitude higher than that of charge transport perpendicular to the fiber direction. It indicates that aligned polymer chains facilitate fast intrachain charge transport.

Secondly, the charge transport mechanism is determined to be the thermally-activated hopping of charge carriers. This is an important finding because it has been speculated that band transport is possible in OFETs fabricated from well-aligned polymer fibers. With a normal range of molecular weight (30 kDa to 100 kDa), which is feasible for industrial scale-up, the stretched length of the corresponding polymer chain, ranging from 50 – 150 nm, is not enough to cross the full channel length of the OFETs. In addition, polymer chains in a solution-processed thin film are likely to have kinks and twists that disrupt the perfect electronic coupling necessary for band transport. It implies that polymers should be designed

to facilitate not only chain alignment but also the strong electronic coupling in the  $\pi$ - $\pi$  stacking direction between chains for efficient hoppings between chains with low energetic barriers.

Finally, the electrical instability and its associated non-ideal device characteristics is thoroughly investigated. Electrical stability is as important as high charge carrier mobility for OFETs to be commercialized in large-scale production. The use of low bandgap donor-acceptor (D-A) polymers for obtaining high mobility introduces undesirable electron current in p-type PFETs. The effect of electron transport and trapping on hole conduction in p-type OFETs has not been addressed. In this work, p-type PFETs fabricated with SiO<sub>2</sub> dielectrics and with a certain degree of ambipolarity exhibit electrical instability (a change in current upon bias stressing) and non-ideality (double-slope in transfer curves) of hole current. It is determined that electron trapping and the subsequent formation of  $-\text{SiO}^-$  charges on SiO<sub>2</sub>/polymer interface are the principle origins of the instability and the double-slope. Suppressing these undesired properties is essential to make PFETs industrial viable. It should be noted that the double-slope has been a long debate without a solid explanation in the OFET research community.

In sum, this thesis shows a comprehensive understanding of the structure-processing-property relationship of PFETs fabricated with well-aligned polymers. New findings in the thesis provide important guidelines for molecular design and device engineering of high-mobility and practical PFETs. These guidelines have been successfully demonstrated by us and our collaborators at UCSB.

## TABLE OF CONTENTS

ACKNOWLEDGEMENT.....	iii
VITA OF HUNG PHAN .....	vi
ABSTRACT .....	xii
TABLE OF CONTENTS.....	xv
LIST OF FIGURES.....	xix
1. Introduction.....	1
1.1. Organic Field-Effect Transistors (OFETs) .....	1
1.2. Working Principles and Figures of Merits of OFETs.....	5
1.3. Organic Semiconductors for OFETs.....	10
1.3.1. Semiconducting Conjugated Organic Materials .....	10
1.3.2. Donor-Acceptor (D-A) Conjugated Polymers for OFETs .....	14
1.4. Charge Transport and Charge Injection in OFETs .....	15
1.4.1. Charge Transport.....	15
1.4.2. Charge Trapping and Device Instability .....	17
1.4.3. Charge Injection .....	18
1.5. Motivation and Structure of the Thesis .....	19
1.6. Characterizations of Organic and Hybrid Materials .....	20
2. Materials and Experimental Methods .....	23
2.1. Semiconducting Polymers .....	23
2.2. OFET Fabrication .....	24
2.3. Electrical measurements of OFET .....	26
2.4. Programming for current transient measurements.....	27

2.5.	Atomic Force Microscopy .....	27
3.	Device Performance and Polymer Alignment of PCDTPT at Different Molecular Weights	29
3.1.	Introduction.....	29
3.2.	Device Performance and Mobility Anisotropy .....	32
3.3.	Polymer Chain Alignment of PCDTPT by High-Resolution AFM.	34
3.4.	Polymer Chain Alignment of PCDTPT by Transmission Electron Microscopy .....	42
3.5.	Conclusion .....	43
4.	Thermally Activated Charge Transport in High-mobility OFETs Fabricated from D-A Polymers .....	44
4.1.	Introduction.....	44
4.2.	Water effect in the analysis of temperature-dependent measurements	45
4.3.	Investigating Activation Energy by Temperature-dependent Measurements	47
4.4.	Characterizing Molecular Stacking by GIWAXS.....	52
4.5.	Conclusion .....	54
5.	Electrical Instability and Non-ideality of OFETs Fabricated from Low Band-gap Polymers	55
5.1.	Introduction.....	55
5.2.	Electrical Instability and Double-Slope of PCDTPT FETs .....	57
5.3.	Electron-Trapping-Induced Electrical Instability and Double-Slope	61
5.4.	Reduction of Electron Trapping at Low Temperature .....	65
5.5.	Mechanism of the Double Slope.....	67



5.6.	Generalization of Electrical Instability and Double-slope.....	70
5.7.	Conclusion.....	74
6.	Suppressing Electrical Instability and Double-Slope by Molecular Design and Device Engineering.....	76
6.1.	Introduction.....	76
6.2.	Utilizing non SiO <sub>2</sub> dielectric materials.....	76
6.2.1.	Suppressing Electron Trapping with BCB dielectric.....	76
6.2.2.	Conclusion & Future Work.....	78
6.3.	New Material Design and Characterization for Suppressing the Electrical instability and Non-ideality while Maintaining High Mobility.....	79
6.3.1.	Design Principles for Inhibiting Electron Injection.....	79
6.3.2.	Improved Device Stability and Ideality in PCDTBTA FETs..	80
6.3.3.	Conclusion & Future Work.....	83
6.4.	Suppressing Electron Transport in Ambipolar PFETs by an Electron Acceptor.....	84
6.4.1.	Suppressing Electron Transport by and Electron Acceptor and Working Hypothesis.....	84
6.4.2.	Uninterrupted Hole Transport of PCDTPT in PCDTPT:PCBM and PCDTPT/C60 devices.....	85
6.4.3.	Electron Transfer from PCDTPT to PCBM and C60.....	88
6.4.4.	Lateral Electron Transport in C60 Layer in PCDTPT/C60 Devices	92
6.4.5.	Conclusion.....	94
7.	Conclusion & Outlook.....	95
7.1.	Conclusion.....	95

7.2.	Outlook .....	96
8.	References.....	100
9.	Appendix.....	118
9.1.	New program to measure the hole current dynamic under different bias stresses at different time intervals.....	118
9.2.	Structural and optoelectronic properties of hybrid bulk-heterojunction materials based on conjugated small molecules and mesostructured TiO <sub>2</sub>	120
9.2.1.	Introduction .....	120
9.2.2.	Material Fabrication and Small Molecule Loading Calculations	123
9.2.3.	Results and Discussions .....	127
9.2.4.	Conclusion .....	133
9.2.5.	References .....	134

## LIST OF FIGURES

- Figure 1.1. Four geometrical structures of thin-film transistors: (a) bottom-gate bottom-contact (BGBC); (b) bottom-gate top-contact (BGTC); (c) top-gate top-contact (TGTC) and (d) top-gate bottom-contact (TGBC). .....3
- Figure 1.2. The evolution of charge carrier mobility of OFETs, in comparison to three most used materials in FETs: single crystal silicon, polycrystalline silicon and amorphous silicon.....4
- Figure 1.3. Charge accumulation in linear regime and accumulation regime of an OFET with an undoped organic semiconductor .....6
- Figure 1.4. Typical transfer curves in (a) linear regime and (b) saturation regime (b); and (c) output curves of a p-type OFET.....9
- Figure 1.5. (a) Chemical structure of trans-polyacetylene; (b) the orientation and delocalization of 2p orbitals in the normal plane to the  $\sigma$ -skeleton of polyacetylene; and (c) schematic diagram of hole transport in an oligo-acetylene: hole is introduced to the molecule by removing an electron from the fifth carbon (via doping for example), then migrated along the backbone through the reorganization of 2p orbitals..... 11
- Figure 1.6. The use of molecular orbital theory in  $\pi$ -conjugated materials to explain the formation of HOMO, LUMO and reduced band gap compared to insulating materials ..... 12
- Figure 1.7. Chemical structures of some organic semiconductors used in p-type OFETs. Adapted from Ref.<sup>56,59</sup> ..... 13
- Figure 1.8. Schematic diagram of the reduced reorganization of hole propagation in D-A copolymers, in comparison to D-D polymers. The partial charge in each conjugated

segment is subjected to less change in charge distribution hence less reorganization energy when it accommodates a charge (hole in this case). Adapted from Ref.<sup>36</sup>14

Figure 1.9. Gaussian density of states comprising of localized states with different energy level. Electrons spontaneously hop (or relax) from higher energy levels to lower energy levels. In order to hop to the higher energy level, external energy (thermal energy, electrical energy) is needed.....16

Figure 2.1. Molecular structure and regioregularity pattern of PCDTPT. The arrows are guides to the eye to highlight stereoregularity. ....23

Figure 2.2. The home-made scratching machine (A) and the resulting surface of SiO<sub>2</sub> after scratching (B) at scan size 2µm × 2µm.....24

Figure 2.3. Schematic of sandwich-casting technique to fabricate PFETs in the thesis26

Figure 3.1. The GPC data of different molecular weight polymers. The data was obtained by Dr. Ming Wang.<sup>117</sup> .....31

Figure 3.2. Mobility of PCDTPT OFETs after annealing at 200 °C. The mobility value and the value in parentheses represent mean and maximum values obtained from 10 independent OFETs. (A) Devices fabricated by drop casting. (B) Devices fabricated by slow drying in the tunnel-like configuration. The horizontal lines in the box denote the 25th, 50th, and 75th percentile values. The error bars denote the 5th and 95th percentile values. The open square inside the box denotes the mean value. (C) and (D) FET characteristics of PCDTPT with mobility of 23.7 cm<sup>2</sup>/Vs. (L = 80 µm, W = 1 mm): (C) transfer curves taken at V<sub>DS</sub> = -80 V (D) output curves taken at various V<sub>G</sub> (0~-40V).<sup>117</sup> .....33

Figure 3.3. Saturation mobility as a function of gate bias. The mobility is calculated from the local slope in the transfer curve at saturation regime  $I_{ds}^{1/2}$  versus  $V_g$  (equation 9).<sup>117</sup> 34

Figure 3.4. AFM images of the PCDTPT topography by drop cast with MW of (A) 300, (B) 160, (C) 80, (D) 50, and (e) 30 kDa. (f) Phase image of the film with MW of 30 kDa. Data was obtained by Dr. Hsin-Rong Tseng.....35

Figure 3.5. AFM images ( $1 \mu\text{m} \times 1 \mu\text{m}$ ) of PCDTPT topside morphology by slow-drying on nano-grooved substrates (with orientation): (A) MW=300 kDa and (B) MW=50 kDa. The height scale is 0 – 5 nm. Data was obtained by Dr. Hsin-Rong Tseng.<sup>117</sup>....36

Figure 3.6. AFM images of PCDTPT FET on nano-grooved substrates at scan size of (a, b)  $5 \mu\text{m}$ , (c, d)  $1 \mu\text{m}$  and (e, f) 250 nm; a, c, e are topography images; b, d, f are phase image. The height scale is 0 – 5 nm and the phase scale is 0 –  $20^\circ$ . .....37

Figure 3.7. (A) High resolution AFM ( $250 \text{ nm} \times 250 \text{ nm}$ ) topside morphology phase image of PCDTPT 300 kDa OFET. (B) The cross-section profile of the dashed line in (A). (C) Molecular structure and estimated size of PCDTPT. The length of one monomer is approximately 2.4 nm and the width (including the side chains) is approximately 1.5 nm. ....39

Figure 3.8. AFM images of (a) top surface and (b) bottom surface of 50 nm PCDTPT films in PFETs with high mobilities shown in Figure 3.2. ....40

Figure 3.9. (a-b) High resolution AFM image of bottom surface of a PCDTPT device with mobility  $\sim 12 \text{ cm}^2/\text{Vs}$  (MW 50 kDa, 0.25 mg/ml, sandwiched devices of nano-grooved substrate, anneal at 200 C in 8 minutes). (c) Section analysis of a line-cut of  $100 \text{ nm} \times 100 \text{ nm}$  showing full-width half-max (FWHM) of a peak (representing a single fiber) of  $\sim 2.5 \text{ nm}$ . .....41

Figure 3.10. Electron diffraction patterns (A) at 0° tilt and (B) at 70° tilt. (C) Bright field transmission electron micrograph showing elongated structures along the alignment direction. Data was obtained by Dr. Shrayesh Patel. <sup>117</sup> .....	42
Figure 4.1. Temperature-dependent mobility of PCDTPT FETs with and without heating (at 400 K in 7 hours) in high vacuum (<10 <sup>-6</sup> torr) .....	46
Figure 4.2. Threshold voltage shift as a function of temperature of PCDTPT FETs with and without heating (at 400 K in 7 hours) in high vacuum (<10 <sup>-6</sup> torr) .....	47
Figure 4.3. Transfer (at V <sub>d</sub> =-50V) curves of the 50 kDa PCDTPT PFET at different temperatures.....	48
Figure 4.4. Temperature-dependent mobility for the PCDPTP PFETs with MW of 50, 160, and 300 kDa. ....	49
Figure 4.5. Activation energy of three MW fractions of PCDTPT.....	50
Figure 4.6. (A) Grazing wide-angle X-ray scattering line profiles of PCDTPT films formed by drop casting. (B) Estimated crystallite correlation length of alkyl and $\pi$ - $\pi$ stacking. ....	53
Figure 5.1. (a) Transfer characteristics of the PCDTPT PFET at V <sub>d</sub> =-80V before and after bias-sweeping gate voltages from 20 V to -60 V in approximately 5 minutes (also called aging); (b) Gate-dependence saturation mobility extracted from I-V curves in (a); (c) and (d) Output curves before and after bias-sweeping effect. Device structure: Si/SiO <sub>2</sub> /Au/DTS/PCDTPT.....	57
Figure 5.2. N-type transfer curve at V <sub>d</sub> =+80V (left) and output curves (right) of spin-coated PCDTPT on normal SiO <sub>2</sub> dielectrics. ....	58

Figure 5.3. Transfer characteristics of the PCDTPT PFET at  $V_d=-80V$  before, after bias-sweeping gate voltages from 30 V to -40 V in approximately 10 minutes (also called aging); and recovery in 95 hours when the device is set at  $V_d=V_g=0V$ . After each recovery interval, the transfer curve was quickly obtained in 5 seconds and the device is set back to  $V_d=V_g=0V$  until the subsequent scan. Device structure:

Si/SiO<sub>2</sub>/Au/DTS/PCDTPT.....60

Figure 5.4. The effect of continuous bias-sweeping on transfer curves (a) and mobility (b) of spin-coated PCDTPT on normal SiO<sub>2</sub> dielectrics (at  $V_d=-80V$ ). .....61

Figure 5.5. (a) Effect of bias-sweeping at negative and positive  $V_g$  on transfer curves of PCDTPT FETs ( $V_d=-80V$ ); (b) Two transfer curves in (a) plotted in linear scale; (c) mobility extracted from two curves in (b). Device structure: Si/SiO<sub>2</sub>/Au/DTS/PCDTPT. ....62

Figure 5.6. (a) The transfer characteristics of the PCDTPT PFET at  $V_d=-80V$  before stressing and after stressing at fixed  $V_d=-80V$  and  $V_g=-40V$  or  $+30V$ ; and (b) Drain current decay during bias-stress in hole accumulation ( $V_g=-40V$ ) and electron accumulation ( $V_g=+30V$ ) regime. The arrow indicate the forward current and backward current of bias-sweeping. Device structure: Si/SiO<sub>2</sub>/Au/DTS/PCDTPT.....63

Figure 5.7. (a) Electron current decay from bias-stressing of PCDTPT FETs in electron accumulation regime ( $V_d=-80V$ ,  $V_g=+30V$ ) at different temperatures. Inset: current decay ratio  $((I_{d, initial} - I_{d, at 300s})/I_{d,initial})$  as a function of temperatures. (b) Transfer curves before and after bias-stress (in (a)) at different selected temperatures. Device structure: Si/SiO<sub>2</sub>/Au/DTS/PCDTPT, spin-coating on nano-grooved substrates.....67

Figure 5.8. (a) The transfer characteristics of the PCDTPT PFET at  $V_d=-80V$  before and after stressing at  $V_d=-80V$  and  $V_g=30V$ . The blue curve (before stressing) was scanned

from  $V_g=30V$  to  $V_g=-60V$ . The red curve (after stressing) was scanned from  $V_g=-60V$  to  $V_g=30V$ . (b) the gate-dependence saturation mobility extracted from I-V curves in (a). Device structure: Si/SiO<sub>2</sub>/Au/DTS/PCDTPT.....68

Figure 5.9. Hole/electron current dynamics of PCDTPT PFET: hole current at  $V_d=-80V$  and  $V_g=-40V$  for  $t=0-200s$ , followed by electron current at  $V_d=-80V$  and  $V_g=+30V$  for  $t=200-500s$ ; and finally hole current measured with a 0.5 second pulse bias  $V_d=-80V$  and  $V_g=-40V$  every 10 seconds. In between hole current measurements (10s), the device was stressed at either in electron accumulation regime ( $V_d=-80V$  and  $V_g=+30V$ ) or hole accumulation regime ( $V_d=-80V$  and  $V_g=-40V$ ). Device structure: Si/SiO<sub>2</sub>/Au/DTS/PCDTPT.....70

Figure 5.10. The transfer characteristics of the PtBTPDPP PFET at  $V_d=-80V$  before and after stressing at  $V_d=-80V$  and  $V_g=30V$ . The blue curve (before stressing) was scanned from  $V_g=30V$  to  $V_g=-60V$ . .....71

Figure 6.1. (a) Drain current decay from bias-stressing of top-contact PCDTPT FETs in electron accumulation regime at different dielectrics ( $V_d=-80V$ ,  $V_g=+30V$  for SiO<sub>2</sub>-DTS SAM and  $V_g=60V$  for SiO<sub>2</sub>-BCB to obtain comparable initial current); and (b) The transfer characteristics of the PCDTPT PFET at  $V_d=-80V$  before stressing and after bias-stressing. Device structure: Si/SiO<sub>2</sub>/DTS SAM or BCB/PCDTPT/Au. ....77

Figure 6.2. The effect of continuous bias-sweeping on transfer curves (a) and mobility (b) of spin-coated top-contact PCDTPT on normal SiO<sub>2</sub> dielectrics with DTS treatment (at  $V_d=-80V$ ). .....78

Figure 6.3. Design principle of PCDTBTA for inhibiting electron injection in OFETs. PCDTBTA was synthesized by Dr. Ming Wang. ....80



Figure 6.4. (a) Transfer characteristics of PCDTBTA FETs in saturation regime ( $V_d=-80V$ ) for the polymer alignment parallel (PARA) and perpendicular (Perp) to the grooves at three different conditions: as-prepared (as), annealed at 100 C in 8 minutes (Ann100) and annealing at 200 C in 8 minutes (Ann200); (b) output curves of an as-prepared parallel device.....81

Figure 6.5. (a) Transfer characteristics of PCDTBTA FETs in saturation regime ( $V_d=-80V$ ) at different conditions (same data as Figure 6.4a but in linear scale to get mobility); (b) Saturation mobilities of PCDTBTA FETs.....82

Figure 6.6. Consecutive transfer curves before and after bias-stressing in (a) log-linear plots and (b) linear-linear plots of PCDTBTA FETs in saturation regime ( $V_d=-80V$ ).83

Figure 6.7. Device structures used in PCDTPT:PCBM and PCDTPT/C60 study.....84

Figure 6.8. Working hypothesis of the improvement of PCDTPT FETs by the addition of PCBM .....85

Figure 6.9. Transfer curves of PCDTPT (P2), PCDTPT:PCBM blend and PCDTPT/C60 bilayer FETs.....86

Figure 6.10. Temperature-dependent mobility of PCDTPT (P2), PCDTPT:PCBM blend and PCDTPT/C60 bilayer FETs. ....87

Figure 6.11. Activation energy of FETs fabricated from PCDTPT:PCBM blend at different weight percentages of PCBM and PCDTPT/C60 bilayer with different thickness of PCDTPT (or P2) .....88

Figure 6.12. Schematic of charge separation at the interface of an electron donor (P2 in this case) and an electron acceptor (C60 or PCBM) upon illumination of visible light89

Figure 6.13. Transfer curves of the device to determine the drain and gate voltage for monitoring electron and hole current as a function of time while turning the light ON/OFF .....	90
Figure 6.14. Electron and hole current of PCDTPT FETs as a function of time while turning the light ON/OFF.....	91
Figure 6.15. Electron and hole current of PCDTPT:PCBM blend FETs as a function of time while turning the light ON/OFF.....	91
Figure 6.16. Electron and hole current of PCDTPT/C60 bilayer FETs as a function of time while turning the light ON/OFF.....	92
Figure 6.17. Electron current at positive biases (highlighted by the red line in (a)) plotting as a function of temperature (b) to estimate the activation energy of electron transport in C60 layer in PCDTPT/C60 bilayer FETs .....	93
Figure 6.18. Activation energy of electron transport in C60 layer in PCDTPT/C60 bilayer FETs and in C60 FETs. ....	94
Figure 7.1. Chemical structures of wide band gap CDT-Ph based polymers. ....	97
Figure 7.2. Schematic drawings showing the correlation between polymer molecular weight or polymer chain length and hopping frequency.....	98
Figure 9.1. SAXS patterns of mesostructured TiO <sub>2</sub> film (a) before and (b) after calcinations. ....	124
Figure 9.2. Nitrogen absorption (circles) and desorption (triangles) isotherms of mesostructured TiO <sub>2</sub> film, measured using a TriStar 3000 Micromeritics Gas Absorption Analyzer.....	124

Figure 9.3. Calibration curve of absorbance at 600 nm at different thicknesses of neat DPP(TBFu) <sub>2</sub> films. ....	125
Figure 9.4. SIMS traces of hybrid TiO <sub>2</sub> -DPP(TBFu) <sub>2</sub> drop-cast film. ....	126
Figure 9.5. SIMS traces of a hybrid TiO <sub>2</sub> -DPP(TBFu) <sub>2</sub> spin-coat film. The arrow indicates the approximate film thickness up to the interface determined by profilometry after the SIMS measurements. ....	127
Figure 9.6. Absorption spectra of neat DPP(TBFu) <sub>2</sub> and hybrid TiO <sub>2</sub> -DPP(TBFu) <sub>2</sub> . ....	129
Figure 9.7. Steady-state photoluminescence and transient photoluminescence (the inset) of neat DPP(TBFu) <sub>2</sub> and hybrid TiO <sub>2</sub> -DPP(TBFu) <sub>2</sub> .....	130
Figure 9.8. (a-f) Surface morphology, dark-current and photo-current images from conducting and photoconducting atomic force microscopy of (a, b, c) TiO <sub>2</sub> -P3HT film and (d, e, f) TiO <sub>2</sub> -DPP(TBFu) <sub>2</sub> film, respectively. (g-i) The morphology of neat P3HT (g), DPP(TBFu) <sub>2</sub> (h) and mesostructured TiO <sub>2</sub> (i).....	132

## 1. Introduction

In this chapter, fundamental knowledge of the thesis work is presented. Firstly, the history of organic field-effect transistors (OFETs) is introduced. It is then followed by the operating principles and figures of merits of OFETs. Next, the basic understanding of electrical conduction in organic semiconductors and the rationale of using donor-acceptor (D-A) copolymers in high mobility OFETs is briefed. Finally, the motivation and structure of the thesis is presented.

### *1.1. Organic Field-Effect Transistors (OFETs)*

A transistor is a three-terminal electronic device in which the electric current flow in a channel between two terminals (source and drain) can be turned ON/OFF or regulated by the third terminal (gate).<sup>1,2</sup> In 1926, Lilienfeld filed a patent proposing the principle of a field-effect transistor (FET) for the first time.<sup>3</sup> The concept of a transistor and the practical amplifier tryouts were further investigated by Lilienfeld, Shockley, Brattain and Bardeen.<sup>4-8</sup> In principle, an FET operates as a parallel-plate capacitor where one plate is a semiconducting channel between two contacts: source and drain. The density of charge carriers in the channel and hence the channel conductivity is modulated by an electric-field (field-effect) between the second plate of the capacitor, the gate electrode, and the channel.<sup>1,2</sup>

FETs can be constructed from various semiconductors, with silicon being by far the most common semiconductor used. Metal-Oxide-Semiconductor FETs (MOSFETs), which were successfully fabricated for the first time in 1960 by Kahng and Atalla,<sup>9</sup> is the most used FET today. With the advantages of using the well-developed silicon wafer fabrication and having the ultra-high charge carrier mobility of single crystal silicon, MOSFETs are indispensable

elements of high-accuracy and ultra-fast electronic devices such as microprocessors (chips) and memory devices.<sup>1</sup> The disadvantages of MOSFETs are the high-temperature fabrication and non-transparency of silicon wafer. Single crystal silicon wafers, atop which most MOSFETs are fabricated, require very high temperature (~1000 °C) for processing. Those prevent MOSFETs from being practical in applications that require special quality such as transparent substrates in display applications<sup>10,11</sup> or degradable substrates for transient electronics.<sup>12</sup> In these cases, thin-film transistors have been found to be more applicable.

Thin-film transistor (TFTs) are a type of FETs made by depositing a thin film of an active semiconductor layer as well as the dielectric layer and metallic contacts over a supporting substrate. Even though TFT was the first patented solid-state amplifier,<sup>4</sup> it only emerged in the 1970s as a candidate for forming very large area integrated circuits for flat panel displays.<sup>13–15</sup> A wide selection of supporting substrates made TFT attractive in a variety of applications. For instance, transparent substrates are used in TFTs that drive current in liquid-crystal display (LCD) and light-emitting diode (LED) display. Amorphous silicon and polycrystalline silicon are the two most common semiconductors used in commercialized TFTs.<sup>16,17</sup> Other inorganic semiconductors have also been used in TFTs such as ZnO,<sup>18–20</sup> Indium Gallium Zinc Oxide (IGZO).<sup>21,21,22</sup>

Organic field-effect transistors (OFETs) are basically TFTs using organic semiconductors as active layers. In parallel with the emerging of TFT using silicon, OFET was first described in the 1970s using metal-free phthalocyanine single crystals.<sup>23,24</sup> The major milestone came about when Koezuka and coworkers at Mitsubishi reported a working OFET using polythiophene, which belongs to a family of conducting polymers discovered in 1970s.<sup>25–28</sup> OFETs can be prepared either by vacuum evaporation of small molecules, by

solution-casting of polymers or small molecules, or by mechanical transfer of a peeled single-crystalline organic layer onto a substrate.

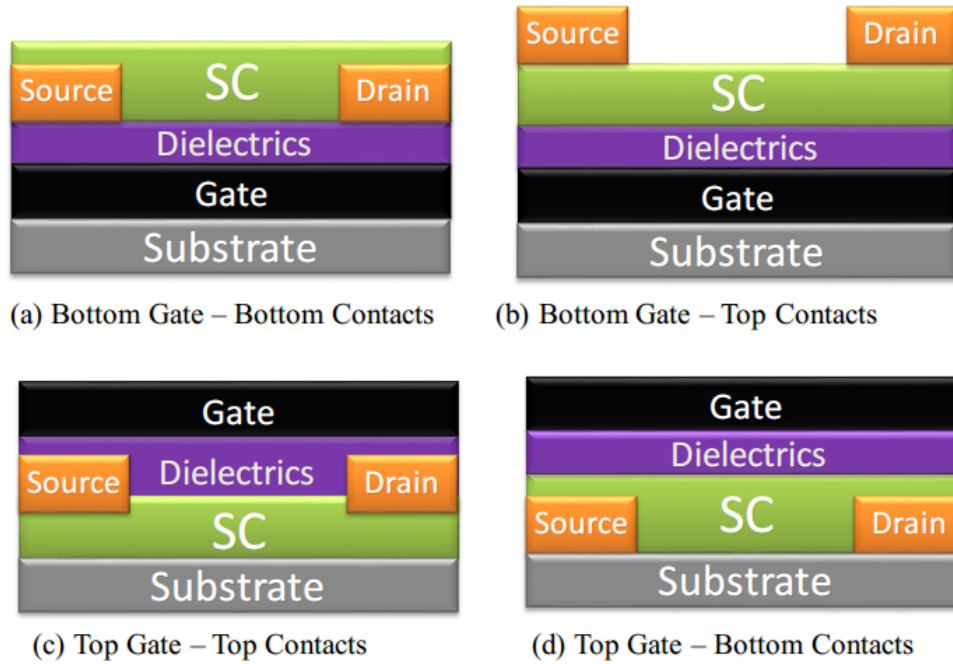


**Figure 1.1. Four geometrical structures of thin-film transistors: (a) bottom-gate bottom-contact (BGBC); (b) bottom-gate top-contact (BGTC); (c) top-gate top-contact (TGTC) and (d) top-gate bottom-contact (TGBC).**

Similar to TFTs, OFETs can be fabricated in four configurations shown in **Figure 1.1**: bottom gate – bottom contact (BGBC), bottom gate – top contact (BGTC), top gate – top contact (TGTC) and top gate – bottom contact (TCBC). The distance between the source and the drain is called the channel length ( $L$ ). This is the direction of the current flow. The larger the length is, the lower the current. The full extent of source and drain is called the channel width ( $W$ ). The longer the width is, the higher current flowing from source to drain. The BGBC is most industrially viable because the whole substrate with gate, dielectrics and contacts can be mass-produced in one company before sending to another company for

processing the active layer. In academic research, BGBC is also preferred, using the commercially well-developed Si wafer as the substrate, in which the heavily doped Si functions as the gate and the thermally grown SiO<sub>2</sub> on top of Si functions as the dielectrics (Figure 2.3).<sup>29,30</sup> Solution-processable materials for gate dielectrics are attractive for making OFETs on flexible substrates. Polymers with different chemical and physical properties have been utilized as dielectric materials in OFETs.<sup>29,31–33</sup>

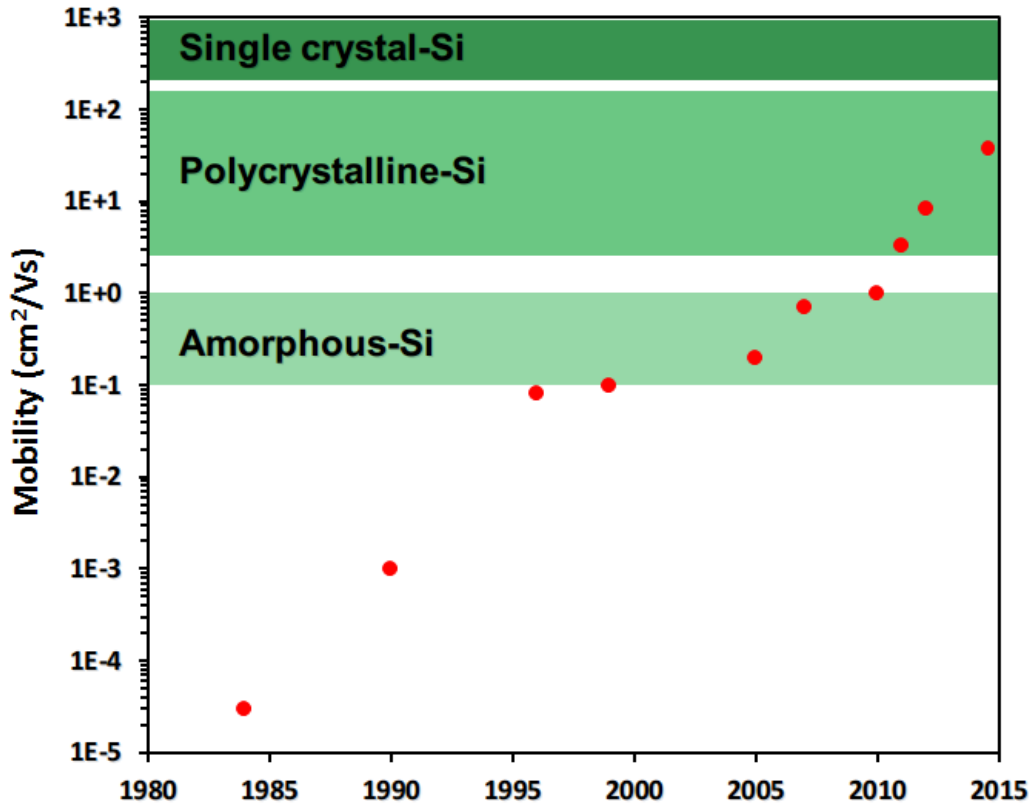


**Figure 1.2. The evolution of charge carrier mobility of OFETs, in comparison to three most used materials in FETs: single crystal silicon, polycrystalline silicon and amorphous silicon**

Significant progress has been made in solution-processed OFETs based on the use of conjugated small molecules and polymers as the semiconducting material in the FET

channel (**Figure 1.2**). Charge carrier mobilities ( $\mu$ ) more than  $10 \text{ cm}^2/\text{Vs}$  frequently achieved make such devices practical for commercialization.<sup>34–36</sup>

### ***1.2. Working Principles and Figures of Merits of OFETs***

The working mechanism of OFETs is similar to that of TFTs. The channel conductance is controlled by gate voltages while drain voltages are used to drive current in the lateral direction from the source to the drain. **Figure 1.3** describes the charge accumulation along the channel at different ranges of drain and gate voltages for an undoped organic semiconductors. In linear regime, drain voltage  $V_d$  is small and normally much smaller than gate voltage  $V_g$  ( $|V_d| \ll |V_g|$ ), charge carrier density gradually decreases from source to drain contacts. For a certain  $V_g$ , the point at which charge carrier become depleted at the drain is called the pin-off voltage  $V_{\text{pin-off}}$ . At  $|V_d| > |V_{\text{pin-off}}|$  the transistor is in saturation regime where drain current  $I_d$  no longer increases with increasing  $V_d$ .<sup>2,37–40</sup>

The current–voltage characteristics in the linear and saturation regime can be analytically derived assuming the gradual channel approximation. It requires that the electric field perpendicular to the current flow generated by  $V_g$  is much larger than the electric field parallel to the current flow generated by  $V_d$ . In order to fulfill this approximation, OFETs are normally made with channel length  $L > 10t$  where  $t$  is the thickness of the dielectrics.<sup>2,37–40</sup>



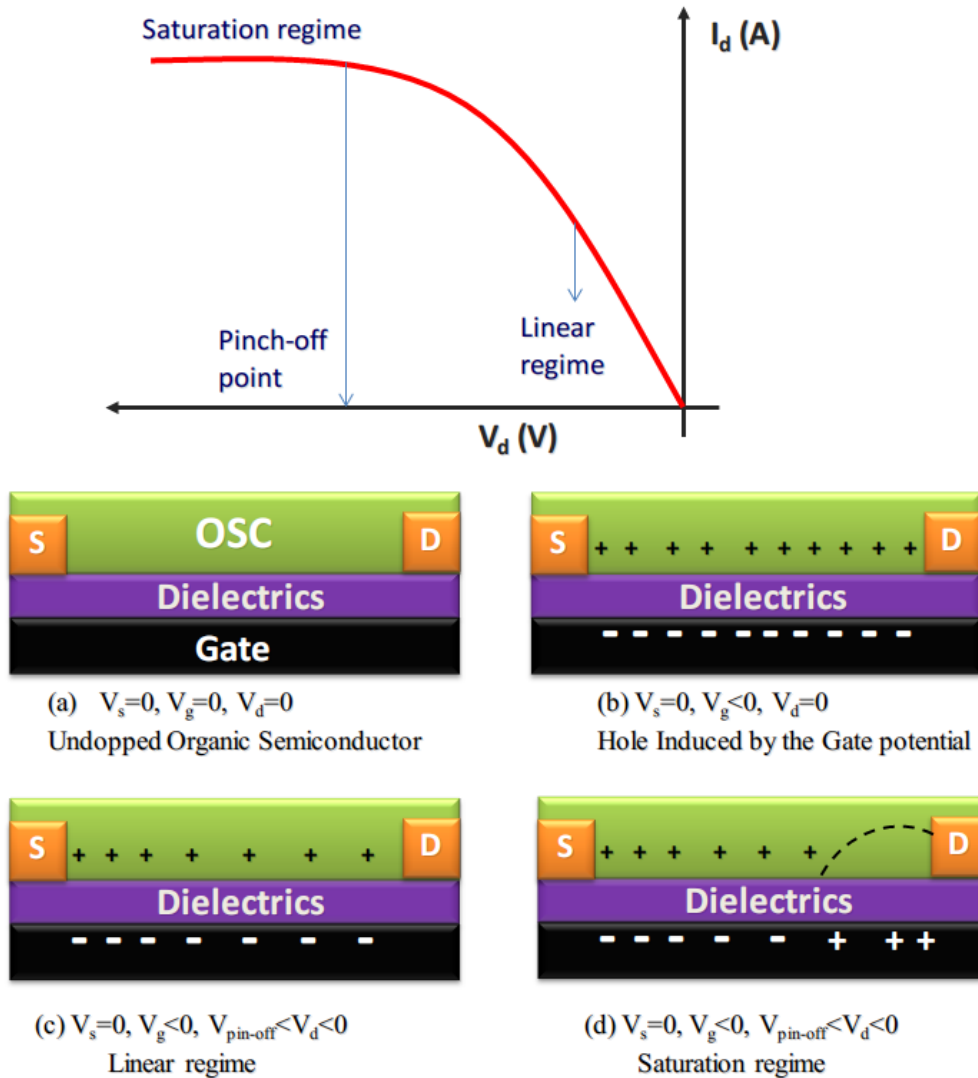


**Figure 1.3. Charge accumulation in linear regime and accumulation regime of an OFET with an undoped organic semiconductor**

In principal, charges start to accumulate in the channel when  $V_g$  is turned on. However, in OFETs, there are usually charge traps at the interface of the dielectric and the organic semiconductor. Therefore, charges induced from a certain  $V_g$  only fill the traps. This voltage is called threshold voltage  $V_{th}$ .<sup>41-44</sup> At  $V_g > V_{th}$ , excess gate voltages,  $V_g - V_{th}$ , induce mobile charges in the channel. At point  $x$  in the channel, the induced charge is proportional to the

excess gate potential and the channel potential  $V_{ch}(x)$  at point  $x$ . The source is always grounded in OFET operation. Therefore, the channel potential right at the source is presumably to be zero. Hence, the induced mobile charges  $Q_m$  per unit area at the source are related to  $V_g$  and  $V_{th}$  via the parallel capacitor charge accumulation equation<sup>40</sup>

$$Q_m = C_i(V_g - V_{th}) \quad (1)$$

where  $C_i$  is the capacitance per unit area of the gate dielectric. From the source to the drain, the channel potential  $V_{ch}(x)$  changes from zero to  $V_d$ , hence the induced charge at point  $x$  is:

$$Q_m = C_i(V_g - V_{th} - V_{ch}(x)) \quad (2)$$

Neglecting diffusion current, the source–drain current  $I_d$  is proportional to the mobile charge density and the electric field via:

$$I_d = W\mu Q_m E_x = W\mu Q_m \frac{dV_{ch}}{dx} \quad (3)$$

$$\text{then } I_d dx = W\mu C_i (V_g - V_{th} - V_{ch}(x)) dV_{ch} \quad (4)$$

where  $W$  is the channel width,  $\mu$  is the charge mobility, and  $E_x$  is the electric field at  $x$ . By integrating both sides of equation (4) with these boundary conditions:  $x = 0$  to  $L$ ,  $V(x=0) = 0$  and  $V(x=L) = V_d$ , assuming that the mobility is independent of  $V_{ch}(x)$  (i.e. independent of carrier density and hence the gate voltage), drain-source current  $I_d$  can be obtained:

$$I_d = \frac{W}{L} \mu C_i \left[ (V_g - V_{th}) V_d - \frac{1}{2} V_d^2 \right] \quad (5)$$

In the linear regime with  $|V_d| \ll |V_g - V_{th}|$ , equation (5) can be simplified to

$$I_{d,lin} = \frac{W}{L} \mu_{lin} C_i (V_g - V_{th}) V_d \quad (6)$$

From equation (6), the linear mobility (i.e. mobility in the linear regime,  $\mu_{lin}$ ) can thus be calculated via:

$$\mu_{lin} = \frac{\partial I_{d,lin}}{\partial V_g} \frac{L}{WC_i V_d} \quad (7)$$

In principal, the channel is pinched off when  $|V_d| = |V_g - V_{th}| = V_{pin-off}$ . As mentioned above, At  $|V_d| > |V_{pin-off}|$  the transistor is in saturation regime where drain current  $I_d$  no longer increases with increasing  $V_d$ . In order to describe saturation current  $I_{d,sat}$ ,  $V_d$  in equation (5) can be replaced by  $V_{pin-off}$ , yielding:

$$I_{d,sat} = \frac{W}{2L} \mu_{sat} C_i (V_g - V_{th})^2 \quad (8)$$

In this case, the square root of the drain current is proportional to  $V_g$ . From equation (8), the saturation mobility (i.e. mobility in the linear regime,  $\mu_{sat}$ ) can be calculated via:

$$\mu_{sat} = \left( \frac{\partial \sqrt{I_{d,sat}}}{\partial V_g} \right)^2 \frac{2L}{WC_i} \quad (9)$$

It should be noted that the linear and saturation mobility calculated in equation (7) and (9) are assumed to be independent of gate voltage. In the case of gate-dependent mobility, the derivative in the two equations should be calculated at a narrow range of  $V_g$  at each  $V_g$  (local derivative).

In general, an OFET is evaluated by measuring its current-voltage characteristics in two types of curves: transfer curves and output curves (**Figure 1.4**). In transfer curves, drain voltages ( $V_d$ ) are fixed and gate voltages ( $V_g$ ) are swept while current is measured. At low  $V_d$ , the transfer curve is in the linear regime; then the linear mobility and threshold voltage can be extracted by equation (7). The mobility is calculated from the slope of  $I_d$  versus  $V_g$ ; and the threshold voltage is calculated from the intercept of  $I_d$  versus  $V_g$ . At high  $V_d$ , the transfer curve is in the saturation regime; then the saturation mobility and threshold voltage can be extracted by equation (9). The mobility is calculated from the slope of the square root

of  $I_d$  versus  $V_g$ ; and the threshold voltage is calculated from the intercept of the square root of  $I_d$  versus  $V_g$ . Another figure of merit is ON/OFF ratio, which is the ratio of OFF current (flat  $I_d$  at  $V_g$  in the far positive for p-type OFETs) and ON current at certain  $V_g$  and  $V_d$ . The output curves are evaluated in two aspects. Firstly, the range of  $V_d$  and  $V_g$  at linear and saturation regime are determined. Secondly, the shape of output curves at  $V_d \sim 0$  V can reflect the effect of contact resistance of the device. If the effect of the contact resistance is high, output curves exhibit the S-shape instead of being linear at  $V_d \sim 0$  V.

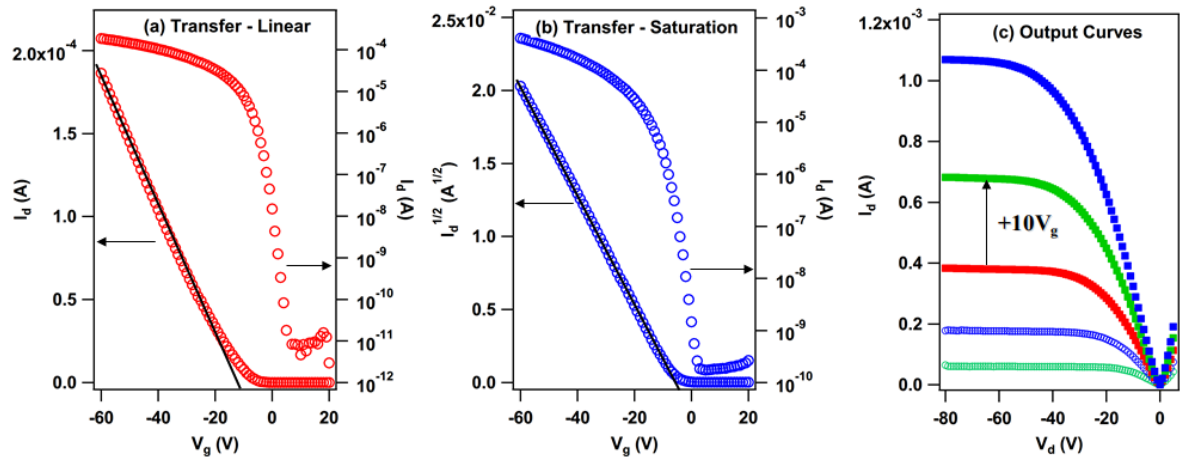


**Figure 1.4. Typical transfer curves in (a) linear regime and (b) saturation regime (b); and (c) output curves of a p-type OFET.**

In the linear regime of the output curves, linear mobility can also be calculated. From equation (6), channel conductance  $\partial I_d / \partial V_d$  is calculated, then the linear mobility is calculated at given  $V_g$  and  $V_{th}$ :

$$\mu_{lin} = \frac{\partial I_{d,lin}}{\partial V_d} \frac{L}{WC_i (V_g - V_{th})} \quad (10)$$

All the figures of merit of OFETs are summarized in Table 1.1.

**Table 1.1. OFET basic figures of merit and calculated methods**

	Linear mobility	Saturation mobility	Threshold voltage	ON/OFF ratio
Calculation Method	Slope of $I_d$ vs. $V_g$ Slope of $I_d$ vs. $V_d$	Slope of $\sqrt{I_d}$ vs. $V_g$	Intercept of $I_d$ vs. $V_g$ or $\sqrt{I_d}$ vs. $V_g$	Ratio OFF $I_d$ and ON $I_d$

### 1.3. Organic Semiconductors for OFETs

#### 1.3.1. Semiconducting Conjugated Organic Materials

The discovery of semiconducting organic materials was reported by researchers in 1950s and 1960s, mostly based on the study of charge injection, transport and recombination in single crystal anthracene.<sup>45–50</sup> A breakthrough happened in 1970s when Heeger, MacDiarmid and Shirakawa demonstrated that the conductivity of polyacetylene can be controlled over a range of more than seven orders of magnitude by chemical doping.<sup>51,52</sup> Tang and Van Slyke made another major contribution when discovering electron and hole injection into a non-crystalline organic semiconductor.<sup>53–55</sup> These discoveries open up a completely new class of conducting and semiconducting materials which are based on alternating single and double bonds organic molecules, i.e.  $\pi$ -conjugated materials.

The conducting and semiconducting properties of  $\pi$ -conjugated materials originate from the bonding and delocalization of the p-orbitals. In conjugated molecules, three out of four electrons in the outer shell of each carbon atom form three  $\sigma$ -bonds; in which the carbon-carbon  $\sigma$ -bonds form the skeleton of the molecule. The fourth valence electron of each carbon, the 2p electron, contributes to the molecular delocalized  $\pi$ -orbitals perpendicular to the  $\sigma$ -skeleton (**Figure 1.5**).<sup>56</sup> The nature of the electrical conductivity of  $\pi$ -conjugated

organic molecules stems from the orbital overlap of the  $\pi$ -orbitals along the conjugated backbone of the molecules (Figure 1.5b). The orbital overlap allows prompt reorganizations of the electron clouds in the molecule to accommodate the introduction of an external charge (hole/electron) (Figure 1.5c). This continuous electron cloud shifting is the foundation of the electrical conduction in one  $\pi$ -conjugated molecule.<sup>52,57</sup>

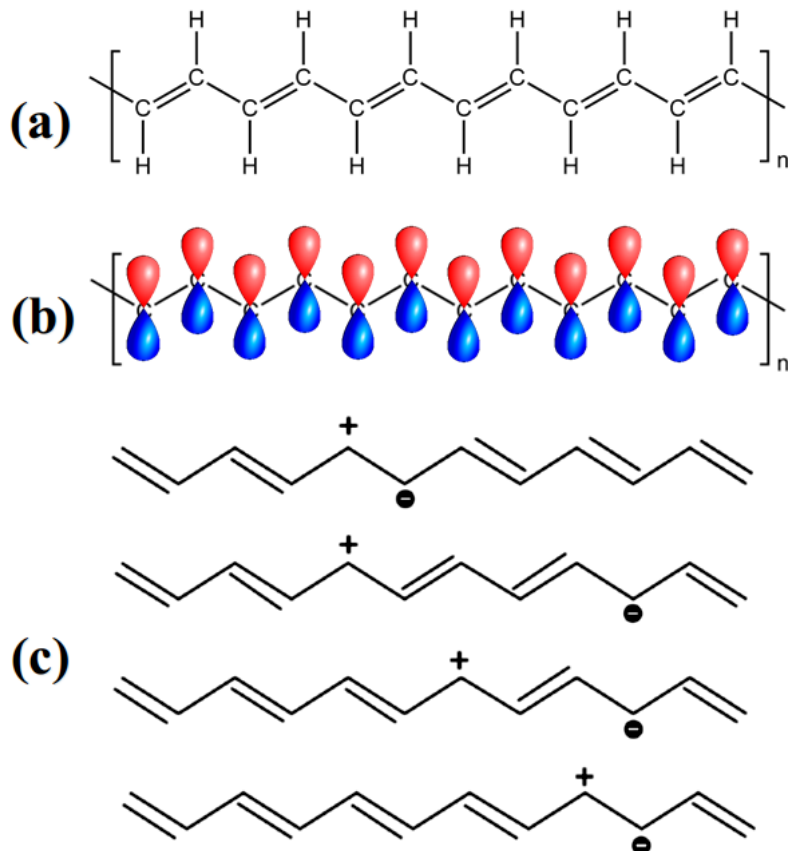


**Figure 1.5.** (a) Chemical structure of trans-polyacetylene; (b) the orientation and delocalization of 2p orbitals in the normal plane to the  $\sigma$ -skeleton of polyacetylene; and (c) schematic diagram of hole transport in an oligo-acetylene: hole is introduced to the molecule by removing an electron from the fifth carbon (via doping for example), then migrated along the backbone through the reorganization of 2p orbitals.

As  $\pi$ -conjugated materials assemble in solid state films, their electrical conduction mechanism can be explained by the band theory of conduction.<sup>57</sup> In molecular orbital theory, a material with  $N$  interacting atomic orbitals will have  $N$  molecular orbitals. In a continuous solid-state material with perfect crystalline structure,  $N$  will be a very large number (typically  $10^{22}/\text{cm}^3$ ). With so many molecular orbitals spaced together in a given range of energies, they form an apparently continuous band of energies (**Figure 1.6**).  $N$  electrons fill from low energy bands to high energy bands. The energy spacing between the highest occupied band (valence band) and the lowest unoccupied band (conduction band) is called the *band gap*. The bonding of p orbitals in conjugated materials contribute to the conduction of charges. When the number of p orbitals increases, the band gap becomes smaller and approaches the band gap of traditional semiconducting materials like silicon.<sup>57,58</sup>

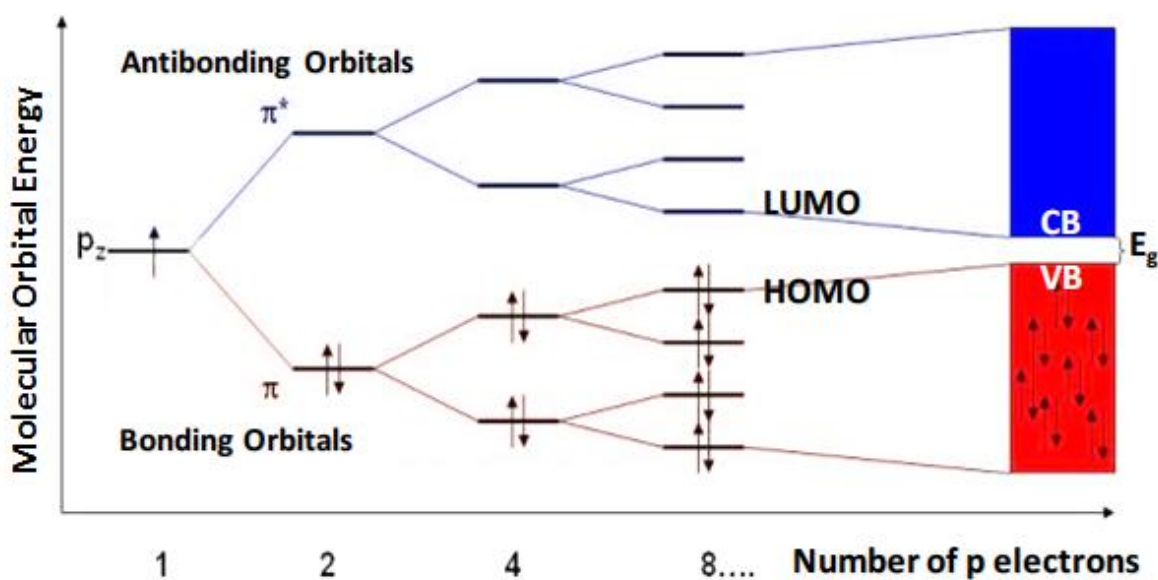


**Figure 1.6. The use of molecular orbital theory in  $\pi$ -conjugated materials to explain the formation of HOMO, LUMO and reduced band gap compared to insulating materials**

In crystalline silicon with all the atoms covalently bond to each other, N is a very large number therefore conduction band and valence band are formed. On the other hand, conjugated organic molecules hold together in solid state primarily by weak Van der Waals force. Different molecules can have different orientation and backbone geometry. These disorders make the number of p orbitals contributing in MO  $\pi$ -orbitals in a conjugated segment finite. As a result, instead of forming the energy bands and corresponding conduction and valence bands, organic semiconductors in solid state rather form discrete molecular orbitals. The band gap is formed between the highest occupied molecular orbital (HOMO) and the lowest unoccupied molecular orbital (LUMO) (**Figure 1.6**).

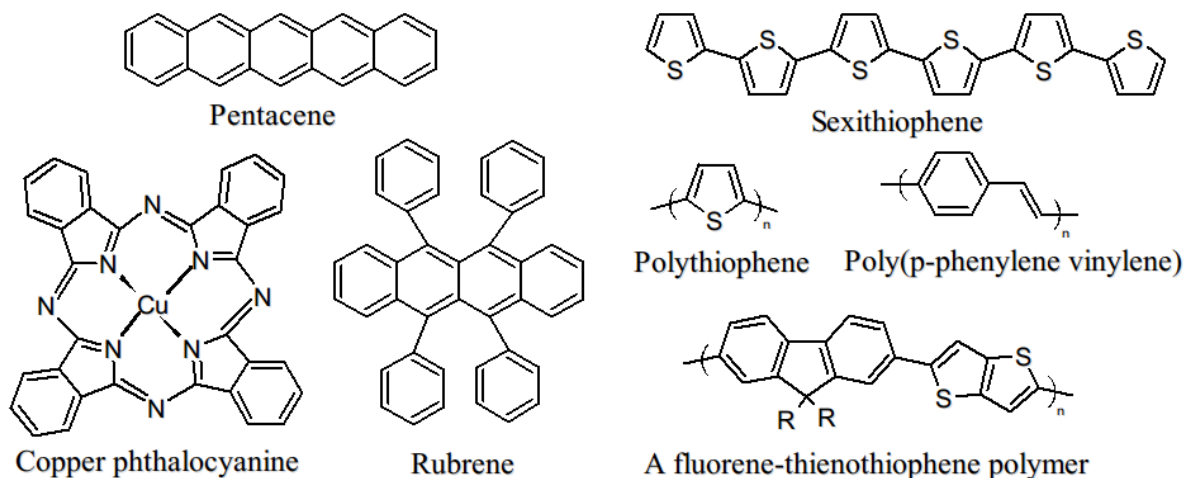


**Figure 1.7. Chemical structures of some organic semiconductors used in p-type OFETs. Adapted from Ref.<sup>56,59</sup>**

In the late 1980s, researchers at Mitsubishi Chemical Research Center used polythiophene to fabricate thin-film transistor for the first time.<sup>25,26,28</sup> Since then, many classes of  $\pi$ -conjugated small molecules and polymers have been developed to improve OFET performances. Typical examples of organic semiconductors used in OFETs, shown in



**Figure 1.7**, are metal phthalocyanine, oligocene (pentacene, rubrene), oligothiophene, and polymers based on thiophene, phenylene vinylene, fluorene, and thienothiophene units.

### 1.3.2. Donor-Acceptor (D-A) Conjugated Polymers for OFETs

Donor-acceptor (D-A) copolymers are the most recent class of materials developed for high-mobility OFETs and high performance OPV.<sup>60–65</sup> D-A copolymers are comprised of alternating electron rich (donor) and electron poor (acceptor) conjugated segments. **Figure 1.8** demonstrates one effect of D-A structure in enhancing charge transport in OFETs, via a reduced reorganization of hole propagation, in comparison to D-D polymers. The induced partial charge in the electron rich and electron poor units is beneficial to reduce the reorganization energy when charges move from one segment to another.<sup>36,66</sup> When a charge is accepted by a conjugated segment, its existing partial charge helps to accommodate the charge with less change in charge distribution hence less reorganization energy.<sup>36,66</sup>

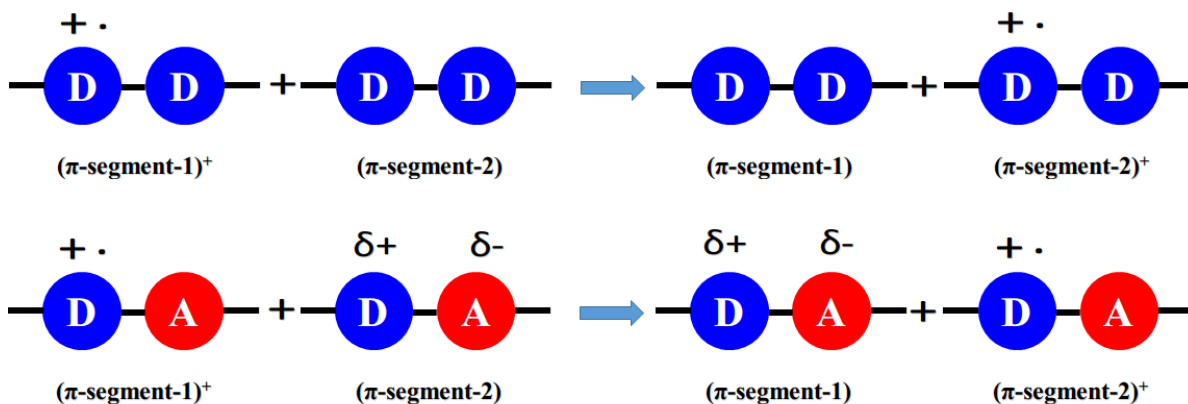


**Figure 1.8. Schematic diagram of the reduced reorganization of hole propagation in D-A copolymers, in comparison to D-D polymers. The partial charge in each conjugated segment is subjected to less change in charge distribution hence less reorganization energy when it accommodates a charge (hole in this case). Adapted from Ref.<sup>36</sup>**

In addition, Yuning Li and coworkers hypothesized that the dipole-dipole interaction between donor and acceptor moieties of two polymer chain enhances the  $\pi$ - $\pi$  interaction hence improve the mobility.<sup>36,66</sup> Mullen and coworkers, on the contrary, used solid-state 2D NMR to show that the donor units pack in a closer proximity to the donor units of the adjacent polymer chain, and vice versa.<sup>67</sup> They suggested that the rigid backbone of the D-A polymer mainly contributes to the tight packing of the polymer in solid state. D-A materials (small molecules and polymers) have also been used in organic solar cells due to their reduced bandgap and improved charge carrier mobility. Some examples of high-mobility D-A copolymers can be found in **Table 5.1**.

#### ***1.4. Charge Transport and Charge Injection in OFETs***

##### 1.4.1. Charge Transport

Charge transport in organic semiconductors has been studied intensively in the last thirty years, in various types of organic electronic devices such as hole and electron-only diodes,<sup>68,69</sup> OFETs,<sup>2,37,39</sup> OLEDs,<sup>70-73</sup> and organic solar cells (OSCs).<sup>74,75</sup> In solution-processed thin films of organic semiconductors, the morphological disorder greatly dictates the charge transport. The disorder results in the localized state with different energy level.<sup>76-79</sup> The density of states (DOS) as a function of energy can be described by either Gaussian or exponential distribution.<sup>78,80-82</sup> Regardless of the shape of the DOS, the energetic disorder results in the hopping of charges between localized states (**Figure 1.9**). The hopping mechanism becomes the widely accepted charge transport mechanism in solution-processed organic electronic devices with a certain degree of energetic disorder. Different theoretical and experimental approaches have been investigated to characterize the DOS.<sup>77,78,81,83-85</sup>

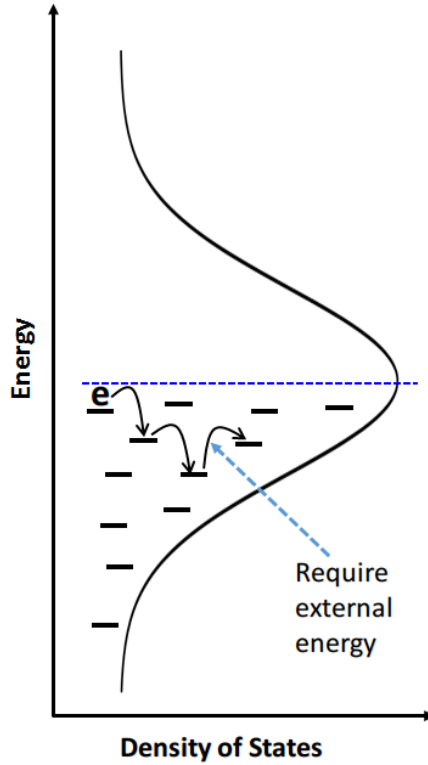


**Figure 1.9. Gaussian density of states comprising of localized states with different energy level. Electrons spontaneously hop (or relax) from higher energy levels to lower energy levels. In order to hop to the higher energy level, external energy (thermal energy, electrical energy) is needed.**

In the context of this thesis, the charge carrier hopping is considered as a basic thermally activated process, which is described by the Arrhenius equation:<sup>2,68,86-88</sup>

$$\mu = \mu_0 e^{-\frac{E_a}{kT}} \quad (11)$$

in which  $\mu$  is the charge carrier mobility,  $\mu_0$  is the mobility prefactor,  $E_a$  is the activation energy and  $k$  is the Boltzmann constant. One can measure the mobility of OFETs at different temperatures and fit the data to equation (11) to extract the activation energy  $E_a$ , which reflects the average energetic barrier for charge carrier hopping. The lower the  $E_a$ , the higher

the mobility at a certain temperature. This analysis is used in chapter 4 to characterize the charge transport mechanism in high-mobility PFETs fabricated from D-A copolymers.

Numerous fundamental scientific questions regarding the charge-transport physics and structure–property relationships of organic semiconductors can be studied in FET devices thank to their ability to control the charge-carrier concentration by gate potentials.<sup>39</sup> Significant efforts have been put to understand the fundamental electronic structure of the organic semiconductor, and how transport processes in molecular level determine the electrical characteristics of macroscopic devices.<sup>89–91</sup> An important aspect of charge transport in OFETs, which differs from charge transport in vertical devices like organic diodes, is the crucial effect of the dielectric interface. As mentioned above, charge transport in TFT happens at a few nanometers above the dielectrics.<sup>1,42</sup> Therefore, the quality of the dielectric interface and the molecular packing right at the interface greatly influence the device physics of OFETs. In chapter 3, it is shown that the polymer chain alignment in only a few nanometer polymer layer right at the dielectrics results in the improvement of the mobility. In chapter 5, it is shown that two different dielectric surfaces have dramatically different impact on the charge trapping and device stability of high-mobility PFETs fabricated from D-A copolymers.

#### 1.4.2. Charge Trapping and Device Instability

Another important topic is the understanding of the electrical instability mechanisms, which are becoming an increasingly important topic as OFETs are approaching large-scale production with strict reliability and lifetime requirements.<sup>30,91,92</sup> The OFET figure of merits (FOMs) (most importantly mobility, threshold voltage and ON/OFF ratio) are desirable to be constant upon prolonged operation (ON state). However, it is well established that those

FOMs change under bias-stress, caused by the gate and drain bias applied to OFETs for several hours to several days.<sup>30,92</sup> For p-type OFETs, it has been reported by several groups that the threshold voltages negatively shift up to the gate bias.<sup>30,43,92–95</sup> There are several hypotheses that explain the bias-stress effect in p-type OFETs including interfacial charge trapping, bipolaron trapping<sup>95</sup>, water effect.<sup>93,96,97</sup> Among them, the effect of electrochemical reactions of a trace amount of water trapped at the interface of SiO<sub>2</sub> dielectric and organic semiconductors is most plausible to explain the current-voltage changes upon bias-stress.<sup>97</sup> In n-type OFET study, it was found that silanol groups (–SiOH) on SiO<sub>2</sub> surface can trap electron and turn to –SiO<sup>•-</sup>.<sup>30,98,99</sup> The bias-stress of ambipolar OFETs has been reported;<sup>94,100,101</sup> but the main cause is not well-understood.<sup>30</sup> In chapter 5, a special case of OFET electrical instability is investigated where electron trapping causes the instability of the device performance of a p-type OFET.

#### 1.4.3. Charge Injection

Another important aspect of the device physics is the injection of charges from the source contact into the organic semiconductor. The parameter that describes the energetic injection barrier and other effects that preventing charge injection is called contact resistance.<sup>92,102–105</sup> In inorganic semiconductors, contact resistance can be minimized by controlling doping concentrations of the semiconductors at the contact.<sup>1</sup> However, controlled doping of organic semiconductors is still difficult, since dopants incorporated in the form of small-molecule counterions can migrate and cause device instabilities.<sup>39,92</sup> In addition, doping in solution-processed organic semiconductors is often accompanied with changes in morphology, hence complicates the device analysis.<sup>106–108</sup> For the devices with short channel

length ( $L < 5\mu\text{m}$ ), the channel resistance becomes smaller and comparable to the contact resistance. Therefore, reducing contact resistance is crucial in short channel length OFETs.

Most of OFETs are made with undoped organic semiconductors. In this case, metals with work-function closest to corresponding HOMO for p-type and LUMO for n-type OFETs are chosen to minimize contact resistance. In p-type OFETs, Au is the most common contact because it has the work-function of around 5.0 eV that is very close to the HOMO of most organic semiconductors. In addition, Au is a stable metal. For organic semiconductors with very low-lying HOMO ( $>5.5$  eV), modification of contacts with high work-function metal oxides, most commonly  $\text{MoO}_x$  have been applied.<sup>109–113</sup> For n-type OFETs, finding a stable metal with work-function close to LUMO of most organic semiconductors (3.0 – 4.0 eV) is more challenging.<sup>66,114,115</sup> Recent high-mobility n-type OFETs have been made with low-lying LUMO ( $>4.0$  eV) and therefore Au or Ag are sufficient to make good contacts.

Recently, high-mobility p-type PFETs have been achieved with narrow band-gap polymers, with LUMO approaching 4.0 eV and HOMO around 5.2 eV. When Au is used for contacts in these devices, electron injection and transport can be enable. In chapter 5, a full analysis of how this electron injection and transport affect hole conduction.

### ***1.5. Motivation and Structure of the Thesis***

The thesis aims to investigate in depth the three fundamental aspects that dictate the performance and practicability of high mobility PFETs including (1) polymer assembly in thin film, (2) charge transport mechanism, and (3) electrical instability. The ultimate goal is to provide guidelines for designing novel materials and engineering devices toward high-mobility and stable PFETs.

Chapter 2 describes the main experimental methods used in the thesis. In chapter 3, a study of molecular assembly a high-mobility PFET system fabricated from aligned polymer chains is presented. The effect of molecular weight is an important focus in chapter 3. In chapter 4, the charge transport aspect of the PFET in chapter 3 is clarified. In chapter 5, the electrical instability and non-ideality in high-mobility PFETs fabricated from D-A copolymers is thoroughly investigated, using the same model system as in chapter 3 and 4. The mechanistic study of chapter 5 proves different methods for suppressing the electrical instability and non-ideality by virtues of molecular design and device engineering. Chapter 6 demonstrates the successful executions of three methods suggested in chapter 5 to improve device stability and ideality. Finally, conclusion and outlook is presented in chapter 7.

### ***1.6. Characterizations of Organic and Hybrid Materials***

In the course of PhD, the thesis author has done researches in characterizing different organic and hybrid organic-inorganic electronic materials. In order to keep the coherent story of PFET in-depth study in the thesis, these works are either briefly mentioned here or presented in the Appendix.

One important work is designing and characterizing an improved hybrid bulk-heterojunction materials based on nanostructured TiO<sub>2</sub> and conjugated small molecules for solar cells and photodetectors. This achievement, which was published in Applied Physics Letters (volume 104, page 233305), is reorganized and presented in **Appendix 9.2**. The work was in a collaboration with Dr. Justin Jahnke and Professor Bradley Chmelka. The nanostructured TiO<sub>2</sub> was synthesized by Dr. Justin Jahnke.

Another significant accomplishment of my PhD research is the comprehending and applying conducting and photo-conducting AFM (c-AFM and pc-AFM) to material and

device characterization. In one project, I utilized c-AFM to reveal that the more continuous conduction network of hybrid TiO<sub>2</sub>-graphene anodes that employ smaller TiO<sub>2</sub> nanoparticles is responsible for the higher power conversion efficiency of dye-sensitized solar cells (DSSCs). The study reveals a size-dependent electron transport property of the TiO<sub>2</sub>-graphene composite photoanodes. As the TiO<sub>2</sub> particle size decreases, a more continuous electron transport network is formed and results in a higher electron mobility in the smaller-sized TiO<sub>2</sub> based composite electrode, indicated by c-AFM dark current images and nano I-V curves. The continuous conduction network reduces the internal resistance at TiO<sub>2</sub>/TiO<sub>2</sub> and TiO<sub>2</sub>/FTO interfaces, ultimately resulting in a faster and more efficient electron transfer of the device using the smaller size of TiO<sub>2</sub> particles. This is the first study that successfully applies c-AFM to characterize DSSC photoanodes and correlates DSSC nanoscale properties to bulk device performance. The results help our collaborators from Nanyang Technological University (Singapore) rationalize the effect of TiO<sub>2</sub> particle size on the current collection efficiency of hybrid TiO<sub>2</sub>-graphene anodes (see Ref. 120 for more information).

Another appealing application of c-AFM and pc-AFM that we have discovered is to directly observe the dopant distribution in molecular-doped organic semiconductor films. Molecular doping in organic electronics has been demonstrated to boost the performance of wide range of devices, for instance the enhanced mobility in FETs, or improved charge injection in light-emitting diodes (LEDs). Developing a tool to directly visualize doping sites is crucial for researchers to control the doping efficiency and design better dopants. We have managed to employ c-AFM for direct visualization of doping sites in p-type doping of semiconducting polymer poly(3-hexylthiophene) (P3HT) with a molecular acceptor (hereinafter called F4TCNQ). Our collaborators in Stanford University hypothesize that in the “weak doping” regime (low concentration of dopants), F4TCNQ dispersed among



amorphous domains of P3HT in thin films. On the other hand, in the “strong doping” regime, F4TCNQ molecules bind to the polymer backbone to form a new crystalline domain in the solid state. However, those microstructures had been only proved indirectly by optical absorption and x-ray diffraction. I optimized c-AFM scanning at high resolution (scan size  $500\text{ nm} \times 500\text{ nm}$ ) and directly observed the high current spots in the order of  $15 - 30\text{ nm}$  on the background of low current in the “weak doping” films. It means that F4TCNQ locally disperses in the film and dopes P3HT at those high current spots. On the other hand, in the “strong doping” films, we observed fairly uniform current distribution. This suggests that dopant molecules are not dispersed across amorphous regions but are instead incorporated into P3HT crystallites and improve the conductivity of the whole films. The results not only help to control dopant distribution, but also open up the opportunity to apply c-AFM and pc-AFM to study other effects of dopants in organic electronics, such as charge injection and photo-current generation (see Ref. 107 for more information).

## 2. Materials and Experimental Methods

### 2.1. Semiconducting Polymers

The model polymer that is mainly used in this thesis is the regioregular poly[4-(4,4-dihexadecyl-4H-cyclopenta[1,2-b:5,4-b']dithiophen-2-yl)-*alt*-[1,2,5]thiadiazolo[3,4-c]pyridine] (PCDTPT, Figure 2.1).<sup>65,116,117</sup> The copolymer comprises of the CDT donor unit and PT acceptor unit, as shown in **Figure 2.1**. The polymer has an energy gap of 1.2 eV, HOMO of  $\sim 5.2$  eV and LUMO of  $\sim 4.0$  eV, characterized by cyclic voltammetry and optical absorption.<sup>65</sup> In chapter 5 and 6 a few other polymers are introduced to generalize the findings of the thesis. The copolymer in this thesis is firstly developed and synthesized by Dr. Lei Ying; then by Dr. Ming Wang at Professor Guillermo Bazan's group.

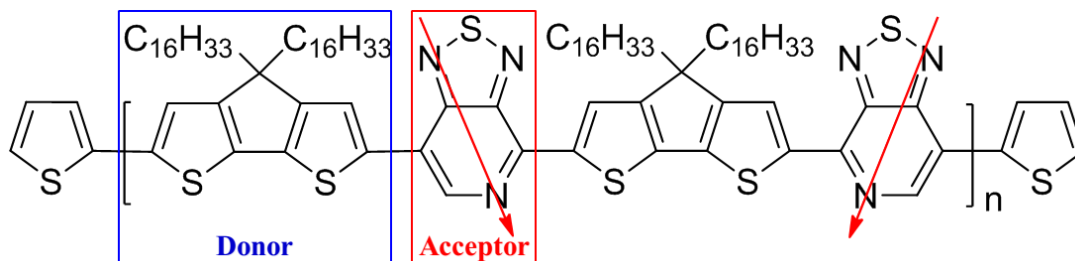


**Figure 2.1. Molecular structure and regioregularity pattern of PCDTPT. The arrows are guides to the eye to highlight stereoregularity.**

In previous works of PCDTPT, high molecular weight (MW) (up to 300 kDa) and region-regularity were shown to be important to obtain higher carrier mobility in OFETs fabricated by either spin-coating or drop-casting the polymer.<sup>116</sup> A method of combining nano-grooved substrates and slow drying in a tunnel-like configuration was demonstrated by Dr. Hsin-Rong Tseng to align the polymer into highly oriented fibers. The fiber was around 50 nm wide and aligned in parallel with the charge flow direction from the source to the

drain. This alignment helped to achieve a hole mobility of  $6.7 \text{ cm}^2/\text{Vs}$  for 300 kDa PCDTPT.<sup>116</sup> In the subsequent chapter 3 and 4, a collaboration work with Dr. Hsin-Rong Tseng aims to 1) understand how molecular weight affect charge carrier mobility in PFETs fabricated with aligned polymer fibers; 2) reveal polymer chain assembly in the 50-nm-wide fibers and 3) elucidate the charge transport mechanism of PFETs fabricated with aligned polymer fibers.

## 2.2. OFET Fabrication

*Nano-grooved substrates:* Nano-grooved substrates were introduced on the surface of  $\text{SiO}_2$  gate dielectric layer by scratching the surface with diamond lapping films (from Allied High Tech Products Inc.) with nanoparticle sizes of 100 nm.

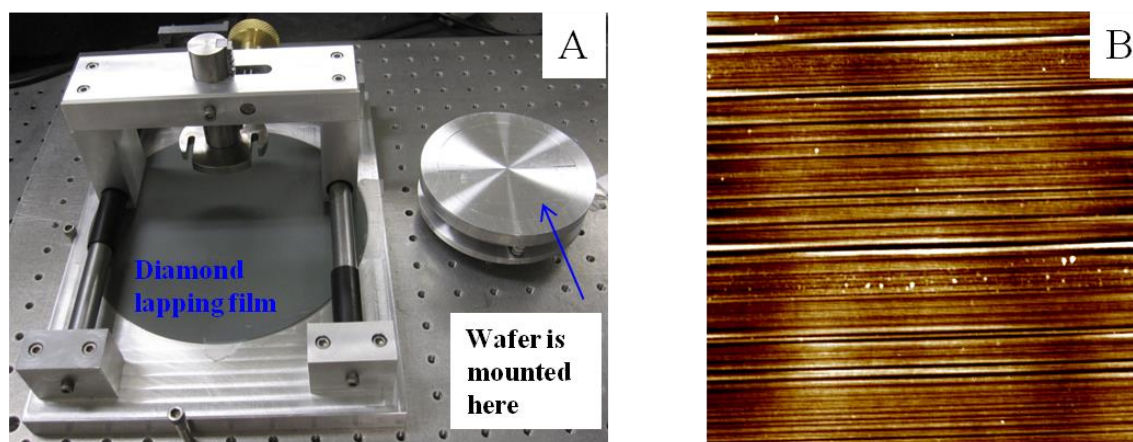


**Figure 2.2.** The home-made scratching machine (A) and the resulting surface of  $\text{SiO}_2$  after scratching (B) at scan size  $2\mu\text{m} \times 2\mu\text{m}$ .

A home-made scratching machine is made for this purpose, shown in **Figure 2.2**. Firstly the diamond lapping film is fixed on the stage and the silicon wafer is fixed on a moving holder facing the diamond film. The moving holder then goes down for the wafer to attach the diamond film and adjust the pressure to about  $0.1 \text{ kg}/\text{cm}^2$ . The holder can move forward

and backward in one direction for total scratching distance  $\sim 1.5$  m to induce the parallel grooves on the substrate. During the scratching process deionized water is required between the wafer and diamond lapping film to achieve uniform surface grooves with high density.

*Device preparation:* Bottom gate, bottom contact FETs with the architecture “Si (500  $\mu\text{m}$ ) / SiO<sub>2</sub> (300 nm) / Au (50 nm) / decyltricholasilane / PCDTPT” were fabricated by either spin-coating or sandwiched-casting the polymer on nano-grooved substrates.<sup>117</sup> The pre-patterned substrates (Si/SiO<sub>2</sub>/Au, L=80  $\mu\text{m}$ , W=1000  $\mu\text{m}$ ) were first cleaned by acetone/isopropanol, then treated by UVO<sub>3</sub> for 15 minutes, right before being passivated by decyltricholasilane (DTS) from 1 vol.% toluene solution at 80 °C for 25 minutes. Passivated substrates were then transfer to nitrogen glovebox to deposit the polymer by spin-coating (8 mg/ml in chloroform) or sandwich-casting (0.25 mg/ml in chlobenzene). In sandwich-casting technique, two pre-patterned-contact substrates are held together in a tunnel-like configuration using two glass spacers (**Figure 2.3**). An amount of ca. 70  $\mu\text{l}$  of a dilute solution of polymers is added into the tunnel. The whole tunnel is placed inside a petri-dish filled with organic solvent to slow-down the evaporation. It takes around 4-6 hrs to completely dry the solution. The samples were annealed at 200 °C for 8 min before measurement. The capacitances are 10 and 11.5 nF/cm<sup>2</sup> for normal and nano-grooved substrates.

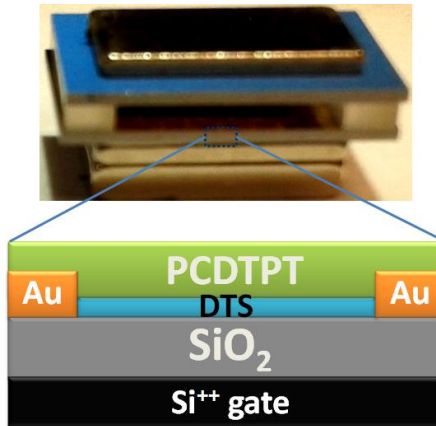


**Figure 2.3. Schematic of sandwich-casting technique to fabricate PFETs in the thesis**

In chapter 6, bottom gate, top contact FETs with the architecture “Si (500  $\mu\text{m}$ ) / SiO<sub>2</sub> (300 nm) / BCB (170 nm) / PCDTPT/ Au” were fabricated by spin-coating the polymer on SiO<sub>2</sub>/BCB substrates prior to thermal evaporating Au source and drain contacts. BCB was prepared by spin-coating the customized dilution of the commercialized Cycotene 3022-46 (Dow Chemicals) on cleaned SiO<sub>2</sub> substrates, followed by thermal cure at 300 °C in 1 minutes.

### ***2.3. Electrical measurements of OFET***

All the electrical measurements are conducted by a Keithley semiconductor parametric analyzer (model 4200-SCS). The analyzer has ultra-low current noise level below 10 pA. Built-in programs are allowed to characterize basic transfer curves, output curves and current vs. time at fixed V<sub>g</sub> and V<sub>d</sub>. New programs are coded to perform more sophisticated measurement. At all temperatures (80K to 300K), the electrical measurements is performed inside a Lakeshore vacuum probe-station under a vacuum of <math>10^{-6}</math> mbar. The devices were heated at 400 K in vacuum for 7 hours prior to the temperature-dependent measurements.

#### ***2.4. Programming for current transient measurements***

In the Model 4200-SCS, external equipment is controlled via the User Test Modules (UTMs), which are essentially C functions created and maintained with the Keithley User Library Tool (KULT). Using KULT interface, new program can be coded to perform transient current measurements where gate voltages and drain voltages can be changed at any specific time during the course of a measurement without stopping it. In addition, the time interval between recorded current can be altered with either linear or exponential functions with measuring time. One new program is developed and coded to measure the hole current dynamic under different bias stresses at different time intervals, which is used in section 5.5 to probe the mechanism of the double-slope.

#### ***2.5. Atomic Force Microscopy***

Atomic force microscopy (AFM) is technique in the family of scanning probe microscopes (SPM).<sup>118,119</sup> AFM operates by measuring and monitoring the local force between a probe and sample surface. Normally, the probe is a sharp tip, which is a 3-6  $\mu\text{m}$  tall pyramid with 15-40 nm end radius.<sup>107,120,121</sup> To acquire an image, AFMs can generally measure the vertical and lateral deflections of the cantilever by using a system of laser beam and photodiode. The laser beam shines to the upper part of the cantilever. Atomic forces induced by the surface to the tip deflect the cantilever and therefore change the deflection of the laser beam. The reflected laser beam strikes a position-sensitive photo-detector consisting of four-segment photo-detector. The differences between the segments of photo-detector of signals indicate the position of the laser spot on the detector and thus the angular deflections of the cantilever. All AFM measurements are performed with a Bruker Multimode AFM system under nitrogen atmosphere. In the glovebox, the Multimode is

placed on a hanging stage to reduce vibration from the building. Budget Sensor AFM tips with force constant of 2.0 nN/nm and resonance frequency of c.a. 300 kHz.

### **3. Device Performance and Polymer Alignment of PCDTPT at Different Molecular Weights**

#### ***3.1. Introduction***

That charge carrier mobilities ( $\mu$ ) of  $10 \text{ cm}^2/\text{Vs}$  have been frequently achieved make OFETs approach closer to industrial applications.<sup>34–36</sup> In term of organic semiconductors used in OFET, conjugated polymers have better film forming and mechanical properties, compared with their small molecule counterparts.<sup>122–124</sup> Several strategies including process optimization<sup>125–129</sup> and molecular design<sup>67,65,124,130</sup> have been proposed to achieve order within the polymer fibers and better polymer packing. One of the most important variables in using polymers for OFETs is controlling molecular weight (MW).<sup>67,131–133</sup> Batch-to-batch variation in MW can greatly affect device performances. It has been shown that low MW materials tend to form crystalline domains, and the “grain boundaries” significantly reduce the carrier mobility.<sup>134,135</sup> The general practice in the field is to obtain high-molecular-weight polymers to enable the formation of interconnected aggregates that is beneficial for obtaining high carrier mobility.<sup>136</sup> From the synthesis point of view, the production yield for high MW materials with low polydispersity remains a challenge. In addition, high MW materials also difficult to dissolve, and the high viscosity limits utility in high-resolution inkjet printing.

In section 1.4, it is mentioned that charge transport in organic semiconductor strongly depends on the molecular assembly in solid-state thin film. In PFETs, it has been reported that the alignment of the polymer is critical for obtaining high mobility. Tseng and coworkers showed the significant improvement of mobility in PCDTPT FETs after the polymer was aligned.<sup>116</sup> In the FET with aligned polymers, the mobility in parallel devices



(charges move along the polymer fibers) was several times higher than that in perpendicular devices (charges move along the polymer fibers). It was hypothesized that the polymer chains pack along the fiber and hence facilitate the efficient intrachain charge transport along the fiber.<sup>116</sup> A direct visualization of polymer chain packing is important to correlate the molecular assembly and charge transport.

Direct visualization of molecular packing has been always fascinated scientists. Scanning tunneling microscopy (STM) is one of the powerful tool to visualize the assembly of atoms and molecules at the resolution of a few nanometers.<sup>137</sup> The utilization of STM, however, requires high vacuum and very smooth surface to obtain high resolution image. In addition, it can only work for conducting materials. AFM, however can be used for any kind of materials and does not require vacuum to obtain high resolution image.<sup>119</sup> The resolution of AFM is generally lower than STM, yet proved to be sufficient in many applications.

In this chapter, a systematic study of OFETs fabricated with PCDTPT of several MWs (ranging from 30 to 300 kDa) is carried out to understand the relationship between MW, carrier mobility and polymer alignment. High-resolution AFM is used to visualize the polymer fiber in a few nanometers length scale, which can suggest the alignment of polymer backbone.

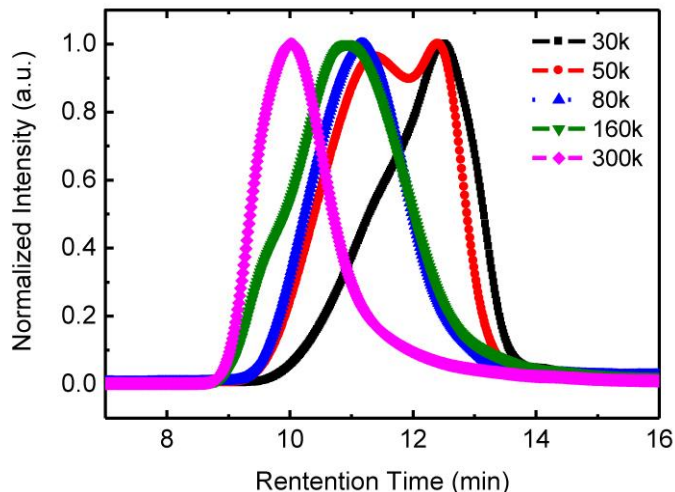


**Figure 3.1.** The GPC data of different molecular weight polymers. The data was obtained by Dr. Ming Wang.<sup>117</sup>

**Table 3.1.** Summary of average molecular weight and polydispersity of different molecular weight materials. The data was obtained by Dr. Ming Wang.<sup>117</sup>

	300k	160k	80k	50k	30k
<i>M<sub>n</sub></i> (kDa)	299	163	78	47	33
<i>M<sub>w</sub></i> (kDa)	1,203	561	131	93	56
<i>PDI</i>	4.0	3.4	1.7	2.0	1.7

Regioregular PCDTPT is synthesized by Dr. Ming Wang according to previous procedures<sup>65</sup> and was then separated into different MW fractions (30, 50, 80, 160, and 300 kDa) by gel permeation chromatography (GPC). The MW distributions and PDI are provided in **Figure 3.1** and **Table 3.1**. BGBC FETs are fabricated with the architecture “Si (500 μm) / SiO<sub>2</sub> (300 nm) / Au (50 nm) / decyltrichlorosilane / PCDTPT” by sandwich-

casting.<sup>116</sup> For comparison, FETs with the same architecture were made by drop-casting onto normal substrates (without surface grooves).

### ***3.2. Device Performance and Mobility Anisotropy***

**Figure 3.2** summarizes the carrier mobilities obtained from the FETs in the saturation regime as a function of MW. In Figure 3.2A, the average mobilities obtained by drop-casting without polymer chain alignment are 1.9, 1.3, 1.2, 0.7, 0.7 cm<sup>2</sup>/Vs for 300, 160, 80, 50, and 30 kDa, respectively. The mobility slightly increases with MW, which is in agreement with previous reports in the literature.<sup>67,132,133</sup> The mobility of devices prepared by sandwich-casting on nano-grooved substrates is significantly increased for all the MWs compared to that of drop-casting devices (Figure 3.2B). Most interestingly, those mobilities that are insensitive to MW. We find that polymer alignment induced by the nano-grooves is of principal importance to achieve high mobility. Figure 3.2C-D shows typical transfer and output curves of the PFETs fabricated from all the MWs. The transfer curve in Figure 3.2C shows non-linear behavior, which has been observed in other high mobility system.<sup>34-36</sup> It should be noted that the mobilities in Figure 3B were all obtained from the slope at lower V<sub>g</sub> in transfer curves (Figure 3.2C). The mobility variation as a function of gate bias is shown in **Figure 3.3**. This behavior is thoroughly investigated in chapter 5.

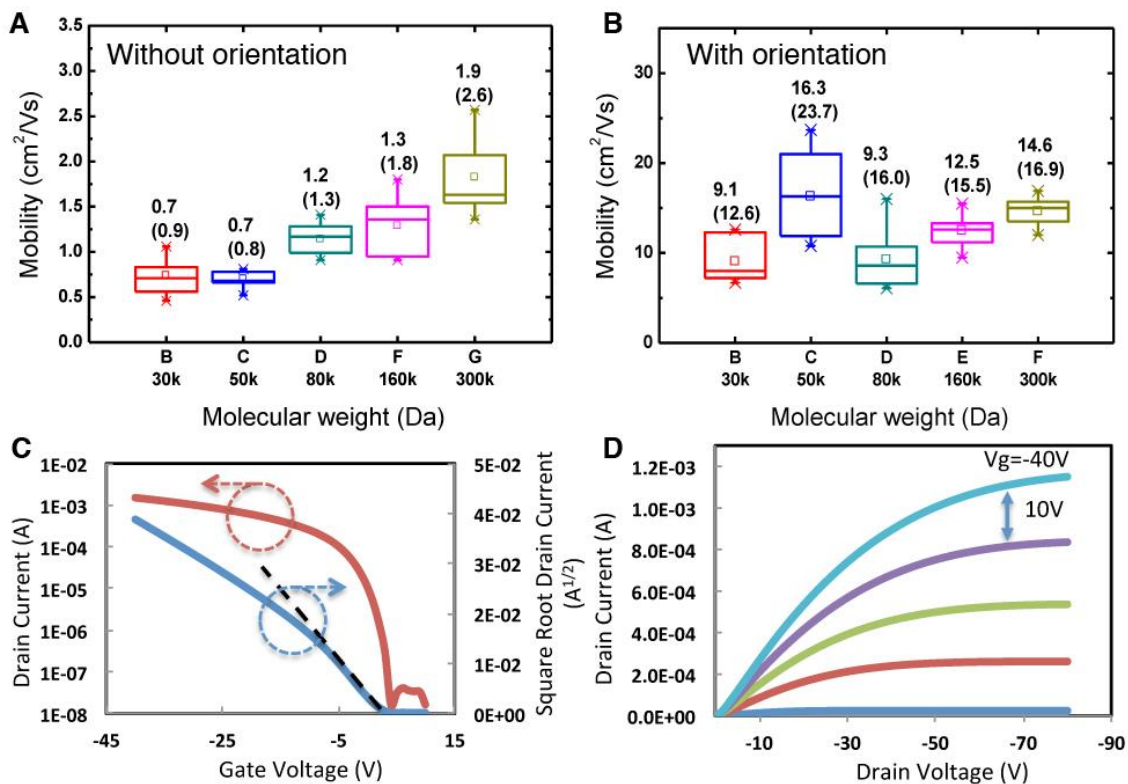


**Figure 3.2. Mobility of PCDTPT OFETs after annealing at 200 °C. The mobility value and the value in parentheses represent mean and maximum values obtained from 10 independent OFETs. (A) Devices fabricated by drop casting. (B) Devices fabricated by slow drying in the tunnel-like configuration. The horizontal lines in the box denote the 25th, 50th, and 75th percentile values. The error bars denote the 5th and 95th percentile values. The open square inside the box denotes the mean value. (C) and (D) FET characteristics of PCDTPT with mobility of 23.7 cm<sup>2</sup>/Vs. (L = 80 μm, W = 1 mm): (C) transfer curves taken at V<sub>DS</sub> = -80 V (D) output curves taken at various V<sub>G</sub> (0--40V).<sup>117</sup>**

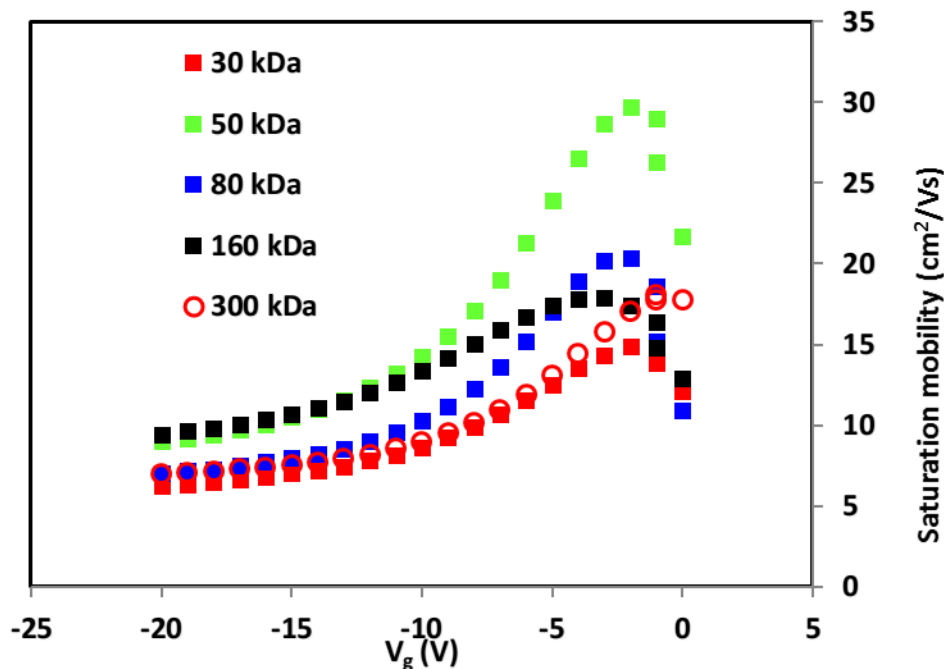


**Figure 3.3. Saturation mobility as a function of gate bias. The mobility is calculated from the local slope in the transfer curve at saturation regime  $I_{ds}^{1/2}$  versus  $V_g$  (equation 9).<sup>117</sup>**

The linear mobility is also calculated using equation (10) for the output curves around  $V_d = -5$  V (-2 V to -8V) and at  $V_g = -40$  V. It is 2.9, 4.7, 3.5, 5.5 and 5.0  $\text{cm}^2/\text{Vs}$  for the MW of 30, 50, 80, 160 and 300 kDa, respectively.<sup>117</sup> The linear mobility is several times lower than saturation mobility, which has been widely observed in the literature.<sup>114,138</sup>

### ***3.3. Polymer Chain Alignment of PCDTPT by High-Resolution AFM***

Atomic force microscopy (AFM) is utilized to understand the mobility variation with MW for both drop-casting and sandwich-casting devices. **Figure 3.4** shows the topography of the films made by drop casting on normal substrates. Nano-scale polymer fiber structures form for all MW fractions. The macroscopic morphology changes dramatically, however, from 300 kDa to low 30 kDa (Figure 3.4A-E). The polymer fiber structure is directionally

random for the high-MW PCDTPT (Figure 3.4A), whereas the fiber structures become discernible in crystalline domains for low MW polymers (Figure 3.4E,F). As seen in the AFM phase image of the 30 kDa polymer FET film, (Figure 3.4F), the polymer fibers within a domain are aligned over lengths approaching the micrometer scale. However, there are disordered grain boundary regions between domains. These create deep trapping sites for charge transport and thereby limit the carrier mobility.<sup>139</sup> As a result, the carrier mobility decreases as the MW decreases in these non-aligned polymer FETs.

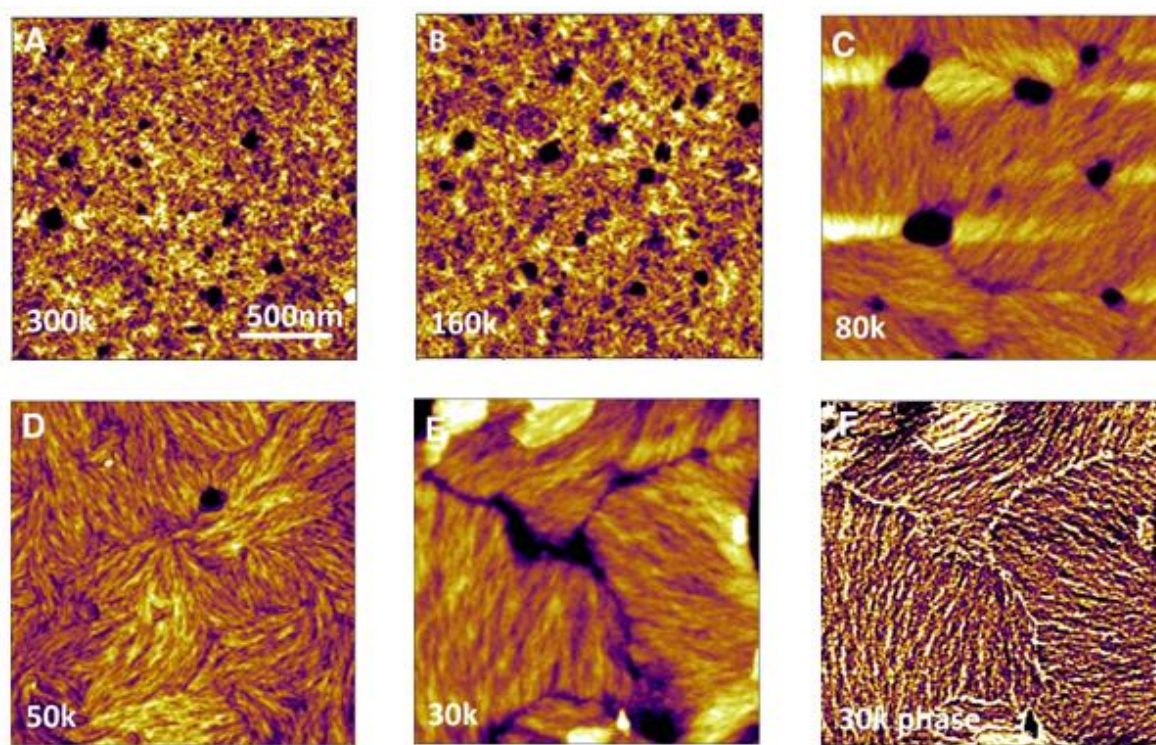


**Figure 3.4. AFM images of the PCDTPT topography by drop cast with MW of (A) 300, (B) 160, (C) 80, (D) 50, and (e) 30 kDa. (f) Phase image of the film with MW of 30 kDa. Data was obtained by Dr. Hsin-Rong Tseng.**

In a previous work, Dr. Hsin-Rong Tseng showed that polymer fibers was formed and aligned along the nano-grooves in devices prepared by sandwich-casting. Similar polymer

fiber alignments are observed for very thin films ( $<10\text{nm}$ ), shown in **Figure 3.5** for both 300 kDa and 50 kDa polymers. These ca. 50 nm wide fibers look like fiber bundles and seems to have finer structure inside. However, these finer structure are difficult to obtain in regular  $1\mu\text{m} \times 1\mu\text{m}$  AFM scan size.

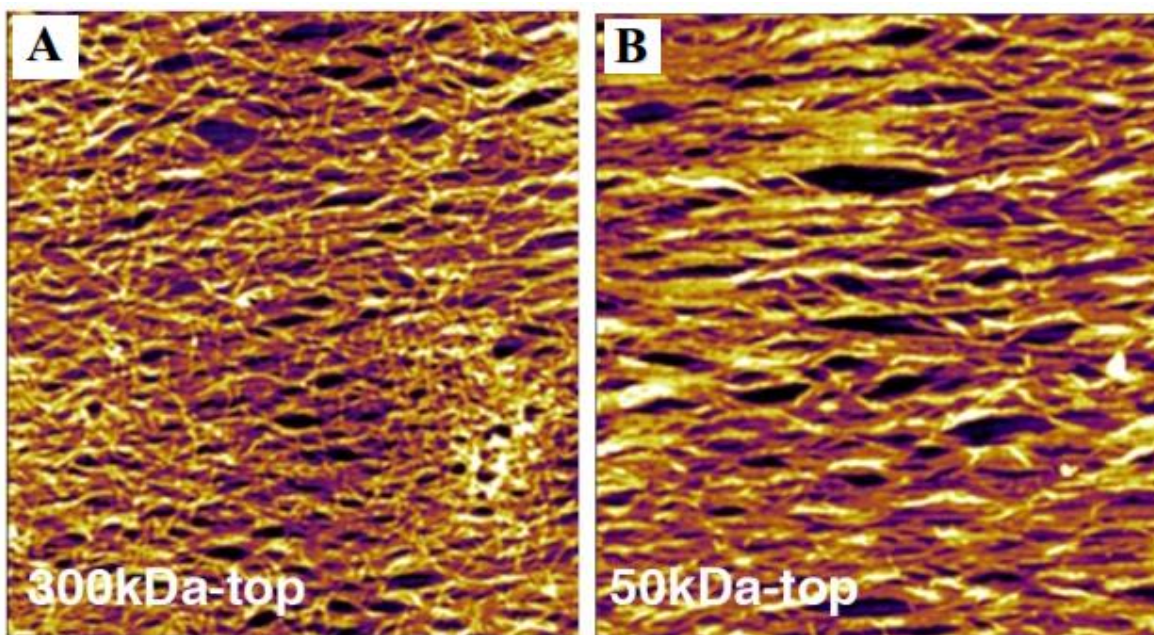


**Figure 3.5.** AFM images ( $1\mu\text{m} \times 1\mu\text{m}$ ) of PCDTPT topside morphology by slow-drying on nano-grooved substrates (with orientation): (A) MW=300 kDa and (B) MW=50 kDa. The height scale is 0 – 5 nm. Data was obtained by Dr. Hsin-Rong Tseng.<sup>117</sup>

PFETs with very thin films of polymers have mobilities of around  $10 - 15\text{ cm}^2/\text{Vs}$ , which is around 1.5 – 2 times lower than those mobilities presented in Figure 3.2B. Albeit giving slightly lower mobility, thin-film polymers are more feasible to perform high resolution AFM (HR-AFM) to reveal the fiber bundles in nanometer scale. Firstly, the regular scans are performed to find a good AFM tip with high contrast in both height and phase images.

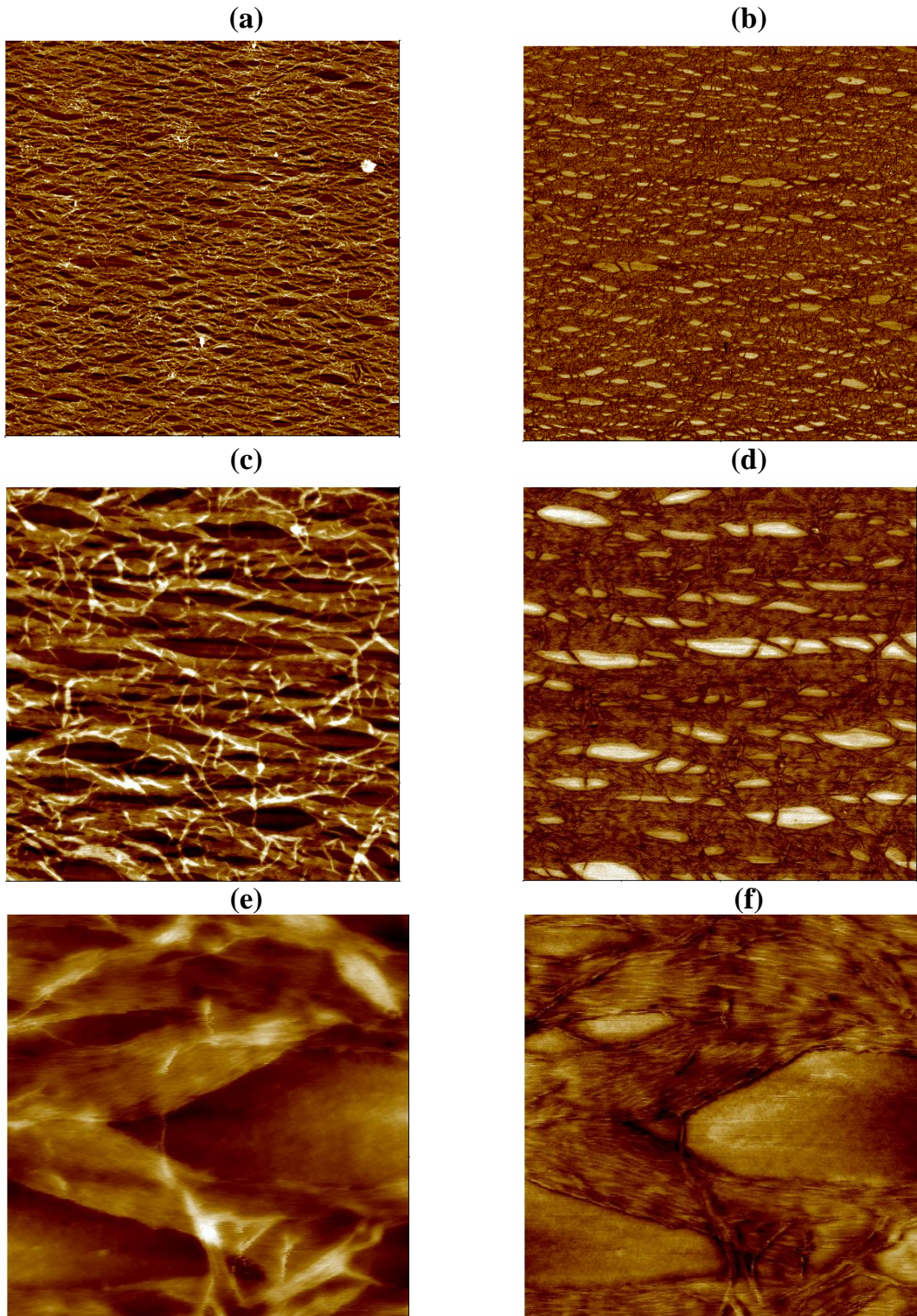


**Figure 3.6.** AFM images of PCDTPT FET on nano-grooved substrates at scan size of (a, b) 5  $\mu\text{m}$ , (c, d) 1  $\mu\text{m}$  and (e, f) 250 nm; a, c, e are topography images; b, d, f are phase image. The height scale is 0 – 5 nm and the phase scale is 0 – 20°.



Polymers with MW of 50 kDa and 300 kDa are used for HR-AFM study and both of them show similar results. **Figure 3.6** shows the height and phase images at different scan sizes of the film made from 300 kDa PCDTPT. It is clear that fibers are formed and well-aligned along the nano-grooves. Because the films are thin, the substrates are not fully covered by polymers. Bare substrates are clearly seen in the phase images.

The HR-AFM image ( $250 \text{ nm} \times 250 \text{ nm}$ ) of the topside morphology of 300 kDa MW film on nano-grooved substrates is further analyzed in **Figure 3.7**. The individual fibers are clearly aligned within the fiber bundles in the phase image in Figure 3A. There is no evidence of any “grain boundaries” in the fiber bundles, which is consistent with the high mobility observed. The width of individual fiber is  $\sim 2\text{-}3 \text{ nm}$  as shown by a cross-sectional AFM line cut surface profile in Figure 3B, and is comparable to the length of the repeat unit ( $\sim 2.4 \text{ nm}$ , Figure 3C). The only way for polymer chains to align is therefore along the fibers. In addition, the mobility is higher along the fiber and the optical absorption is anisotropic,<sup>116</sup> consistent with our hypothesis that carriers transport along the conjugated polymer backbone. The predominant intrachain charge transport in high-mobility semiconducting polymer has also been recently proposed using optical characterization.<sup>140</sup>

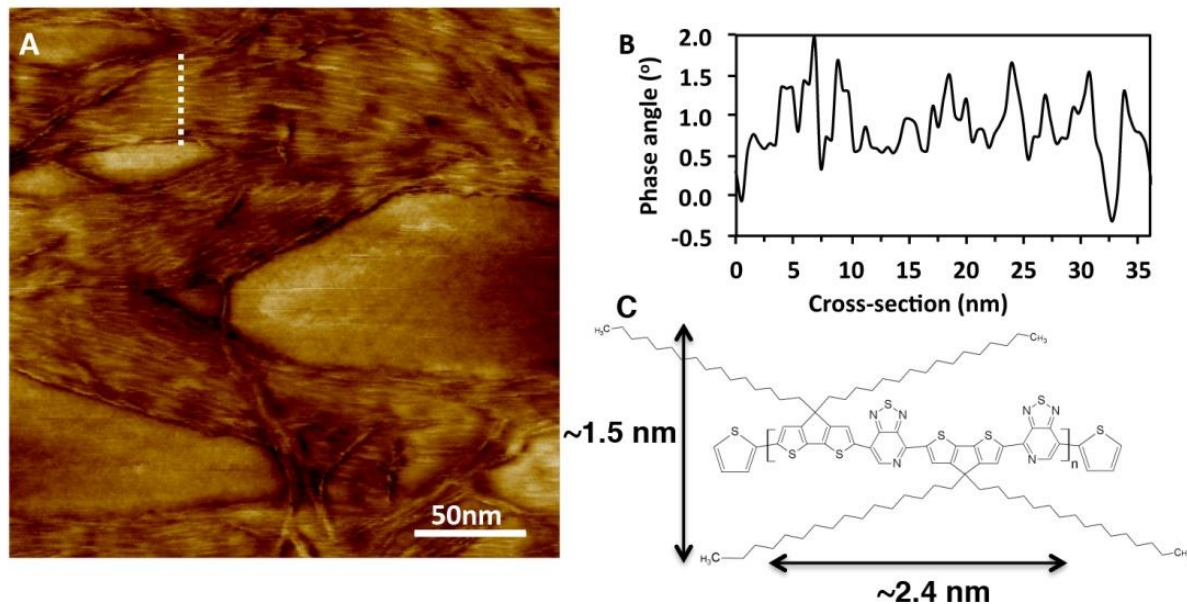


**Figure 3.7. (A) High resolution AFM (250 nm×250 nm) topside morphology phase image of PCDTPT 300 kDa OFET. (B) The cross-section profile of the dashed line in (A). (C) Molecular structure and estimated size of PCDTPT. The length of one monomer is approximately 2.4 nm and the width (including the side chains) is approximately 1.5 nm.**

The incomplete polymer coverage results in a slightly lower mobility in PFETs of PCDTPT. In order to increase the film thickness and surface coverage, the whole tunnel in sandwich-casting technique is tilted with an angle of around 13°. The gravitation makes the film at the bottom half of the substrate thicker. The highest mobilities are obtained with thick-film OFETs. Interestingly, the polymer fibers are not aligned on the top surface of the thick film (~ 50 nm), shown in **Figure 3.8a**. We hypothesize that the alignment only happens at the first few nanometers of the polymer right on top of the nano-grooves. This is enough to enhance the charge carrier mobility because charge transport in TFTs occurs at a few nanometers above the dielectric surface. In order to prove that, we use HF to etch the SiO<sub>2</sub> dielectric to flip the bottom surface on another substrate to perform AFM. It turns out

the hypothesis is true: polymer fibers of PCDTPT aligned at the bottom surface, revealed in **Figure 3.8b**. Obtaining high-quality images of the bottom surface is challenging due to the surface distortion during the etching process.

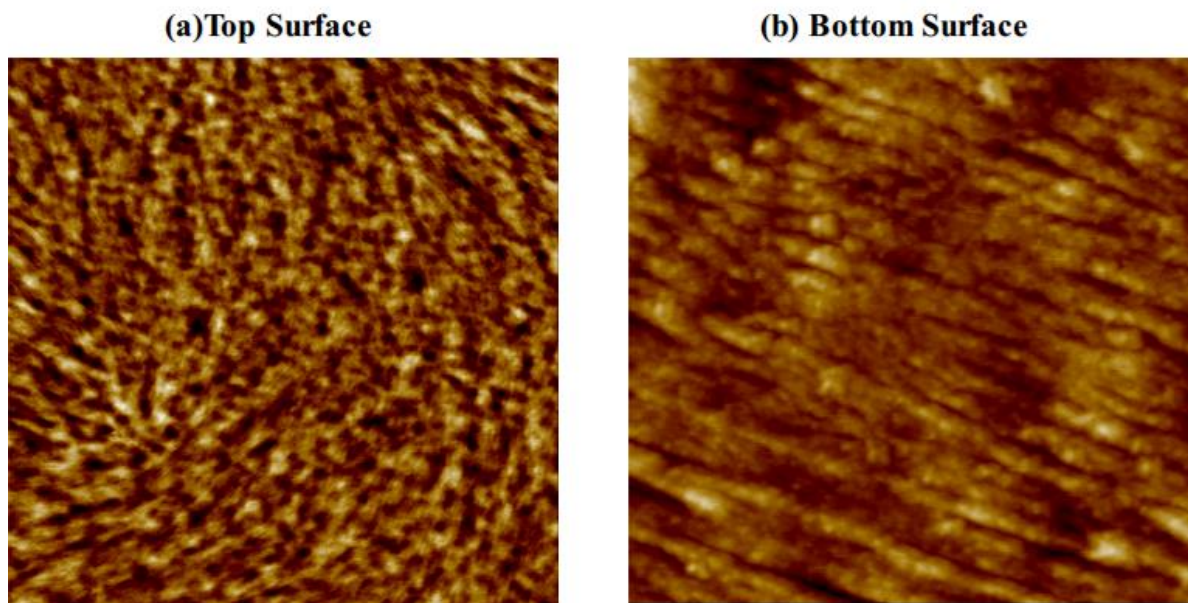


**Figure 3.8. AFM images of (a) top surface and (b) bottom surface of 50 nm PCDTPT films in PFETs with high mobilities shown in Figure 3.2.**

Finally, we manage to obtain HR-AFM of the bottom surface to show the alignment of single small fiber formation (**Figure 3.9**). It clearly shows that the fiber is aligned in one direction. The single fiber width is around 2.5 nm (**Figure 3.9c**), which is consistent with the one we observed on the top surface of the thin films.

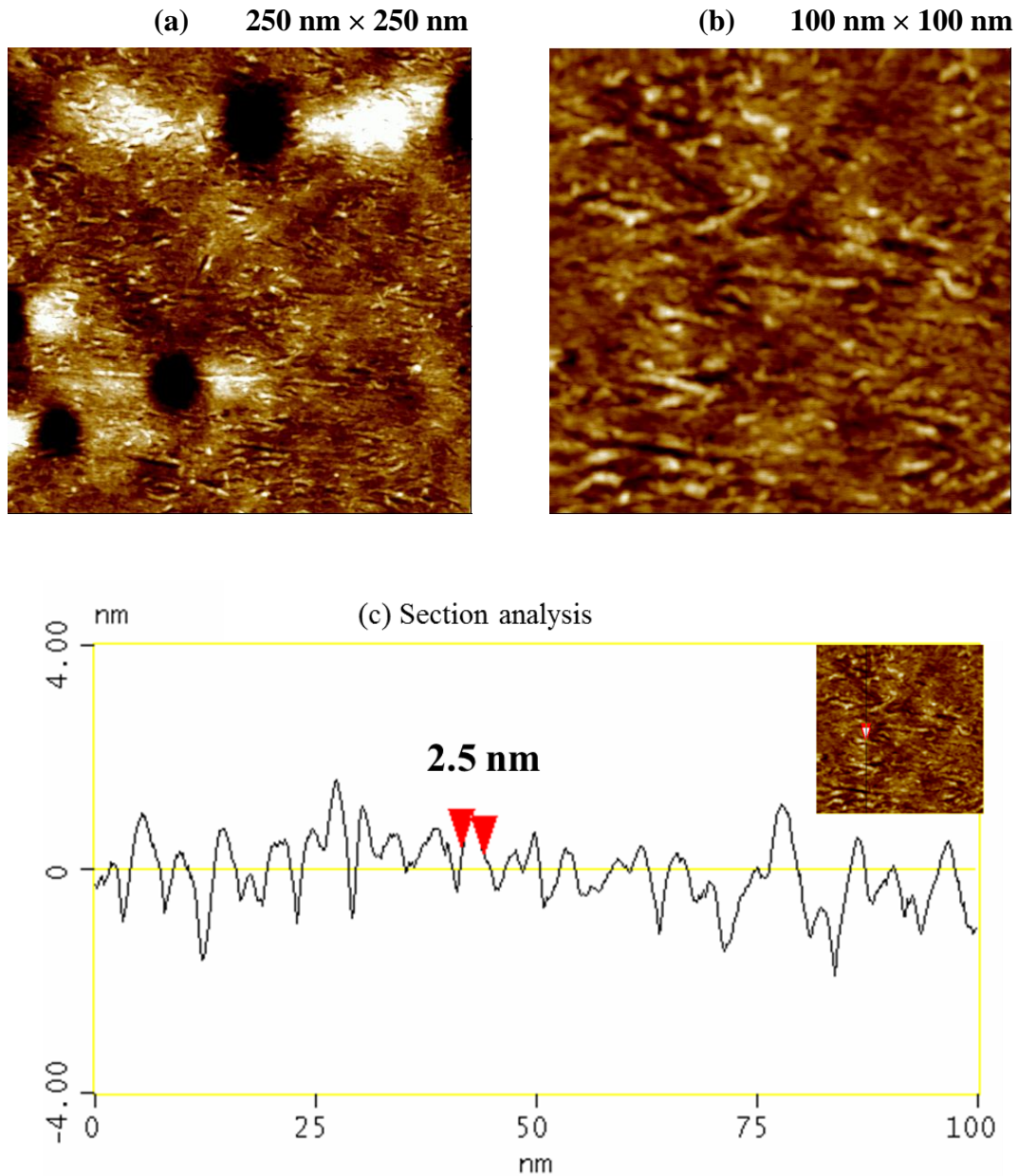


**Figure 3.9. (a-b) High resolution AFM image of bottom surface of a PCDTPT device with mobility  $\sim 12 \text{ cm}^2/\text{Vs}$  (MW 50 kDa, 0.25 mg/ml, sandwiched devices of nano-grooved substrate, anneal at 200 C in 8 minutes). (c) Section analysis of a line-cut of 100 nm × 100 nm showing full-width half-max (FWHM) of a peak (representing a single fiber) of  $\sim 2.5 \text{ nm}$ .**

### 3.4. Polymer Chain Alignment of PCDTPT by Transmission Electron Microscopy

The orientation of the films cast on the nano-grooved substrates was further investigated by transmission electron microscopy (TEM) using electron diffraction (ED); and presented in **Figure 3.10**. With the electron beam orthogonal to the film ( $0^\circ$  tilt angle, Figure S4A), the ED pattern consist of very sharp reflections corresponding to the (010)  $\pi$ - $\pi$  stacking of the crystalline lattice. The angular spread of the (010) reflection in the plane of the film indicates that all the polymer backbone axes of the polymer crystallites are oriented within  $\pm 12^\circ$  of the alignment axis. With the sample tilted  $70^\circ$  (Figure S4B), the ED pattern shows exceptional alignment as indicated by the very sharp reflections corresponding to the alkyl side-chain packing (100) of the crystalline lattice. The ED results indicate the aligned polymer chains have an “edge-on” orientation relative the scratched substrates. Overall, these results provide further evidence that the alignment of the polymer chains plays a crucial role in enhancing the mobility.

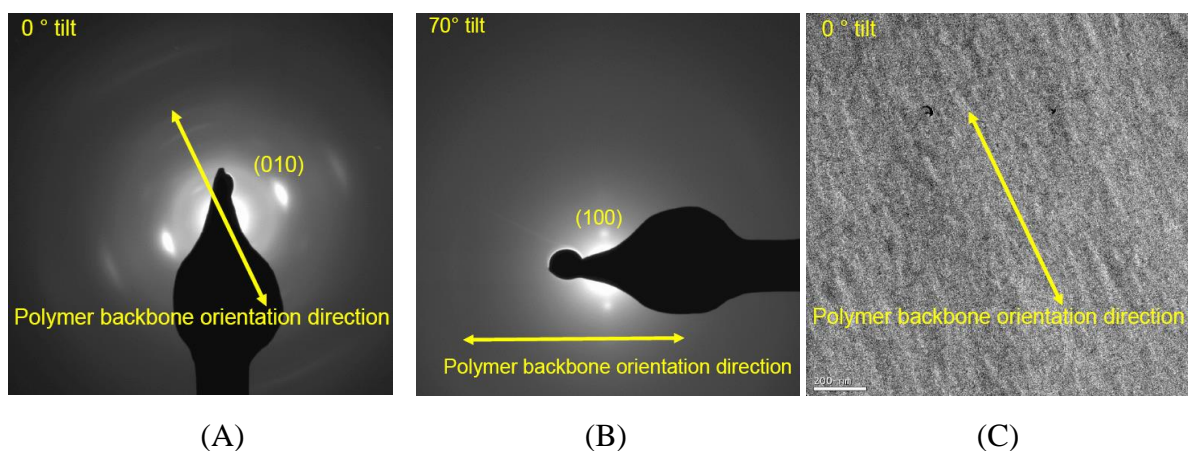


**Figure 3.10. Electron diffraction patterns (A) at  $0^\circ$  tilt and (B) at  $70^\circ$  tilt. (C) Bright field transmission electron micrograph showing elongated structures along the alignment direction. Data was obtained by Dr. Shrayesh Patel.<sup>117</sup>**

### ***3.5. Conclusion***

To summarize, hole mobility higher than  $10.0 \text{ cm}^2/\text{Vs}$ , for transport predominantly along the conjugated chain is demonstrated with aligned PCDTPT. The mobility of PFETs with long-range-order aligned polymer fibers is about an order of magnitude higher than that of non-aligned-polymer PFETs. More importantly, the mobility PFETs with long-range-order aligned polymer fibers is insensitive to MW and therefore very high MW is not necessary for achieving high mobility. With optimization, AFM can be a powerful tool to visualize polymer fiber at the length scale of a few nanometers. Polymer chain fiber alignment, shown by HR-AFM, facilitates carrier transport along the conjugated polymer backbone with occasional hopping to neighboring chains through  $\pi$ - $\pi$  stacking. The hopping mechanism is further investigated in the following chapter, chapter 4.

## **4. Thermally Activated Charge Transport in High-mobility OFETs Fabricated from D-A Polymers**

### ***4.1. Introduction***

Understanding charge transport mechanism in electronic devices is essential to control the device operation and improve the device performance. The correct physical description of the charge carriers and the mechanism of charge transport in organic semiconductors, particularly in high-mobility conjugated polymer system are still under controversial.<sup>39,76,80,64</sup> Charge transport in low-mobility, disorder OSCs, which has been widely investigated from studies on xerographic amorphous OSCs, is limited by the disorder in thin films. The conduction is therefore driven by the thermally assisted hopping of localized charge carriers from one site to another in an energetically disorder landscape. On the other hand, the classical band-like, Bloch electron conduction well describes the charge transport in crystalline inorganic semiconductors, which usually has mobility higher than  $100 \text{ cm}^2/\text{Vs}$ .<sup>1</sup> High-mobility conjugated polymers has the mobility between these two regimes ( $> 10 \text{ cm}^2/\text{Vs}$ ).<sup>141,142</sup> Therefore, a thorough understanding of charge transport mechanism and factors that limit carrier mobilities in the high-mobility regime of conjugated polymer is crucial for not only designing better performance molecules but also the controlling of manufacturing process in industrial scale.

In this chapter, the charge transport mechanism of PCDTPT FETs is analyzed and correlate with the morphology in Chapter 3 to build a model for charge transport in the high-mobility PFETs with aligned polymers.

#### ***4.2. Water effect in the analysis of temperature-dependent measurements***

In order to study the charge transport mechanism of PFETs, mobility is measured as a function of temperatures from 300 K to 80 K. Ideally, for thermally activated hopping process, the mobility-temperature relationship for the whole range of temperatures should be able to be described by Arrhenius equation. However, it has been reported in the literature that a trace amount of confined water can cause an anomaly at around 200 K. For OFETs, Stalinga and coworker observed the anomaly in the temperature dependent current and mobility of oligothiophene and polythiophene devices.<sup>83,143,144</sup> The anomaly can be reduced by processing the device in water-free environment but cannot be removed. They also hypothesized that the confined water trapped in the organic layer does not crystallize at 273 K but forms a metastable liquid causing the anomaly. In chapter 5, the metastable water is shown to act as traps and cause the shift in threshold voltage after multiple scans. At around 200 K to 220 K metastable water solidifies. Therefore, at temperature below 200 K, this water effect disappears. The effect of water in charge transport and charge trapping of OLEDs, hole-only diodes and electron-only diodes has also been reported. Blom and coworkers observed a common electron trap with similar trap density in devices made from different conjugated polymers.<sup>145,146,71</sup> It happens for devices that are completely processed in the N<sub>2</sub> glovebox and measured under high vacuum. This common electron trap is hypothesized to be a complex of a trace amount of water and oxygen in the organic semiconductor films.



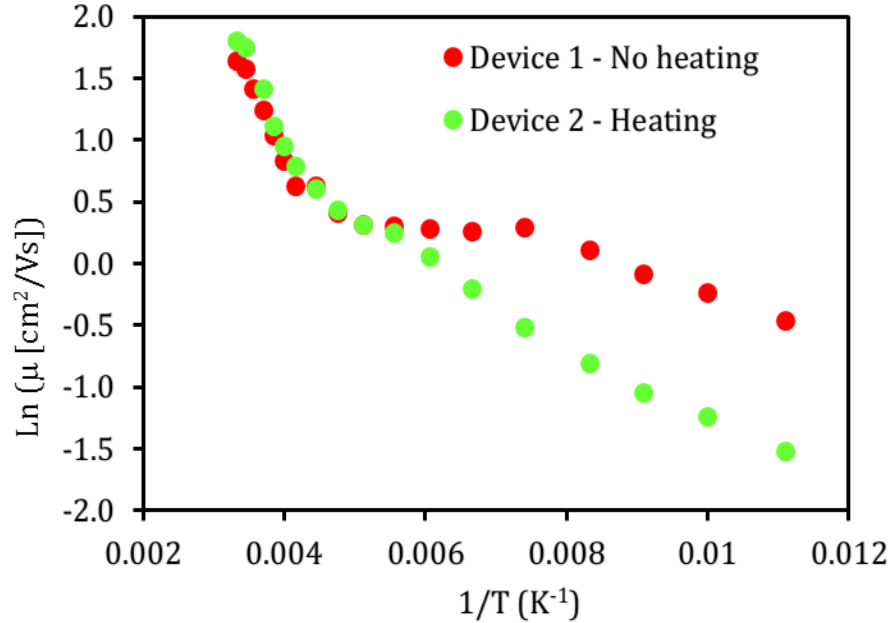


**Figure 4.1. Temperature-dependent mobility of PCDTPT FETs with and without heating (at 400 K in 7 hours) in high vacuum ( $<10^{-6}$  torr)**

Figure 4.1 shows temperature-dependent mobility of two devices prepared by same conditions (nano-grooved substrates, PCDTPT MW 300 kDa, 0.25 mg/ml, sandwich-casting, anneal at 200 C in 8 minutes). Device 1 was conducted temperature-dependent measurements right after preparing while device 2 was heated at 400 K in 7 hrs in high vacuum ( $<10^{-6}$  torr) in the probe station before being conducted the measurement. It clearly shows that, after heating the device in UHV, the plateau around 220 – 180 K of device 2 becomes insignificant. We hypothesize that the removing of residual water in the device upon heating is attributed for the phenomenon.

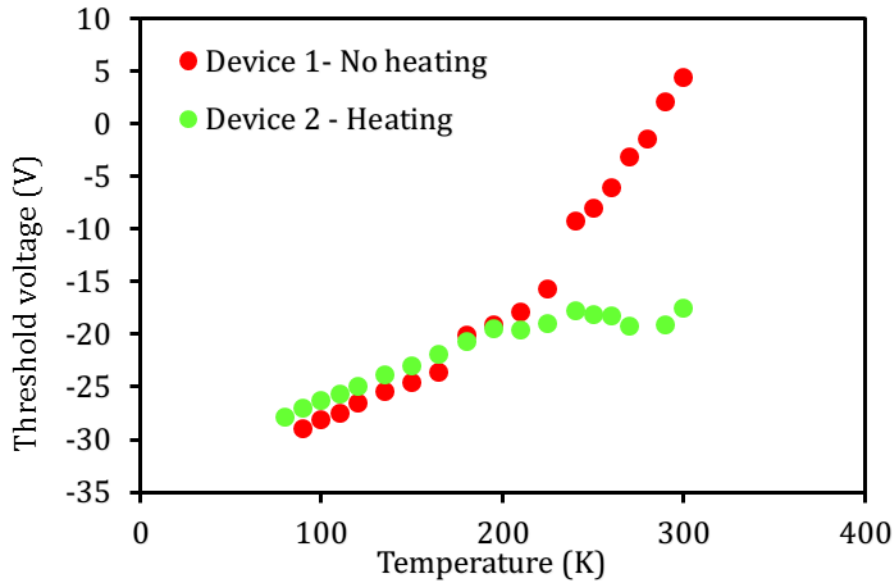


**Figure 4.2. Threshold voltage shift as a function of temperature of PCDTPT FETs with and without heating (at 400 K in 7 hours) in high vacuum ( $<10^{-6}$  torr)**

Another interesting observation after removing water is the change in threshold voltage as temperature decreases. For the device without heating, the threshold voltage negatively shifted dramatically from 300 K to 240 K, while in the device with heating, it remained relatively constant. It suggests that the dynamic interaction of residual water with the OFET polymer layer changes as the system is cooling down before the transformation of water. Below 200 K, the shift in threshold voltage is similar in both devices. With these observations, all the following temperature-dependent measurements are performed after the devices are heated at 400 K in vacuum for at least 7 hours.

#### ***4.3. Investigating Activation Energy by Temperature-dependent Measurements***

The effect of molecular weight of PCDTPT on activation energy was evaluated by using three GPC fractionated molecular weight  $M_n$  50 kDa, 180 kDa and 300 kDa. Devices from three MWs are prepared and tested in the same conditions (nano-grooved substrate, 0.25

mg/ml concentration, sandwich-casting, anneal at 200 C in 8 minutes, heat 7hrs in UHV before measuring). Transfer and output curves of all the devices at all temperature were normal and showed similar trend as temperature decreases. The transfer curves in saturation regime (at  $V_d=-50V$ ) of the 50 kDa PCDTPT device at different temperatures are shown in **Figure 4.3**. Mobilities are calculated from transfer curves in both linear and saturation regimes and plotted with inverse temperature, according to the Arrhenius law, to investigate the charge transport mechanism.

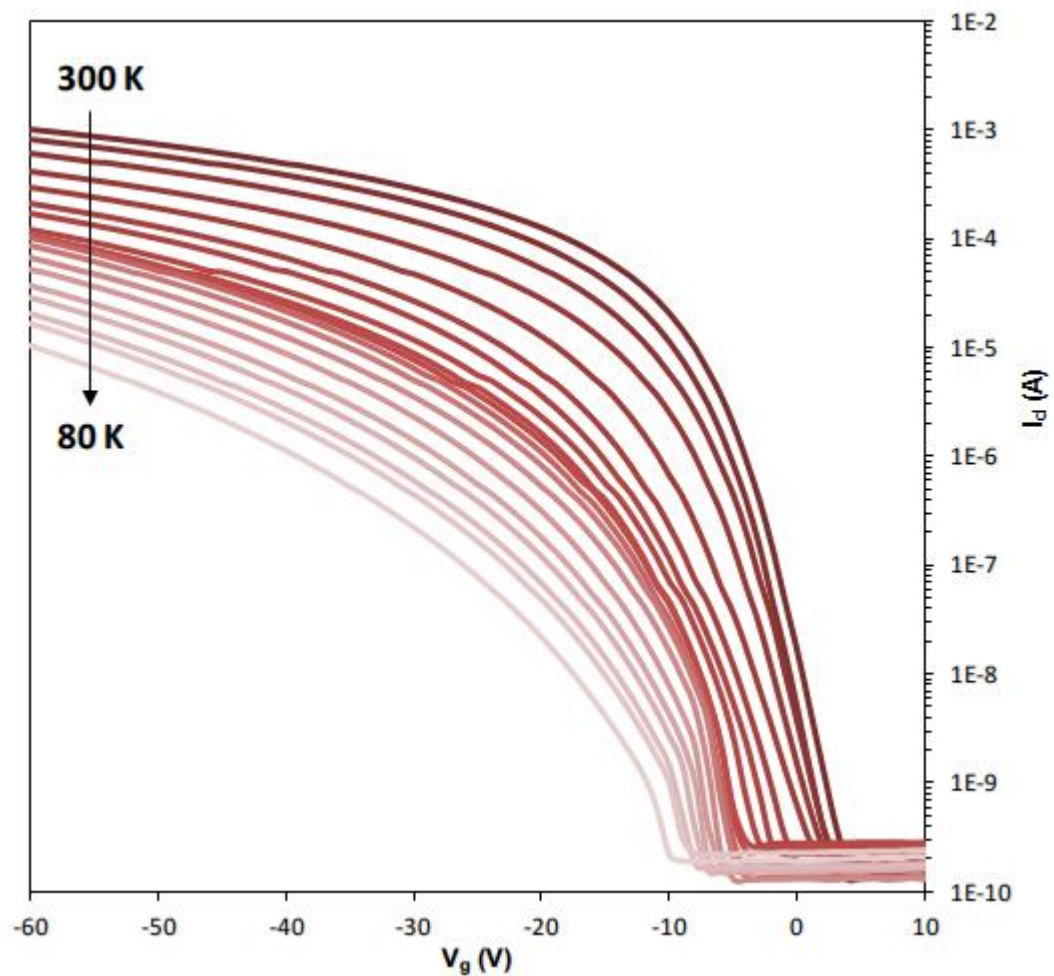


**Figure 4.3.** Transfer (at  $V_d=-50V$ ) curves of the 50 kDa PCDTPT PFET at different temperatures.

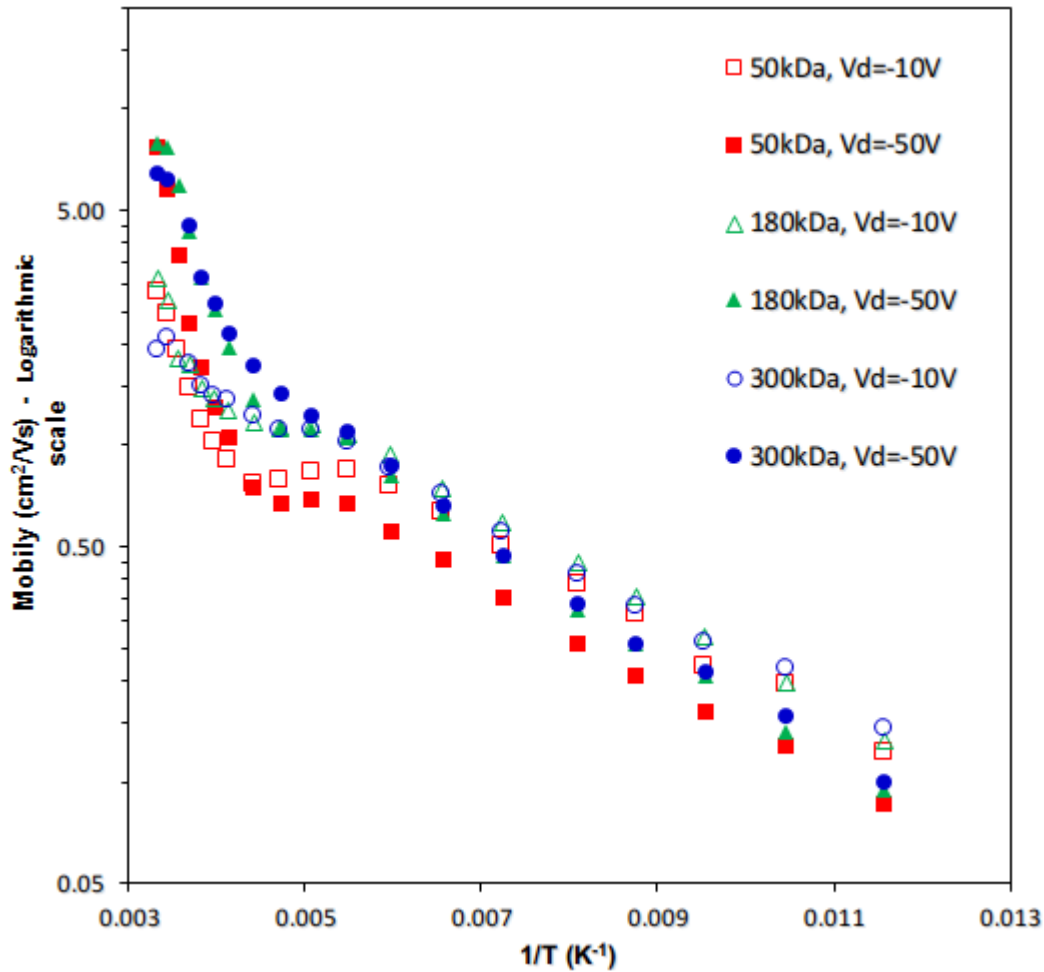


**Figure 4.4. Temperature-dependent mobility for the PCDTPT PFETs with MW of 50, 160, and 300 kDa.**

Temperature-dependent mobility in both linear (at  $V_d=-10V$ ) and saturation regime (at  $V_d=-50V$ ) of OFETs with MW of 50, 160, and 300 kDa materials aligned on nano-grooved substrates is presented in **Figure 4.4**. In all the cases, the mobility decreases as temperatures decreases, which indicates the thermally activated hopping transport mechanism. Considering the dimension of the PFETs, that charge transport in PCDTPT FETs is limited by thermally activated hopping is reasonable. In fact, perfect chain alignment in an PFET with channel width of  $1000\ \mu m$  and channel length of  $10 - 160\ \mu m$  is very

unlikely. Even though X-ray diffraction, AFM and TEM show perfect alignment and tight  $\pi$ - $\pi$  stacking of polymer chains in the films, diffraction techniques only probe the crystalline portions of the films with periodic stacking.

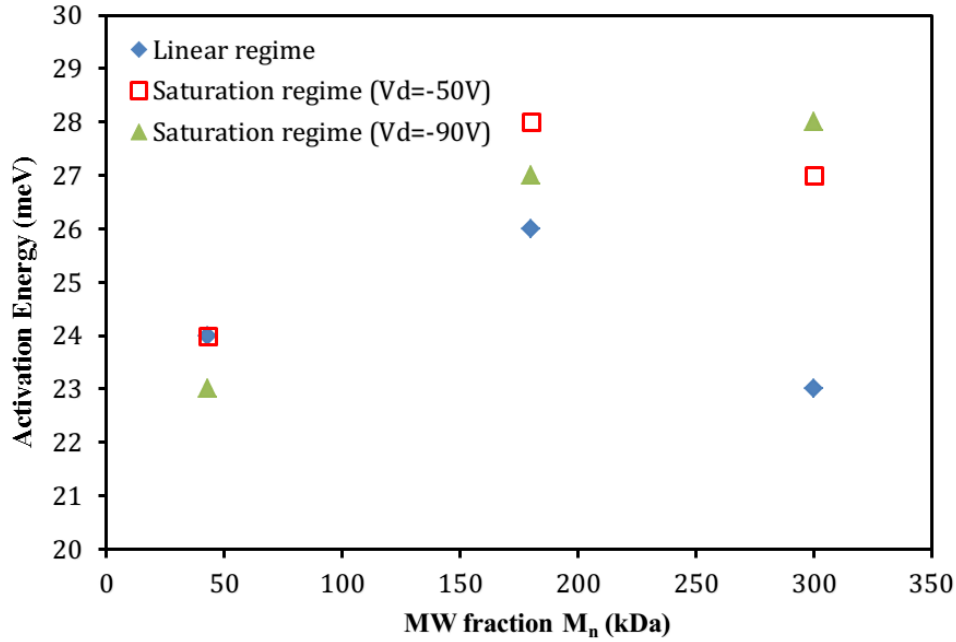


**Figure 4.5. Activation energy of three MW fractions of PCDTPT**

It is clear that the temperature-dependent mobility at both linear and saturation regime (at both  $V_d=-50V$  and  $-90V$ ) of all MW is not significant (**Figure 4.5**). In all the cases, the activation energy varies in a narrow range of 22-30 meV, as extracted in the temperature range from 85K to 180 K. This variation in activation energy is very small considering the fact that thermal energy at 300 K is 26 meV. The nonlinear behavior of the mobility near and above 200 K could result from the bias stress<sup>85</sup> or residual moisture in the film.<sup>144,147,148</sup> The activation energy is low, compared to most other high-mobility polymers,<sup>149,88,150,151</sup> implying that the inter-chain carrier hopping is efficient. The low activation energy is consistent with the observation that there are no grain boundaries from chain-to-chain or fiber-to-fiber.<sup>134</sup> The MW-independent  $E_a$  indicates the similar energetic barrier of hopping

in three MWs. This barrier probably correlates to the  $\pi$ - $\pi$  stacking distance of the polymer assembly in thin films. In order to characterize the  $\pi$ - $\pi$  stacking distance as well as other order parameters of PCDTPT thin films, grazing incidence wide-angle X-ray diffraction (GIWAXS) is characterized and presented in section 4.4.

Next, activation energy of PDCTPT PFETs on normal substrates and nano-grooved substrates (for both parallel and perpendicular devices) is tested. **Table 4.1** summarizes the activation energy of the three devices (nano-grooved substrates, PCDTPT MW 300 kDa, 0.25 mg/ml, sandwich-casting, anneal at 200 C in 8 minutes) at both linear regime and saturation regime. Interestingly, the activation energies of different devices (normal substrate, nano-grooved substrate parallel and perpendicular) are similar, even though the mobility can vary by an order of magnitude (0.2 – 6.1 cm<sup>2</sup>/Vs). This implies that the conduction pathway is similar in all devices. As mentioned in section 3.5, this conduction pathway is primarily along the conjugated polymer backbone with occasional hopping to neighboring chains through  $\pi$ - $\pi$  stacking.<sup>117</sup> It should be noted that in our device processing condition, PCDTPT polymer assemble in fibers in all devices. In the devices on normal substrate, the fibers align in random direction while in the devices on nano-grooved substrates the fibers are either more parallel (parallel devices) or perpendicular (perpendicular devices) to the electrical field from source to drain. In addition, the fibers are not perfectly aligned in one direction; there are some cross-talks fibers in the other directions. Carriers overcome a similar energetic barrier, correlates to the similar  $\pi$ - $\pi$  stacking distance of the polymer assembly in thin films for the three devices.<sup>65,117,152</sup> However, carriers transport in different route distance depending on the alignment of the fibers, resulting in different calculated mobility.

**Table 4.1. Summary of activation energy PDCTPT PFETs on normal substrates and nano-grooved substrates (for both parallel and perpendicular devices)**

<b>Device characterization</b>	<b>Normal substrate</b>	<b>Nano-grooved substrate - parallel</b>	<b>Nano-grooved substrate - perpendicular</b>
Saturation mobility at 300K (cm <sup>2</sup> /Vs)	0.2 – 0.4	1.5 – 6.1	0.6 – 1.0
Activation energy - Linear regime (meV)	33 ± 5	27 ± 5	28 ± 6
Activation energy - Saturation regime (meV)	32 ± 5	30 ± 5	29 ± 6

#### ***4.4. Characterizing Molecular Stacking by GIWAXS***

A summary of GIWAXS results for PCDTPT with MW of 30, 50, 80, 160, and 300 kDa is summarized in **Figure 4.6**. Firstly, scattering intensities are plotted as a function of the scattering vector ( $q$  (nm<sup>-1</sup>)) in **Figure 4.6A**. The two length scale regimes commonly investigated in conjugated polymer thin films are from  $q \sim 1$ -10 nm<sup>-1</sup>, which corresponds to the lamellar side chain packing and backbone, and the  $q$  range of  $\sim 12$ -20 nm<sup>-1</sup> describing the  $\pi$ -  $\pi$  stacking between ordered polymer segments.<sup>153</sup> The positions of the peaks are the same for all the MWs, which means that the MW does not affect the final structure that is formed; however the full width at half-maximum (FWHM) of the alkyl stacking peaks shows a MW dependence.

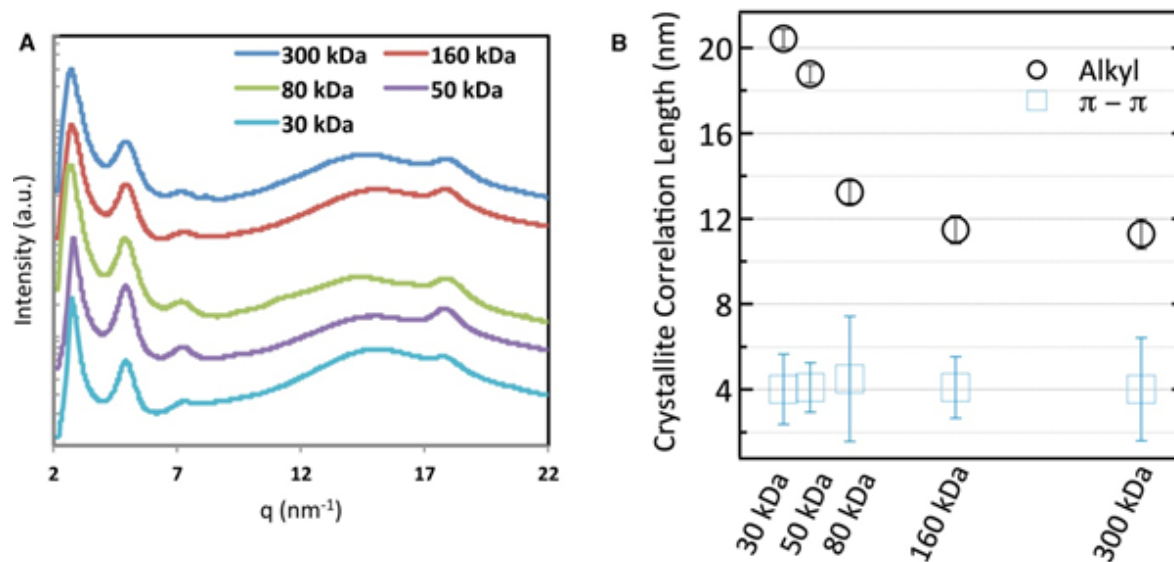


**Figure 4.6. (A) Grazing wide-angle X-ray scattering line profiles of PCDTPT films formed by drop casting. (B) Estimated crystallite correlation length of alkyl and  $\pi$ - $\pi$  stacking.**

The crystalline correlation length (CCL) of alkyl and  $\pi$ - $\pi$  stacking were estimated by the Scherrer equation and the data are shown in **Figure 4.6B**.<sup>117,152</sup> The CCL of alkyl stacking changes from 20 nm for 30 kDa to 11 nm for 300 kDa polymer fraction. On the other hand, the CCL of  $\pi$ - $\pi$  stacking is  $\sim 4$  nm for all MWs. The independence on the MW of the CCL of  $\pi$ - $\pi$  stacking, in combination with the MW-independent activation energy shown in Figure 4.5, supports the result that carrier transport is predominately along the backbone of the chain with occasional hopping through  $\pi$ - $\pi$  stacking to a neighboring chain, followed again by transport along the backbone. In this way the mobility is insensitive to MW and high mobility can be achieved after long-range polymer alignment.



#### ***4.5. Conclusion***

The temperature-dependence of the mobility are investigated for PCDPT PFETs with different MWs and on different substrates. In all the cases, the mobility is thermally activated with an activation energy  $\sim 30$  meV, as extracted in the temperature range from 85K to 180 K. The nonlinear behavior of the mobility near and above 200 K could result from the bias stress or residual moisture in the film. The activation energy is low, compared to most other high-mobility polymers, implying that the inter-chain carrier hopping is efficient. The low activation energy is consistent with the observation that there are no grain boundaries from chain-to-chain or fiber-to-fiber, observed from AFM in chapter 3. The MW-independent activation energy is in agreement with the MW-independent mobility and fiber alignment presented in chapter 3.

## 5. Electrical Instability and Non-ideality of OFETs Fabricated from Low Band-gap Polymers

### 5.1. Introduction

Electrical stability and charge mobility are two important parameters of organic field-effect transistors (OFETs) that needed to be improved in order to be commercialized in large-scale production.<sup>30,91,92</sup> Recently, the carrier mobility of solution-processed polymer FETs (PFETs) has been impressively improved by virtues of molecular designs and device engineering.<sup>67,117,124,154,155</sup> One common route of achieving high mobility PFETs is utilizing donor-acceptor (D-A) alternating structure. The D-A structure has been reported to enhance molecular interactions and shorten  $\pi$ - $\pi$  stacking distance, which consequently reduce energetic barriers for hopping and increase charge mobilities.<sup>67,124,156</sup> The stabilization of the resonance structure by adapting D-A motif results in the reduction of the energy gap between the highest occupied molecular orbital (HOMO) and the lowest unoccupied molecular orbital (LUMO) of the polymer. On one hand, this reduction is beneficial to obtain ambipolar and n-type PFETs. On the other hand, it introduces undesirable ambipolarity in unipolar p-type PFETs, which results in the increase of OFF current and the dependence of turn on voltage on drain bias.<sup>157</sup> More importantly, p-type OFETs are usually biased in electron accumulation regime in order to switch off. The electron injection and trapping occurred in p-type OFETs under OFF state could alter the device characteristics when it is switched back to ON state.<sup>44</sup> Another puzzling observation in several high-performing D-A copolymers in bottom gate FETs with SiO<sub>2</sub> gate dielectric is the double-slope in saturated transfer curves ( $I_d^{1/2}$  vs.  $V_g$ ) – high slope at small gate voltage but decreases with increasing

magnitude of the gate voltage.<sup>117,124,64,155,158</sup> To further develop materials and device engineering for high performance PFETs for practical applications, the effects of ambipolarity on the charge transport, charge trapping and especially the double-slope of p-type PFETs should be addressed.

In this chapter, the mechanism of the electrical instability of p-type PFETs with a certain degree of ambipolarity is investigated. The work helps to unravel the effect of electron conduction on the stability of hole current and the double-slope behavior. The model polymer still the low bandgap D-A polymer PCDTPT (**Figure 2.1**).<sup>65,116,117,155</sup> The polymer has an energy gap of 1.2 eV, HOMO of ~5.2 eV and LUMO of ~4.0 eV, characterized by cyclic voltammetry and optical absorption.<sup>65</sup> This PFET system was chosen because it has been shown to have high field effect hole mobility and double-slope in saturated transfer curves, presented in chapter 3.<sup>117,155</sup> While performing current-voltage (I-V) measurement, we found that consecutive sweeping of gate voltage changed the shape of the transfer curves. We conducted a thorough study of bias-stress of the system and found that electron trapping at the gate dielectric/polymer interface greatly alters the device characteristics including the occurrence of the double-slope. We indirectly proved that a trace amount of water trapped in OFETs and silanol groups on SiO<sub>2</sub> surfaces may be attributed to this electrical instability of the devices.

## 5.2. Electrical Instability and Double-Slope of PCDTPT FETs

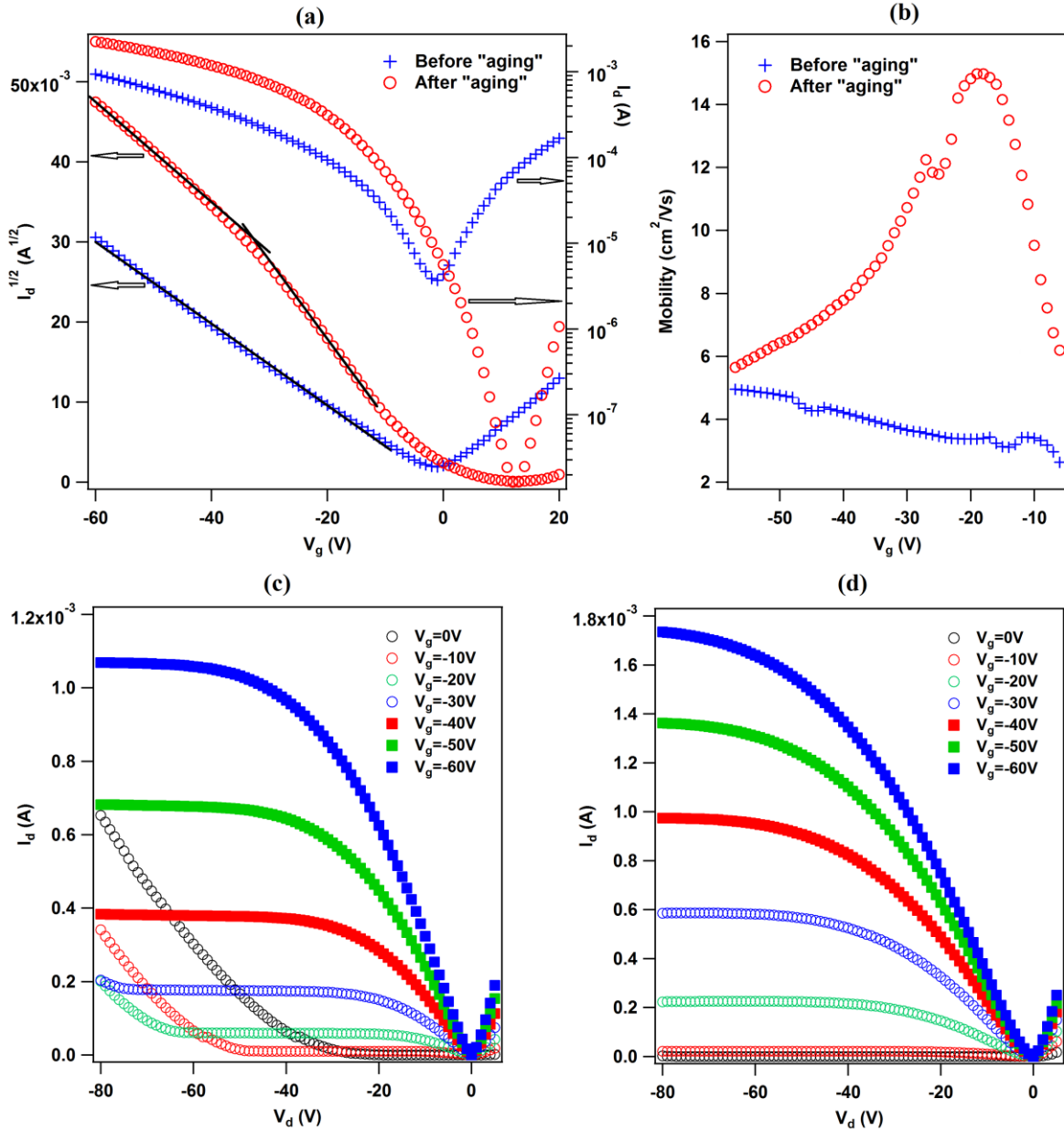


**Figure 5.1.** (a) Transfer characteristics of the PCDTPT PFET at  $V_d = -80$  V before and after bias-sweeping gate voltages from 20 V to -60 V in approximately 5 minutes (also called aging); (b) Gate-dependence saturation mobility extracted from I-V curves in (a); (c) and (d) Output curves before and after bias-sweeping effect. Device structure: Si/SiO<sub>2</sub>/Au/DTS/PCDTPT

**Figure 5.1** demonstrates the effects of the continuous bias-sweeping on the device performance of the bottom-gate bottom-contact PCDTPT FETs using SiO<sub>2</sub> as dielectrics. In this study, SiO<sub>2</sub> surface were treated with self-assemble monolayer (SAM) of decyltrichlorosilane (DTS) (**Figure 2.3**), unless otherwise stated.<sup>116,117</sup> Silane SAM has been proved to significantly reduce electron traps on the surface of SiO<sub>2</sub>, but not completely.<sup>98</sup> The devices were fabricated by sandwiched- casting the polymer solution onto nano-grooved substrates.<sup>117</sup> The first transfer (**Figure 5.1a, blue**) and output curves (**Figure 5.1c**) of the devices show strong ambipolarity.<sup>157,159</sup> N-type scan of the devices at positive V<sub>d</sub> and V<sub>g</sub> shown in **Figure 5.2** proved the unarguable electron injection in this device structure. More importantly, no non-ideality is observed in the transfer characteristics of hole current vs. gate voltages. A perfect linear relationship of the square root of drain current and gate voltages is ideal for the saturation regime, described in equation (8).

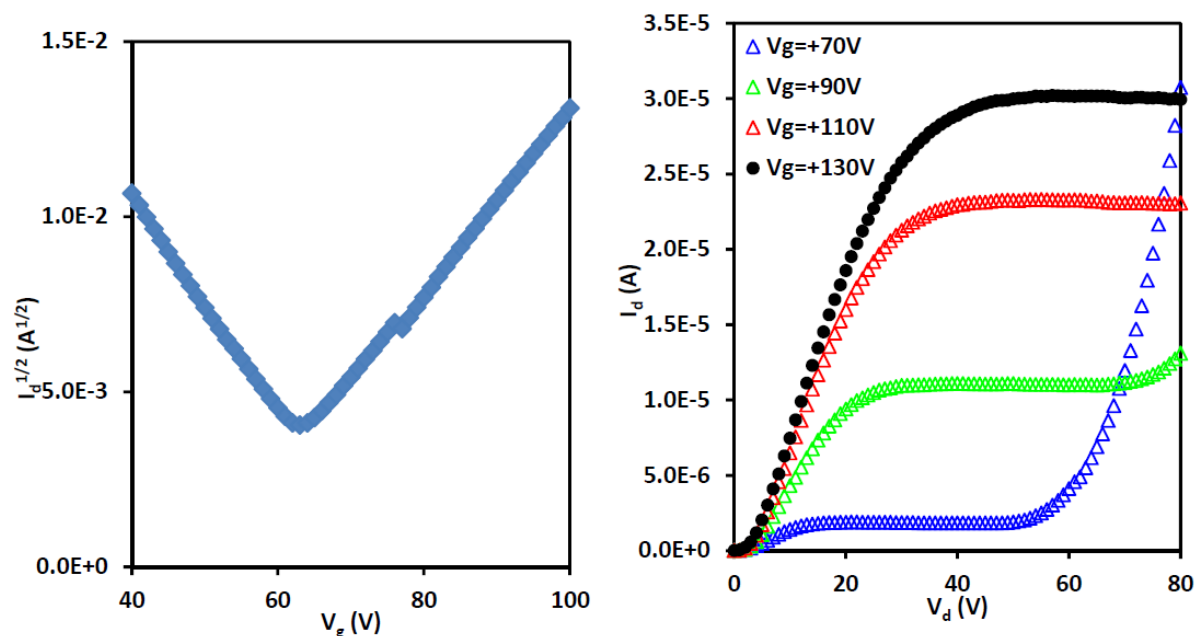


**Figure 5.2.** N-type transfer curve at V<sub>d</sub>=+80V (left) and output curves (right) of spin-coated PCDTPT on normal SiO<sub>2</sub> dielectrics.

As the devices were bias-swept successively in approximately 5 minutes (also called aging) ( $V_g$  from +20V to -60V) to get repeatable transfer curves (**Figure 5.1a**), we noticed the substantial changes in the device characteristics (commonly named “aging effect” or “device instability” by industry). Hole current increased; electron decreased; OFF current decreased and turn on voltage ( $V_{on}$ ) shifted to more positive gate bias (**Figure 5.1a**). Simultaneously, the double-slope behavior became discernible upon aging. As a consequence, the peak mobility as a function of gate voltage increased almost three times after aging, as shown in **Figure 5.1b**. Similar changes were observed in the output curves upon aging (**Figure 5.1c-d**) including the clear disappearance of ambipolarity<sup>157,159</sup> due to the diminution of electron current.

The transfer curve after “aging” is not in steady state, but rather gradually recover back to the first transfer curve when the PFET is not operated, shown in Figure 5.3. As the PFET is in presumably OFF state ( $V_d=V_g=0V$ ), the transfer curve quickly recovers in the first 20 minutes, then gradually recover to the first scan in the course of around four days. The recover can be explained by the neutralization of electron-trapped sites by injected holes, which is discernible from hole current at  $V_g=0V$  after “aging”. This effect on holes in the recovery and the mechanism of the double-slope is investigated further in section 5.5.

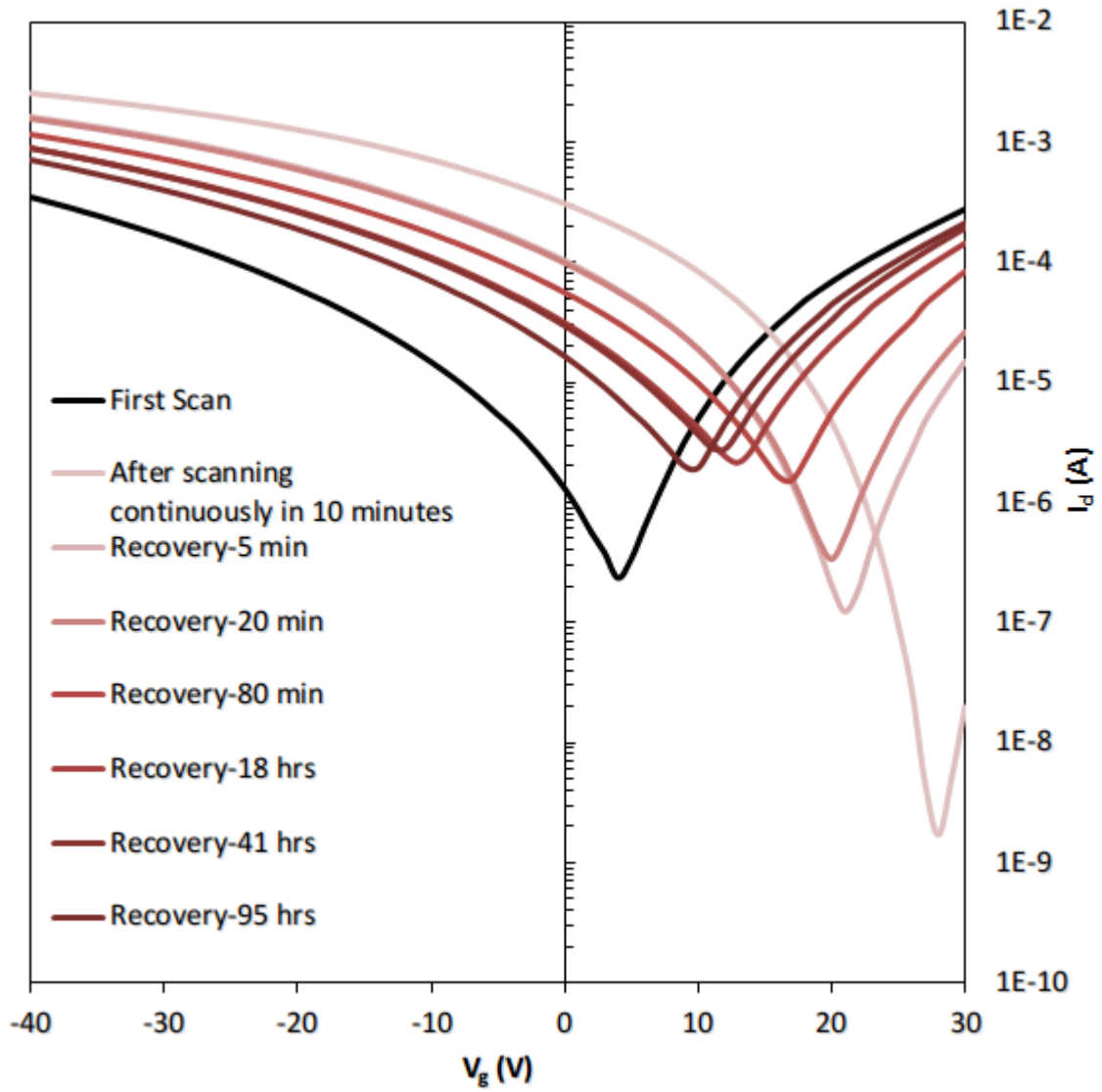
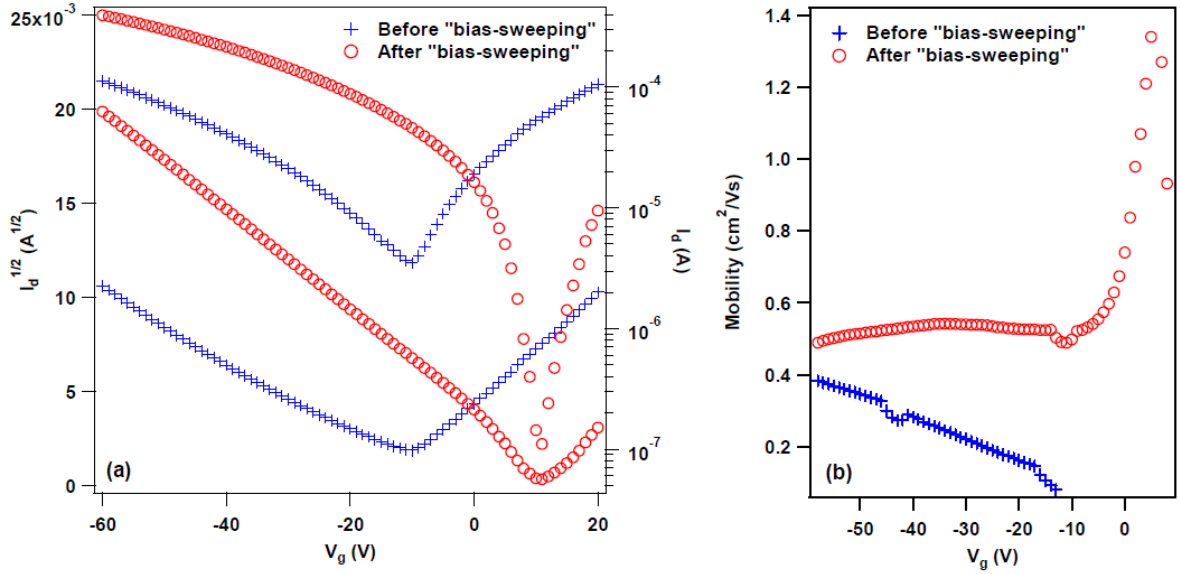


Figure 5.3. Transfer characteristics of the PCDTPT PFET at  $V_d=-80\text{V}$  before, after bias-sweeping gate voltages from  $30\text{ V}$  to  $-40\text{ V}$  in approximately  $10\text{ minutes}$  (also called aging); and recovery in  $95\text{ hours}$  when the device is set at  $V_d=V_g=0\text{V}$ . After each recovery interval, the transfer curve was quickly obtained in  $5\text{ seconds}$  and the device is set back to  $V_d=V_g=0\text{V}$  until the subsequent scan. Device structure:  $\text{Si/SiO}_2/\text{Au/DTS/PCDTPT}$ .

The bias-sweeping effects were also observed for the spin-coating devices on normal SiO<sub>2</sub>/DTS substrates (**Figure 5.4**), which indicates that the cause is not the nano-grooves on SiO<sub>2</sub> surface.



**Figure 5.4. The effect of continuous bias-sweeping on transfer curves (a) and mobility (b) of spin-coated PCDTPT on normal SiO<sub>2</sub> dielectrics (at  $V_d = -80$ V).**

### 5.3. Electron-Trapping-Induced Electrical Instability and Double-Slope

In order to investigate the mechanism of the electrical instability and the double slope, it is crucial to de-couple the effects of positive and negative gate voltages in bias-sweeping in Figure 5.1. We first scanned the devices at negative gate voltages then positive gate voltages (**Figure 5.5**). The bias-sweeping at very negative bias (hole transport regime) did not change the transfer curves whereas the bias-sweeping at positive bias (ambipolar and electron transport regime)<sup>157,159</sup> significantly changed the transfer curves in the similar manner with “aging effect” presented in Figure 5.1.



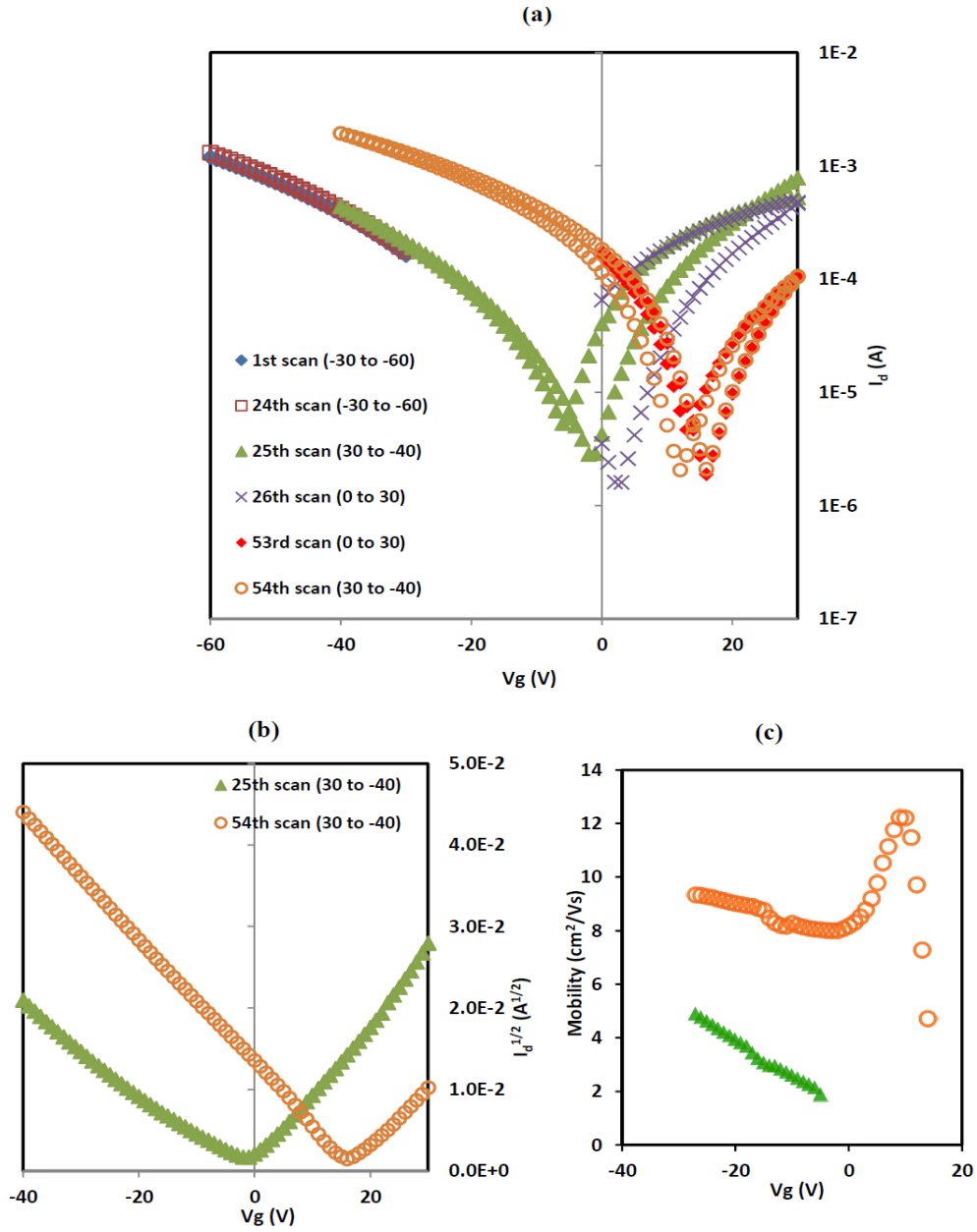


**Figure 5.5. (a) Effect of bias-sweeping at negative and positive  $V_g$  on transfer curves of PCDTPT FETs ( $V_d=-80V$ ); (b) Two transfer curves in (a) plotted in linear scale; (c) mobility extracted from two curves in (b). Device structure: Si/SiO<sub>2</sub>/Au/DTS/PCDTPT.**

Next, we bias-stressed the device at fixed gate voltages of -40 V for 5 minutes at  $V_d=-80V$ ; and the I-V curves were recorded; then we bias-stressed at  $V_g = +30V$  and  $V_d=-80V$  for 5 minutes. **Figure 5.6a** presents the effect of bias-stress on the transfer characteristics at opposite gate polarities. Bias-stressing at +30 V caused the most change in the transfer curve, whereas negative gate bias only slightly lowered the OFF current. The current decay as functions of bias-stress time in PCDTPT FETs is shown in **Figure 5.6b**.

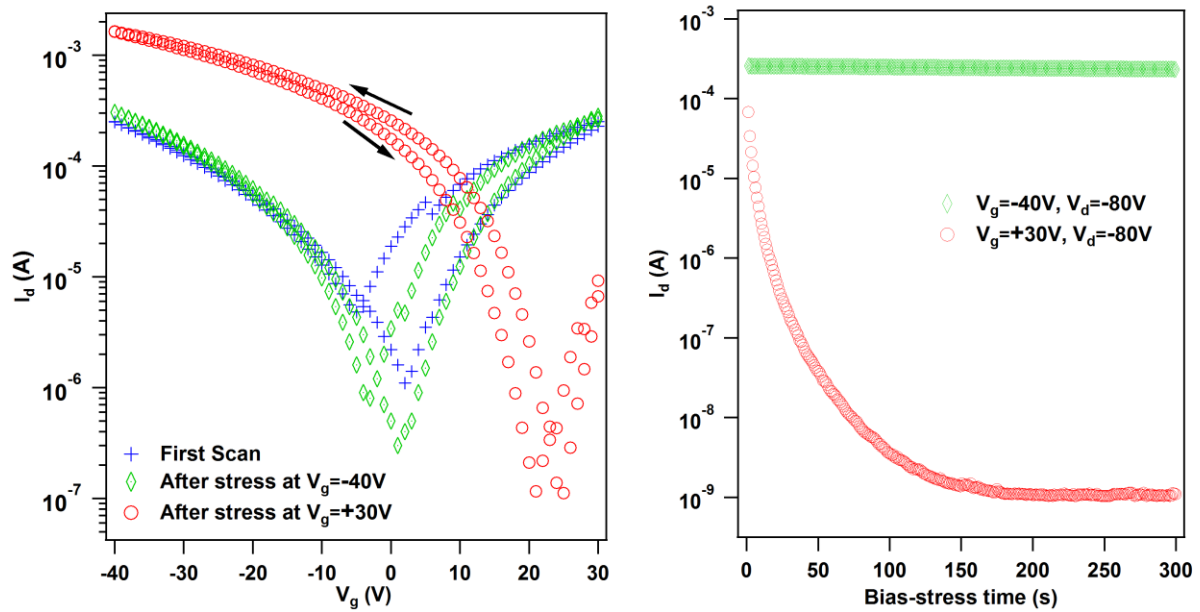


**Figure 5.6. (a) The transfer characteristics of the PCDTPT PFET at  $V_d=-80V$  before stressing and after stressing at fixed  $V_d=-80V$  and  $V_g=-40V$  or  $+30V$ ; and (b) Drain current decay during bias-stress in hole accumulation ( $V_g=-40V$ ) and electron accumulation ( $V_g=+30V$ ) regime. The arrow indicate the forward current and backward current of bias-sweeping. Device structure: Si/SiO<sub>2</sub>/Au/DTS/PCDTPT.**

As the device was bias-stressed in hole accumulation regime ( $V_g=-40V$ ,  $V_d=-80V$ ), hole current negligibly decreased (from 0.26 mA to 0.23 mA) in the course of 5 minutes, which is commonly observed in p-type OFETs.<sup>43</sup> Remarkably, as the device was bias-stressed in

electron accumulation regime ( $V_g=+30V$ ,  $V_d=-80V$ ), electron current promptly plummeted several orders of magnitude after  $\sim 100$  s. This is a remarkable observation to prove that the trapping of electrons and its consequences may be the main causes of the device instability due to bias-sweeping or bias-stressing in electron accumulation regimes.

Electron trapping that leads to the formation of the negatively charge  $-\text{SiO}^-$  in OFETs employing  $\text{SiO}_2$  as dielectrics has been reported in the past ten years.<sup>30,98,99</sup> In n-type OFET study, it was found that silanol groups ( $-\text{SiOH}$ ) on  $\text{SiO}_2$  surface can trap electron and turn to  $-\text{SiO}^-$ , which was proved by Attenuated total reflection Fourier Transform Infrared (ATR-FTIR) spectroscopy.<sup>98</sup> Electrochemical reactions of water, oxygen, silanol and injected electrons leading to the increase density of  $-\text{SiO}^-$  charge were demonstrated in carbon-nanotube FETs.<sup>160</sup> This mechanism has also been hypothesized as the trapping mechanism for n-type OFETs.<sup>30,99</sup> The fact that the substrates of n-type OFETs become more negatively-charged after stressing at positive gate bias has been proved by Scanning Kelvin Probe Microscopy.<sup>44,161</sup> The electrochemical reactions involve in the electron trapping and the formation of  $-\text{SiO}^-$  can be found in Phan et al.<sup>162</sup>

In PCDTPT FETs, the formation of  $-\text{SiO}^-$  upon electron trapping can be applied to explain the rapid decay of electron current (**Figure 5.6b**) and substantial changes in device characteristics. Firstly, the presence of  $-\text{SiO}^-$  at the contacts results in the increase of electron injection barrier resulting in the prompt reduction of electron current. Secondly,  $-\text{SiO}^-$  increases the effective gate voltage for hole accumulation while reduces the effective gate voltage for electron accumulation.<sup>37,44</sup> As a result, both threshold voltages of hole and electron positively shift, which causes the positive shift of turn-on voltage in the transfer curves. The suppression of electron current and enhancement of hole current then

concomitantly happen for the same reasons. Apart from the anomalous increase of the peak mobility (**Figure 5.1b**), the overall hole mobility slightly increases after electron trapping and  $-\text{SiO}^-$  formation, which may be due to the attractive force of hole and  $-\text{SiO}^-$  charges. This is opposite to the observation in p-type bias-stress in which hole mobility decreases due to repulsive force of hole and proton.<sup>30,43</sup> The positive shift of threshold voltage can also be responsible for the negative shift of the drain saturation voltage ( $V_{\text{d}}^{\text{sat}}$ ). Therefore, saturation become less obvious for the FET after aging, especially at high  $V_{\text{g}}$  (Figure 5.1d).

#### ***5.4. Reduction of Electron Trapping at Low Temperature***

The source of electron traps is thought to be the interplay of silanol groups of  $\text{SiO}_2$  dielectrics and a trace amount of water and oxygen trapped on  $\text{SiO}_2$  surface. Due to the extreme complexity of electrochemical reactions of electrons, silanol, water and oxygen in a solid-state device, it may not be possible to directly prove this hypothesis. Alternatively, we can indirectly prove by intentionally mitigating the effect of water and  $\text{SiO}_2$  dielectrics. To prove the role of water in trapping electrons in PCDTPT FETs, we performed bias-stress in electron conduction regime at low temperatures at which water is frozen. As mentioned in chapter 4, in OFETs, a trace amount of confined water, so-called supercooled water are unable to form crystalline structure; thus remaining fluid well below 273 K. Below 200 K, water solidifies and insignificantly affects the charge transport and charge trapping of OFETs.<sup>144,163</sup> The trace amount of water can be trapped in the film, especially at the interface of the  $\text{SiO}_2$  and the polymer and cannot be pumped out completely under vacuum. In a report by Blom and coworkers,<sup>145</sup> the authors found a common electron trap caused by a water and oxygen complex in organic single-carrier diodes and light-emitting diodes even when these devices were fabricated in the  $\text{N}_2$  glovebox and tested in vacuum.

**Figure 5.7a** demonstrates the decay of electron current as a function of bias-stress time at temperatures ranging from 300 K to 100 K. At all temperatures, the devices were stressed at constant  $V_d=-80\text{V}$  and  $V_g=+30\text{V}$  in 300 s. At 300 K and 240 K, the current significantly dropped after 300 s. The current decay was less pronounced at 220 K and became insignificant at all temperature below 180 K. **Figure 5.7b** shows the transfer curves before and after bias-stress at different selected temperatures. At 160 K, as electron trapping is eliminated due to the freezing of supercooled water, transfer curves before and after bias-stressing are indiscernible. **Figure 5.7c** demonstrates the difference in the variation of the current decay ratio after 300 s (defined as  $(I_{d, \text{initial}} - I_{d, \text{at } 300\text{s}})/I_{d, \text{initial}}$ ) and the variation of mobility, as temperature increases from 100 K to 300 K. At around 200 K, current decay sharply increases from 0.25 at 180 K to 0.99 at 240 K while mobility slightly increases from  $0.55 \text{ cm}^2/\text{Vs}$  to  $0.59 \text{ cm}^2/\text{Vs}$ , respectively. The slow change of mobilities around 200 K is consistent with a previous paper of PCDTPT FETs.<sup>117</sup> Those phenomena happen at around 200 K because it is the condensation temperature of supercooled water trapped in the devices. Below 180 K, the mobility continues to decrease (hopping transport) while the current decay ratio remains relatively constant. Those indicate that the significant reduction of bias-stress effect below 200 K is due to the freezing of supercooled water but not the reduction in mobility.

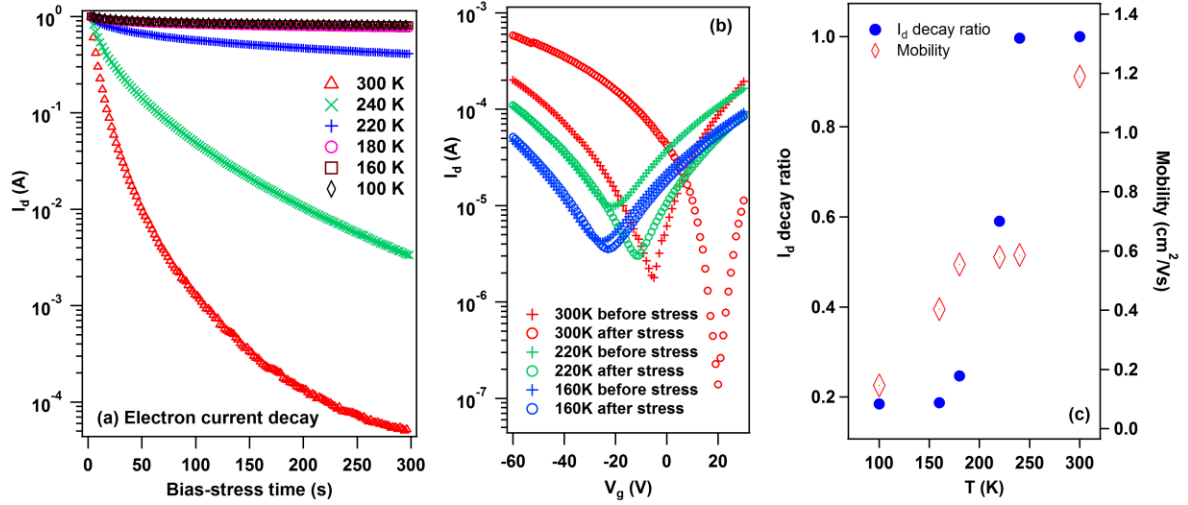


**Figure 5.7. (a) Electron current decay from bias-stressing of PCDTPT FETs in electron accumulation regime ( $V_d=-80\text{V}$ ,  $V_g=+30\text{V}$ ) at different temperatures. Inset: current decay ratio ( $(I_{d, \text{initial}} - I_{d, \text{at 300s}})/I_{d, \text{initial}}$ ) as a function of temperatures. (b) Transfer curves before and after bias-stress (in (a)) at different selected temperatures. Device structure: Si/SiO<sub>2</sub>/Au/DTS/PCDTPT, spin-coating on nano-grooved substrates.**

### 5.5. Mechanism of the Double Slope

The mechanism for the occurrence of the double-slope in the transfer curve after bias-sweeping or bias-stressing in electron accumulation regime is also investigated. The double-slope has also not been interpreted in the literature even though some suggestions have been made, such as the effect of contact resistance, the disorder at the interface, the influence of the subthreshold regime and the non-saturated at high  $V_g$ .<sup>64</sup> In our case, **Figures 5.1 and 5.6** clearly show that the double-slope happens upon bias-stressing PCDTPT FETs in the electron conduction regime. However, it is unclear how the electron trapping and followed by the formation of  $-\text{SiO}^-$  result in the double-slope.

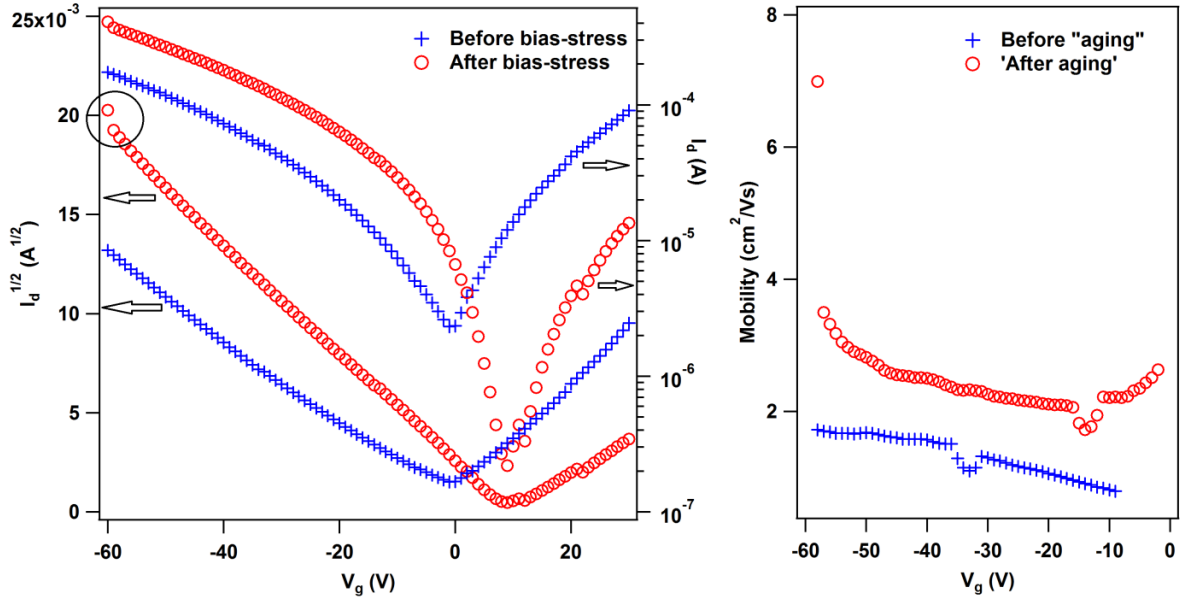


**Figure 5.8. (a) The transfer characteristics of the PCDTPT PFET at  $V_d=-80V$  before and after stressing at  $V_d=-80V$  and  $V_g=30V$ . The blue curve (before stressing) was scanned from  $V_g=30V$  to  $V_g=-60V$ . The red curve (after stressing) was scanned from  $V_g=-60V$  to  $V_g=30V$ . (b) the gate-dependence saturation mobility extracted from I-V curves in (a). Device structure: Si/SiO<sub>2</sub>/Au/DTS/PCDTPT.**

We hypothesize that the change of  $-\text{SiO}^-$  density during the course of one scan deviates the transfer curve from an ideal transfer curve and results in the double-slope. After bias-stressing the device in the electron conduction regime, the transfer curves in **Figure 5.1** were obtained by sweeping  $V_g$  from positive to negative. During this bias-sweeping,  $-\text{SiO}^-$  density reduces due to the neutralization with protons which are produced by electrochemical reactions of trapped water and holes.<sup>30,96</sup> These reactions have been postulated to explain the bias-stress of hole conduction in p-type OFETs using SiO<sub>2</sub> as dielectrics.<sup>30,96,99</sup> To strengthen this hypothesis, the device was scanned from negative to positive gate voltages right after being bias-stressed in electron accumulation regime (**Figure**

**5.8).** The hole current at the initial gate bias,  $V_g = -60V$ , was anomalously higher than the general trend of the transfer curve; possibly because the  $-SiO^-$  density was at its maximum. This observation supports our hypothesis that the formation of  $-SiO^-$  upon electron trapping and the change in  $-SiO^-$  density during one scan results in the double-slope in the transfer curve.

In order to further investigate this hypothesis, hole current dynamics after aging (stress at electron transport regime) under either hole or electron bias stress is measured. These measurements are only possible with the home-built coding program presented in section 2.4. The results are presented in **Figure 5.9**. In the first 200s, constant  $V_g = -40V$  and  $V_d = -80V$  were applied and hole current were measured. Then gate bias was switched to  $+30V$  to stress the device in 300s. Electron current dramatically dropped during the stressing time, consistent with previous report. After stressing the device in 300s at  $V_g = +30V$ , hole current was measured with a 0.5 second pulse bias in every 10 seconds. In between the pulse bias for hole current measurements, the device was stressed at either  $V_g = +30V$  or  $V_g = -40V$ . Firstly, hole current increased more than five times immediately after bias stress, due to the formation of  $SiO^-$  as we explained before. Then, hole current increased when the device was stressed in electron transport regime ( $V_g = +30V$ ), due to the further increase of  $SiO^-$  that induced more holes. On the other hand, as the device was stressed at hole transport regime, hole current decreased to the initial value at  $t = 0s$ . It implies that injected holes neutralize  $SiO^-$  and therefore diminish the effect of  $SiO^-$  in increasing hole current.



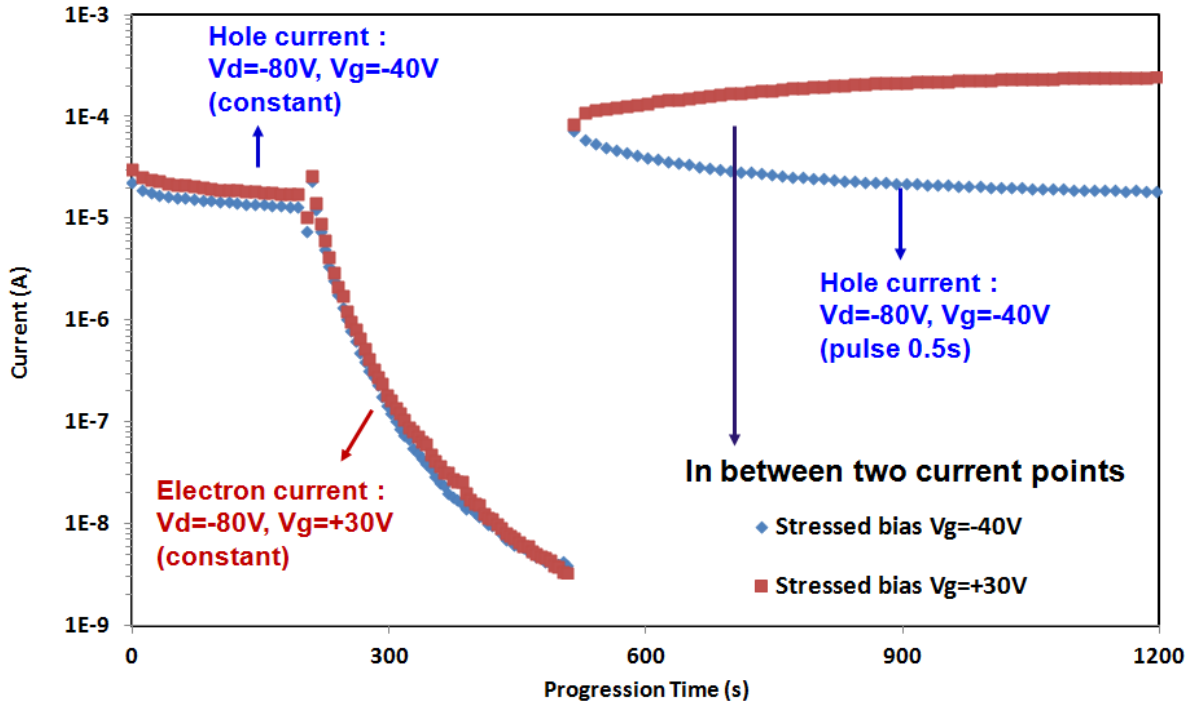
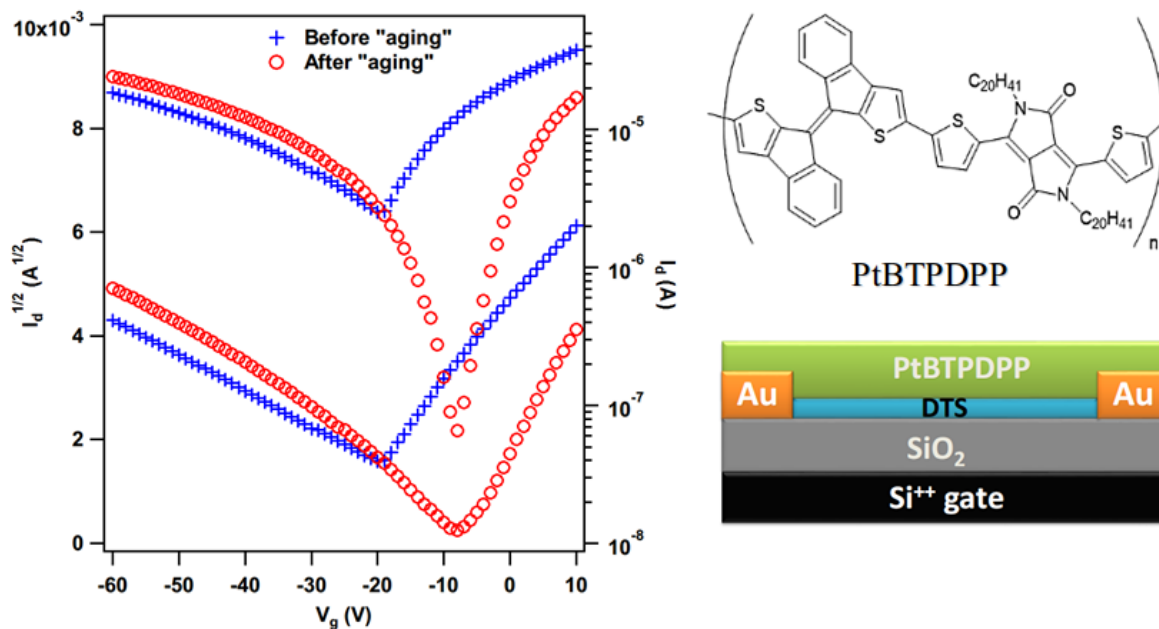


**Figure 5.9. Hole/electron current dynamics of PCDTPT PFET: hole current at  $V_d=-80\text{V}$  and  $V_g=-40\text{V}$  for  $t=0-200\text{s}$ , followed by electron current at  $V_d=-80\text{V}$  and  $V_g=+30\text{V}$  for  $t=200-500\text{s}$ ; and finally hole current measured with a 0.5 second pulse bias  $V_d=-80\text{V}$  and  $V_g=-40\text{V}$  every 10 seconds. In between hole current measurements (10s), the device was stressed at either in electron accumulation regime ( $V_d=-80\text{V}$  and  $V_g=+30\text{V}$ ) or hole accumulation regime ( $V_d=-80\text{V}$  and  $V_g=-40\text{V}$ ). Device structure: Si/SiO<sub>2</sub>/Au/DTS/PCDTPT.**

### ***5.6. Generalization of Electrical Instability and Double-slope***

In addition to PCDTPT, the electrical instability and double-slope occurrence in other low band-gap polymers have been observed. Our collaborators, Michael Ford, showed that the electrical instability and double-slope can be found in the copolymers of CDT and three different acceptor units.<sup>164–166</sup> He also showed these behavior for another class of low band

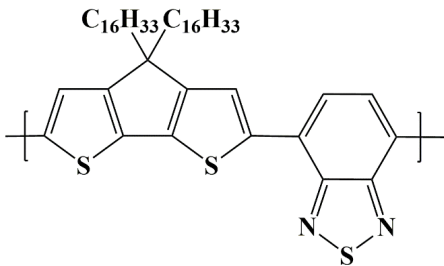
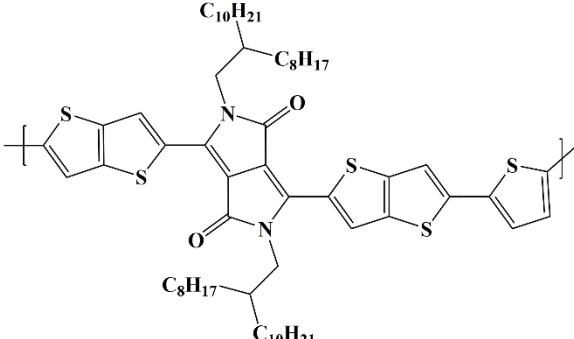
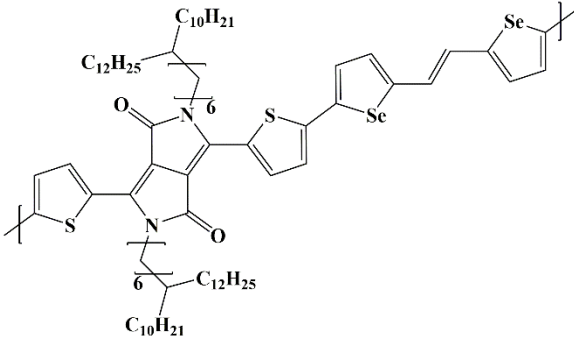
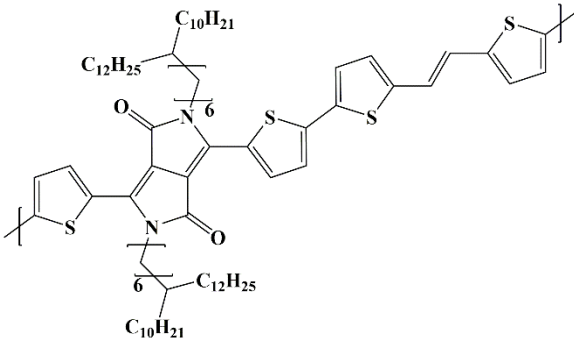
gap D-A polymer based on DPP acceptor unit.<sup>164–166</sup> In **Figure 5.10**, the electrical instability and double-slope are demonstrated for the recently new class of polymer developed by Wudl and coworkers.<sup>167</sup>

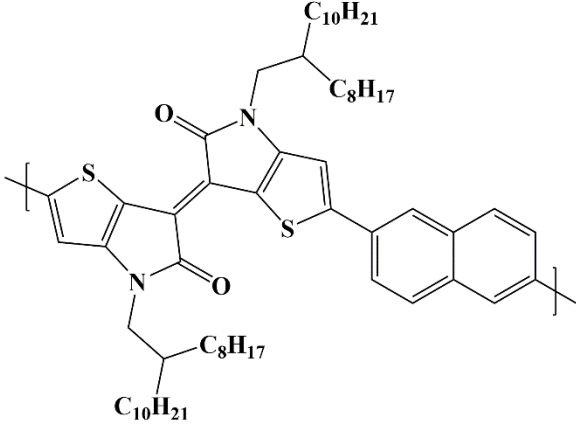
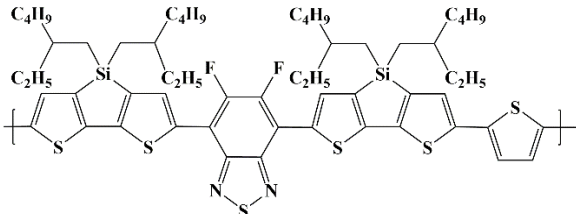
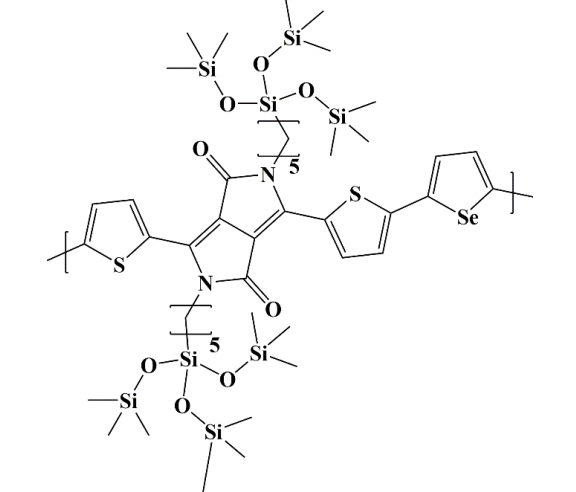
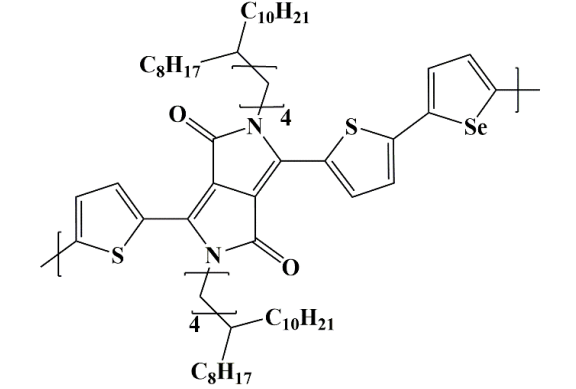


**Figure 5.10.** The transfer characteristics of the PtBTPDPP PFET at  $V_d=-80V$  before and after stressing at  $V_d=-80V$  and  $V_g=30V$ . The blue curve (before stressing) was scanned from  $V_g=30V$  to  $V_g=-60V$ .

The double slope can also be found in a number of papers in the literatures. **Table 5.1** summarize some of the low band gap D-A polymers that showed double-slope in PFET transfer curves. In a total agreement with the finding in this thesis that electron trapping at SiO<sub>2</sub> interface is the cause of the double-slope, all the PFETs that show double-slope are based on SiO<sub>2</sub> dielectrics. In addition, the use of non-SiO<sub>2</sub> dielectric shows no double-slope but lower mobility in compared to SiO<sub>2</sub> dielectric, for a few polymer system.<sup>168,169</sup>

**Table 5.1. Double-slope of recent high-mobility OFETs fabricated from low band gap D-A polymers**

Polymer Structure	Mobility (cm <sup>2</sup> V <sup>-1</sup> s <sup>-1</sup> )	Device Structure <sup>a</sup> / Dielectric <sup>b</sup>	Bandgap/ Double Slope?
	18.5	BGBC DTS- treated SiO <sub>2</sub>	1.3 eV Yes <sup>155</sup>
	2.6	BGBC HMDS- treated SiO <sub>2</sub> <sup>25</sup>	1.3 eV No <sup>67</sup>
	10.5	BGBC DTS- treated SiO <sub>2</sub>	1.30 eV Yes <sup>36</sup>
	1.4	TGBC PMMA	1.30 eV No <sup>168</sup>
	9.8	BGTC OTS- treated SiO <sub>2</sub>	1.18 eV Yes <sup>169</sup>
	6.9	BGTC Cytop	1.18 eV No <sup>169</sup>
	8.5	BGTC OTS- treated SiO <sub>2</sub>	1.18 eV Yes <sup>169</sup>
	4.8	BGTC Cytop	1.18 eV No <sup>169</sup>

	12	BGTC P(VDF- TrFE)	1.36 eV No <sup>154</sup>
	9.1	TGBC P(VDF- TrFE)	1.38 eV No <sup>170</sup>
	8.8	BGTC OTS- treated SiO <sub>2</sub>	1.24 eV Yes <sup>171</sup>
	8.3	BGTC OTS- treated SiO <sub>2</sub>	1.28 eV Yes <sup>172</sup>

	7.1	BGTC OTS- treated SiO <sub>2</sub>	1.20 eV Yes <sup>173</sup>
	BT: 0.02 DPP: 1.8	BGTC ODMS- treated SiO <sub>2</sub>	BT: 1.7 eV DPP: 1.3 eV  BT: No DPP: Yes <sup>174</sup>

<sup>a</sup>: BGBC = bottom gate, bottom contact; BGTC = bottom gate, top contact; TGTC = top gate, top contact; TGBC = top gate, bottom contact. <sup>b</sup>: DTS = decyltrichlorosilane; OTS = octadecyltrichlorosilane or octamethoxytrichlorosilane; HMDS = hexamethyldisilazane; ODMS = *n*-octadecyltrimethoxysilane; P(V<sub>D</sub>F-TrFE) = poly[(vinylidene fluoride-co-trifluoroethylene)]; PMMA = poly(methyl methacrylate); Cytop = proprietary fluorinated polymers

## 5.7. Conclusion

In conclusion, the causes of electrical instability (aging) and double-slope of p-type PFETs fabricated from low band-gap D-A copolymers are elucidated. Electron trapping and subsequently the formation of  $-\text{SiO}^-$  charges are the principle origins for considerable changes in the device characteristics upon bias-sweeping, including the occurrence of the double-slope behavior. The findings provide important guidelines for molecular design and

device engineering of toward high performance and practical OFETs. For the former one, the strategy of using D-A copolymer motif to increase FET hole mobility should be manipulated to minimize ambipolarity. For instance, the molecular structure should not stabilize electrons too well; or should have a shallower LUMO which leads to insufficient electron injection in OFETs using Au contacts. For device engineers, the replacement of SiO<sub>2</sub> dielectric by electron-trap-free polymer dielectrics must be genuinely considered. Simply using self-assemble monolayers such as DTS is not sufficient to protect the SiO<sub>2</sub> surface to prevent the device instability. In addition, work-functions of source/drain contacts can be modified to suppress electron injection. In the following chapter, it is demonstrated that those guidelines have been successfully applied at UCSB.

## **6. Suppressing Electrical Instability and Double-Slope by Molecular Design and Device Engineering**

### ***6.1. Introduction***

From the comprehensive study in chapter 5, two methods can be readily realized to suppress the electrical instability and double-slope. First, a hydroxyl-free, hydrophobic dielectric, and free of electron traps can be used. As shown in Table 5.1, no double-slope was observed when P(VDF-TrFE)<sup>154</sup> and CYTOP<sup>169</sup> were used as dielectrics in the literature. In section 6.2, a polymer dielectric is used to suppress the electrical instability and double-slope of PCDPTP FETs. The second method is to design a polymer with LUMO further away from the work function of Au contacts. In section 6.3, a CDT-based material with low-lying LUMO is designed and investigated. Another method, discovered by our collaborator, Michael Ford at Professor Bazan's group,<sup>164</sup> involves the use of electron acceptors to accept electrons from the polymers so that the injected electrons are not trapped at SiO<sub>2</sub> interface. Working mechanism of this method is presented in section 6.4.

### ***6.2. Utilizing non SiO<sub>2</sub> dielectric materials***

#### **6.2.1. Suppressing Electron Trapping with BCB dielectric**

In order to suppress the instability and double-slope of PCDTPT FETs, a bilayer dielectric, Si/SiO<sub>2</sub>/BCB is used in BGBC FETs. In this configuration, the polymer is deposited on top of BCB. BCB (a polymer of divinyl-tetramethylsiloxane-bis(benzocyclobutene) derivative) is a crosslinked hydroxyl-free polymer dielectric that repels water absorption and hence reduce electron traps in OFETs.<sup>98</sup> The device was

prepared by spin-coating PCDTPT polymer solution on SiO<sub>2</sub>/BCB substrates, followed by Au evaporation for top contacts. For comparison, a controlled device was also fabricated and tested using Si/SiO<sub>2</sub> substrates with same DTS treatment as bottom-contact devices. This measurement also helps to confirm the role of SiO<sub>2</sub> surface in trapping electrons.

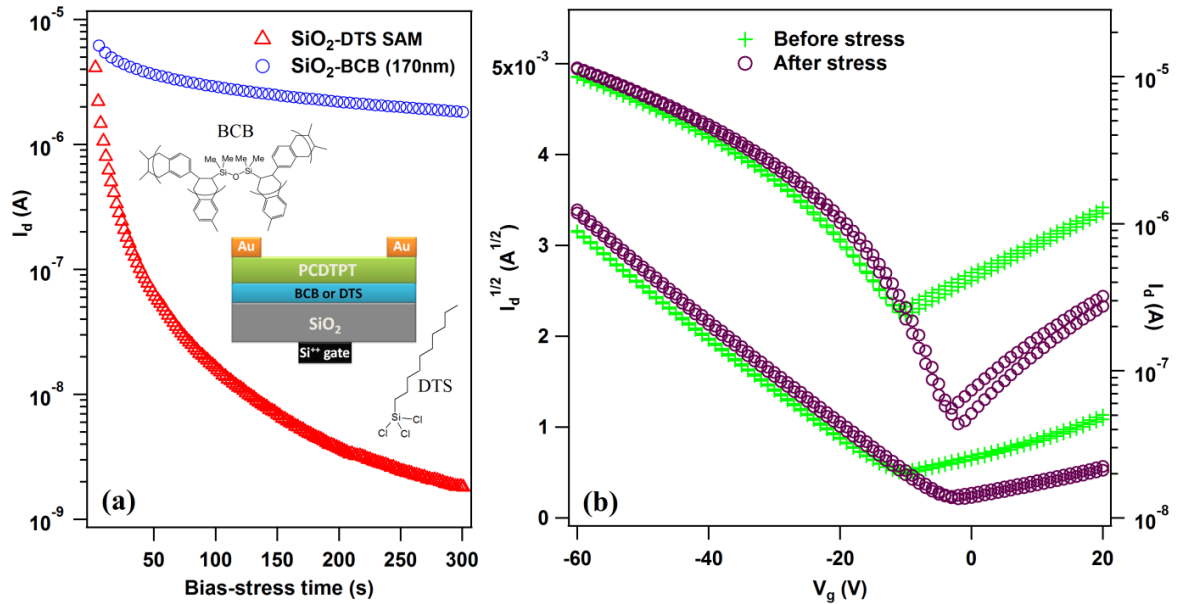


**Figure 6.1. (a) Drain current decay from bias-stressing of top-contact PCDTPT FETs in electron accumulation regime at different dielectrics ( $V_d=-80V$ ,  $V_g=+30V$  for SiO<sub>2</sub>-DTS SAM and  $V_g=60V$  for SiO<sub>2</sub>-BCB to obtain comparable initial current); and (b) The transfer characteristics of the PCDTPT PFET at  $V_d=-80V$  before stressing and after bias-stressing. Device structure: Si/SiO<sub>2</sub>/DTS SAM or BCB/PCDTPT/Au.**

**Figure 6.1a** shows the current decay of the FETs prepared on the two substrates. As expected, top-contact devices using SiO<sub>2</sub> substrates exhibited almost four orders of magnitude decrease of electron current under bias-stress, similar to bottom-contacts ones (**Figure 5.1**). On the other hand, the use of BCB dielectrics immensely lowered the electron current decay under bias-stress. The transfer curves of BCB device before and after being



stressed were presented in **Figure 6.1b**. In complete contrast with the devices prepared on SiO<sub>2</sub> substrates (**Figure 6.2**), insignificant changes in hole current upon bias-stressing were observed. Most importantly, the double-slope behavior did not occur. Recently, a high-performance D-A copolymer was also reported with another hydroxyl-free dielectric, poly(vinylidene fluoride-trifluoroethylene) (P(VDF-TrFE)), without exhibiting double-slope behavior.<sup>154</sup> The slight decrease of electron current in BCB devices might be attributed to the inevitable electron trapping by a trace amount of water and oxygen either at the interface or in the polymer itself.

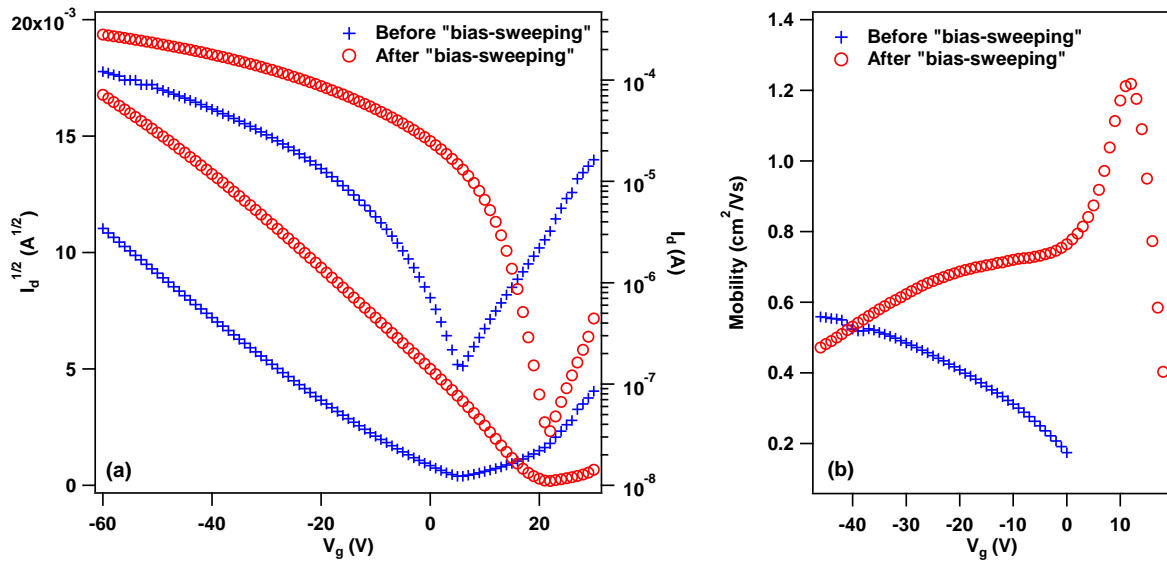


**Figure 6.2. The effect of continuous bias-sweeping on transfer curves (a) and mobility (b) of spin-coated top-contact PCDTPT on normal SiO<sub>2</sub> dielectrics with DTS treatment (at V<sub>d</sub>=-80V).**

### 6.2.2. Conclusion & Future Work

As we learn from the intensive bias-stress study in chapter 5, SiO<sub>2</sub> dielectrics is one of the major sources of electron traps. It results in the instability of the PFETs that possess

ambipolarity. In unipolar p-type OFETs, SiO<sub>2</sub> has been shown to trap holes, resulting in the continuous threshold voltage shift under prolonged operation.<sup>93,96,175</sup> Therefore, it is very important to test polymer substrates or polymer dielectrics as alternative platforms to evaluate and optimize OFETs. It is also helpful for OFET commercialization because practical OFETs are desired to be deposited on flexible polymer substrates eventually. BCB has been demonstrated to work well for bottom-gate top-contact spin-coating PCDTPT FETs. The stability of the device is significantly improved with BCB dielectrics. However, the high electron current (Figure 6.1b) reduces ON/OFF ratios; and electrons may get trapped for prolonged operations. In addition, the mobility is low because the polymer chains are not aligned. In future work, the mechanical rubbing method can be used in two ways to improve the mobility of PFETs using polymer dielectrics.<sup>131,176-178</sup> In the first method, top surfaces of semiconducting polymers can be rubbed to align the polymer chains for high-mobility top gate PFETs. In the second one, polymer dielectrics can be rubbed to make nano-grooves, similar to the nano-grooves on SiO<sub>2</sub>, to induce polymer alignment when the polymer semiconductors are deposited on top of nano-grooved polymer dielectrics. Mechanical rubbing has been used in manufacturing liquid crystal display (LCD) for decades.<sup>179</sup>

### ***6.3. New Material Design and Characterization for Suppressing the Electrical instability and Non-ideality while Maintaining High Mobility***

#### **6.3.1. Design Principles for Inhibiting Electron Injection**

Chapter 5 demonstrates that the enabling of electron injection, transport and trapping in the PCDTPT PFETs is the root cause of the electrical instability and double-slope. Naturally, the first design principle to improve this is to block the electron injection by widening the

electron injection barrier between the Au source/drain contacts and the semiconductors. One way to achieve it is to use a material with much shallower LUMO. PCDTBTA (**Figure 6.3**) is a new CDT-based polymer using a weaker acceptor unit, BTA, to raise the LUMO further away from Au work-function to eliminate the electron injection, while keeping D-A motif for high mobility.

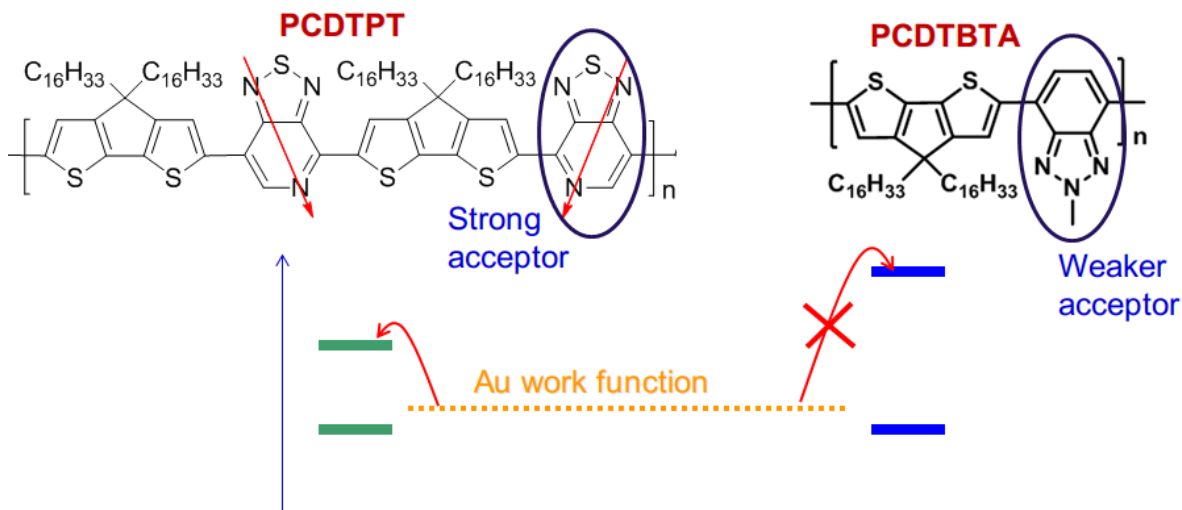


**Figure 6.3. Design principle of PCDTBTA for inhibiting electron injection in OFETs. PCDTBTA was synthesized by Dr. Ming Wang.**

### 6.3.2. Improved Device Stability and Ideality in PCDTBTA FETs

The transfer and output curves of PCDTBTA (molecular weight ~24 KDa, PDI ~2.9) FETs fabricated by blade-coating on nano-grooved substrates are presented in **Figure 6.4**. As we expected, all the devices are unipolar p-type OFETs. Other characteristics are close to ideal for an FET: 1) low hysteresis; 2) low turn-on voltage; and 3) well-defined saturation regime in output curves. The mobilities are shown in **Figure 6.5b**. For both as-prepared and annealed devices, mobility of parallel devices (to the direction of the grooves and the blade movement) is about ten times higher than that of perpendicular devices. This is an indirect

indication of the polymer chain alignment along the grooves. Interestingly, thermal annealing degrades the mobility of PCDTBTA FETs. This is opposite to PCDTPT FETs and other PFET systems reported in the literature.

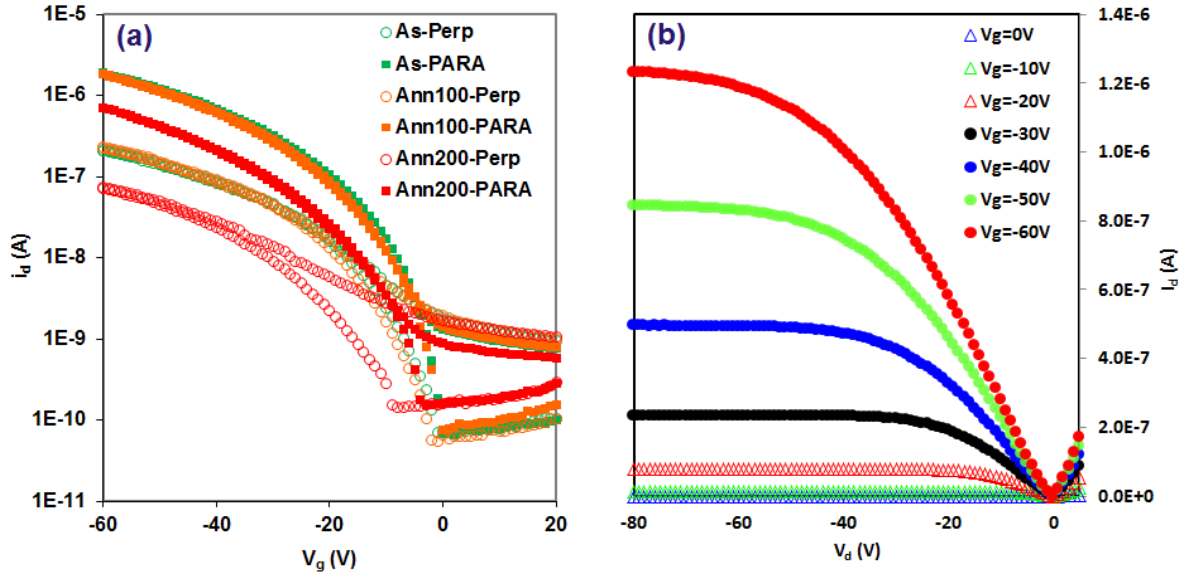


**Figure 6.4. (a) Transfer characteristics of PCDTBTA FETs in saturation regime ( $V_d=-80V$ ) for the polymer alignment parallel (PARA) and perpendicular (Perp) to the grooves at three different conditions: as-prepared (as), annealed at 100 C in 8 minutes (Ann100) and annealing at 200 C in 8 minutes (Ann200); (b) output curves of an as-prepared parallel device.**

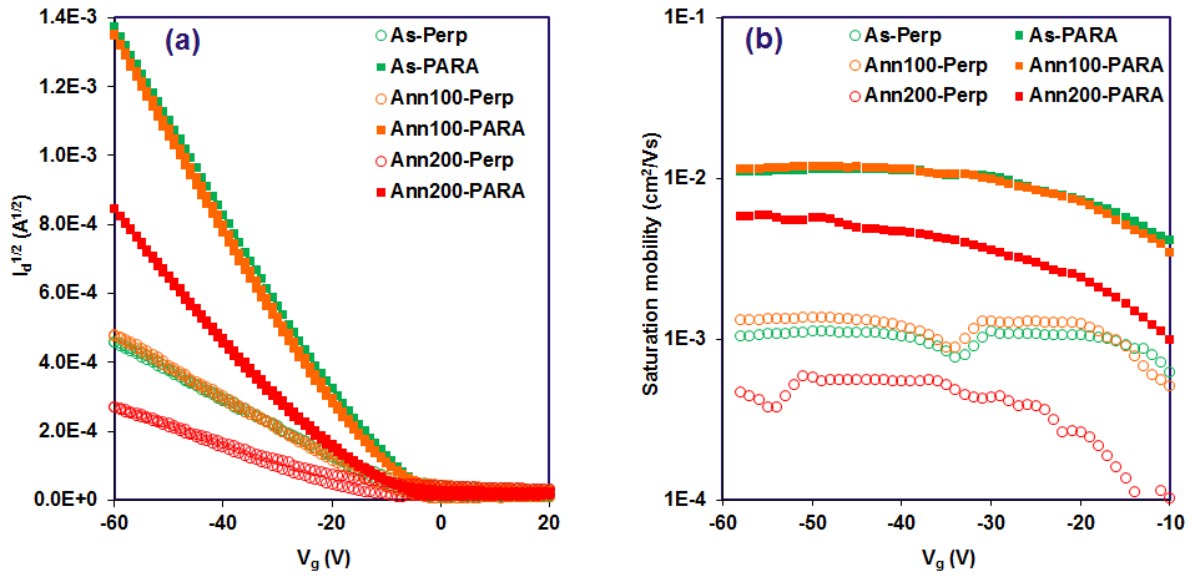


**Figure 6.5. (a) Transfer characteristics of PCDTBTA FETs in saturation regime ( $V_d=-80V$ ) at different conditions (same data as Figure 6.4a but in linear scale to get mobility); (b) Saturation mobilities of PCDTBTA FETs.**

Since the PCDTBTA FETs are unipolar, an “aging” effect study is conducted to compare with PCDTPT. The devices were bias-swept 10 times before being bias-stressed in electron accumulation regime ( $V_g=+30V$ ,  $V_d=-80V$ ) in 5 minutes (same conditions that induce “aging effect” in PCDTPT in chapter 5). The first 10 transfer curves and the transfer curve after being bias-stressed are presented in **Figure 6.6**. As clearly shown, all the transfer curves are almost identical and there is no double-slope after bias-stressing. It indicates that the “aging effect” is negligible in PCDTBTA FETs. This is consistent with our hypothesis that negligible electron injection and trapping in these devices is important to eliminate the electrical instability of and double slope.

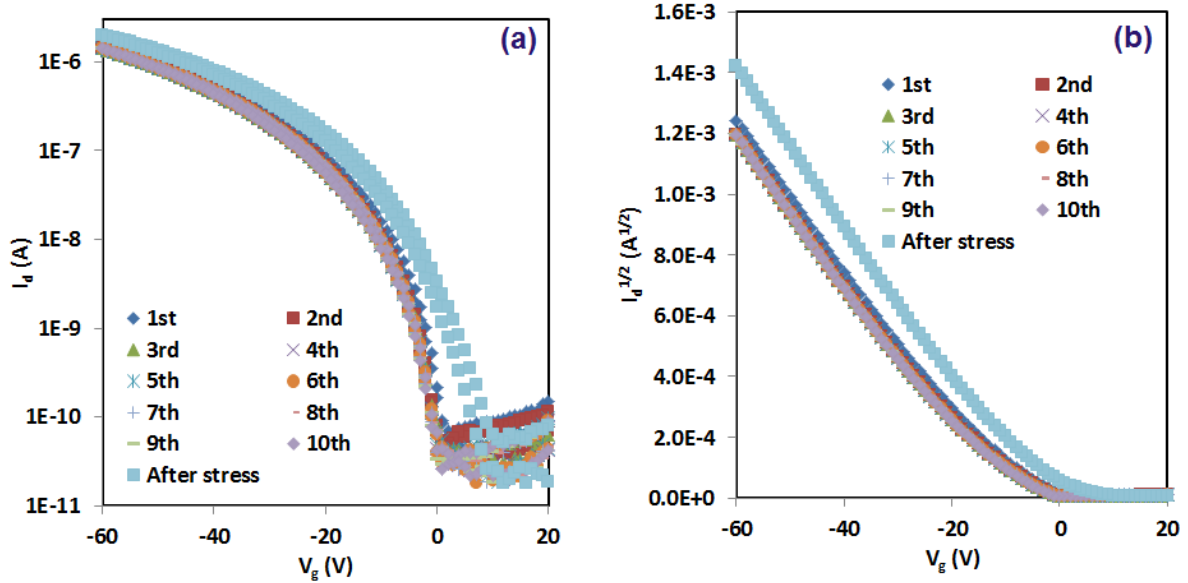


**Figure 6.6. Consecutive transfer curves before and after bias-stressing in (a) log-linear plots and (b) linear-linear plots of PCDTBTA FETs in saturation regime ( $V_d = -80V$ ).**

### 6.3.3. Conclusion & Future Work

The use of a weak acceptor with CDT donor to widen the band gap is successfully demonstrated for suppressing the electrical instability and double slope. However, the mobility is two orders of magnitude lower than PCDTPT FETs, even with polymer alignment on nano-grooved substrates. Perhaps the  $\pi$ - $\pi$  interaction is not strong enough for efficient charge hopping. In the future, the  $\pi$ - $\pi$  stacking will be characterized by GIWAXS, and the temperature-dependent mobility measurements will be conducted to calculate the activation energy. The cause of mobility degradation upon thermal annealing of the PFETs will also be further investigated to establish the structure-processing-property relationship of D-A copolymers for FETs.

## 6.4. Suppressing Electron Transport in Ambipolar PFETs by an Electron Acceptor

### 6.4.1. Suppressing Electron Transport by and Electron Acceptor and Working

#### Hypothesis

In addition to changing polymer structures and using non-SiO<sub>2</sub> dielectrics to suppress the electrical instability and double-slope, a simple addition of an additive in PCDTPT solutions that can suppress electron transport while maintaining high hole mobility of PCDTPT is strongly desired. Michael Ford, in Professor Bazan's group, found that fullerene derivatives can be used to suppress the electrical instability and double-slope while retaining the hole mobility of the PFETs. The phenomena were successfully demonstrated for three electron acceptors (PC<sub>61</sub>BM, bis- PC<sub>61</sub>BM and PC<sub>84</sub>BM) and four low band gap D-A polymers whose FETs exhibit the electrical instability and double-slope.<sup>164</sup> This section presents the mechanistic study of how PC<sub>61</sub>BM and C60 can suppress electron transport while maintaining high hole mobility in PCDTPT FETs. **Figure 6.7** show all the device structures used in this section.

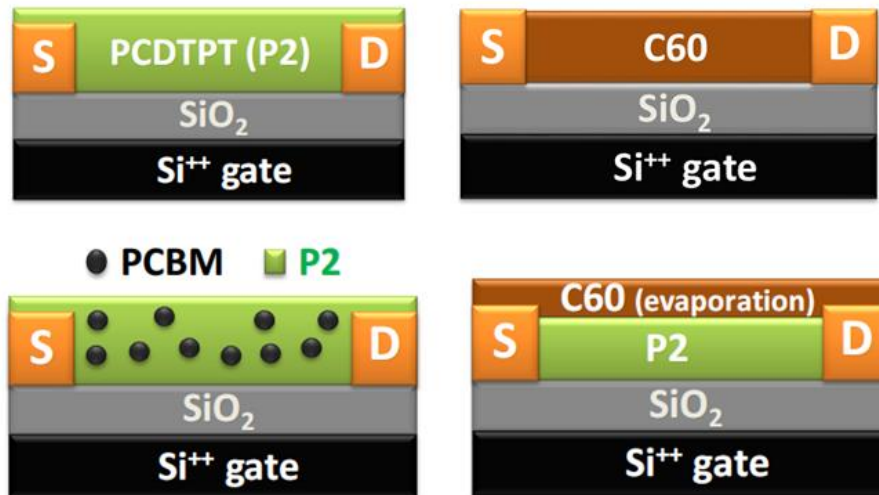


**Figure 6.7.** Device structures used in PCDTPT:PCBM and PCDTPT/C60 study

Two mechanisms are hypothesized to explain the device characteristics of PCDTPT:PCBM (PCBM is used for PC<sub>61</sub>BM from this point) blend FETs (**Figure 6.8**). Firstly, PCBM readily accepts electrons from the polymers to prevent the electron trapping at SiO<sub>2</sub> and the formation of SiO<sup>-</sup> that cause electrical instability and double-slope. This can be explained by two reasons: 1) PCBM have higher electron affinity than PCDTPT and 2) the interaction of the polymers and fullerenes (both carbon-based materials) is stronger than in that of the polymers and SiO<sub>2</sub> surface. Secondly, PCDTPT preferably resides at SiO<sub>2</sub> interface while PCBM stays on top surface. Therefore, hole transport in PCDTPT:PCBM FETs are very similar to that in neat PCDTPT FETs. As mentioned in section 1.4.1, charge transport in OFETs only occurs at the first few nanometers above the dielectric surface.

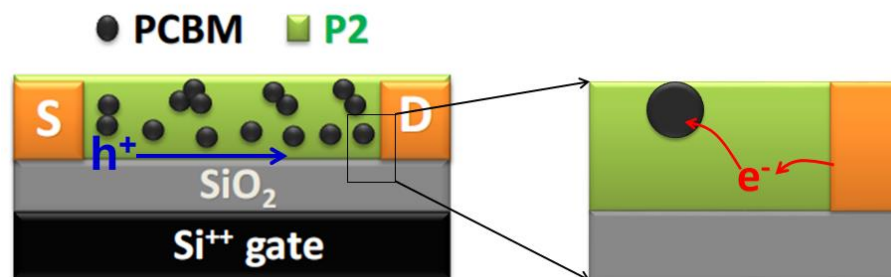


**Figure 6.8. Working hypothesis of the improvement of PCDTPT FETs by the addition of PCBM**

#### 6.4.2. Uninterrupted Hole Transport of PCDTPT in PCDTPT:PCBM and PCDTPT/C60 devices

In order to prove that PCBM preferably stays on the top surface of PCDTPT:PCBM films but still accepts electron from PCDTPT to prevent the electron trapping at SiO<sub>2</sub> surface, the bilayer PCDTPT/C60 is fabricated and tested. In this device, C60 is slowly evaporated on top of a 30nm thick film of PCDTPT therefore it is very likely that there is no



C60 at the SiO<sub>2</sub> interface. As shown in **Figure 6.9**, the addition of C60 on the top surface also suppresses the electron current. The higher OFF current in PCDTPT/C60 devices compared to PCDTPT:PCBM devices is elucidated in section 6.4.3.

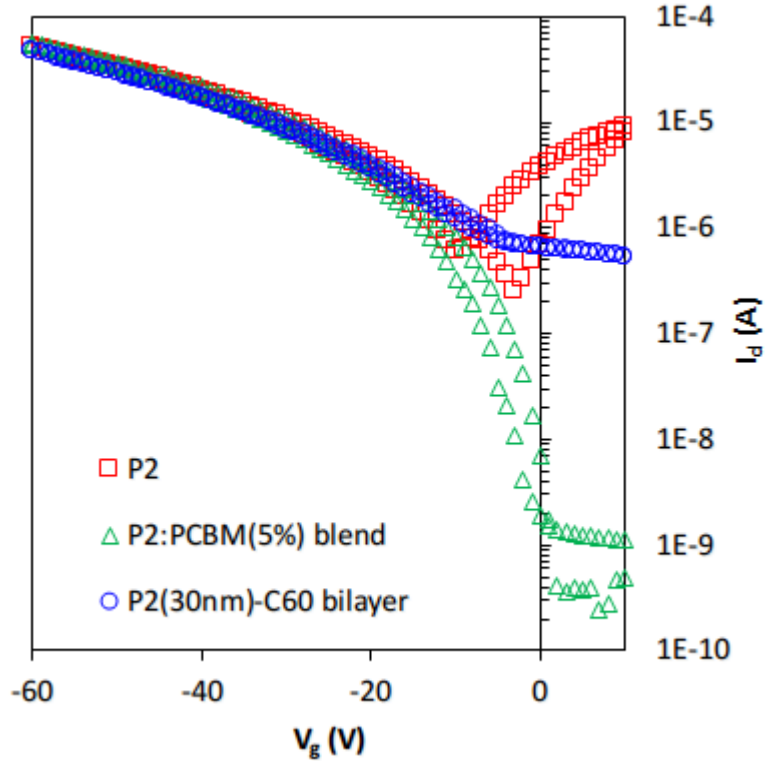


**Figure 6.9.** Transfer curves of PCDTPT (P2), PCDTPT:PCBM blend and PCDTPT/C60 bilayer FETs.

**Figure 6.9** shows that hole transport (at negative  $V_g$ ) of FETs fabricated from the polymer, the polymer:PCBM blend and polymer/C60 bilayer is almost identical. It indicates that hole transport is not interrupted in the presence of either PCBM or C60 in the devices. In order to gain further insight into the uninterrupted hole transport, the activation energy of hole transport in those devices is characterized.

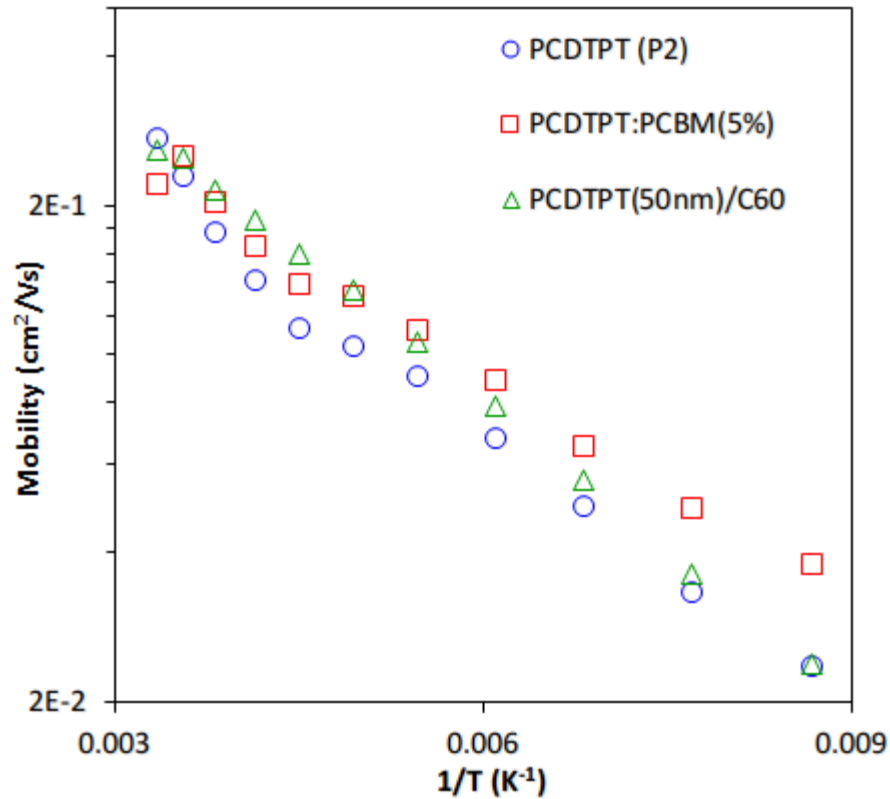


**Figure 6.10. Temperature-dependent mobility of PCDTPT (P2), PCDTPT:PCBM blend and PCDTPT/C60 bilayer FETs.**

**Figure 6.10** presents the temperature-dependent mobility of PCDTPT, PCDTPT:PCBM and PCDTPT/C60 FETs. As expected for thermally activated transport, hole mobility decreases as temperatures decrease for the three devices. The activation energy is extracted using Arrhenius equation. **Figure 6.11** reveals the activation energy of all the devices. The activation energy of FETs fabricated from PCDTPT:PCBM blend at different weight percentages of PCBM and PCDTPT/C60 bilayer with different thicknesses of PCDTPT is very similar, in an agreement with the similar hole current characteristics of the three devices at room temperature. It confirms the hypothesis that hole transport of PCDTPT at the interface of SiO<sub>2</sub> is not interfered by the addition of fullerene derivatives.

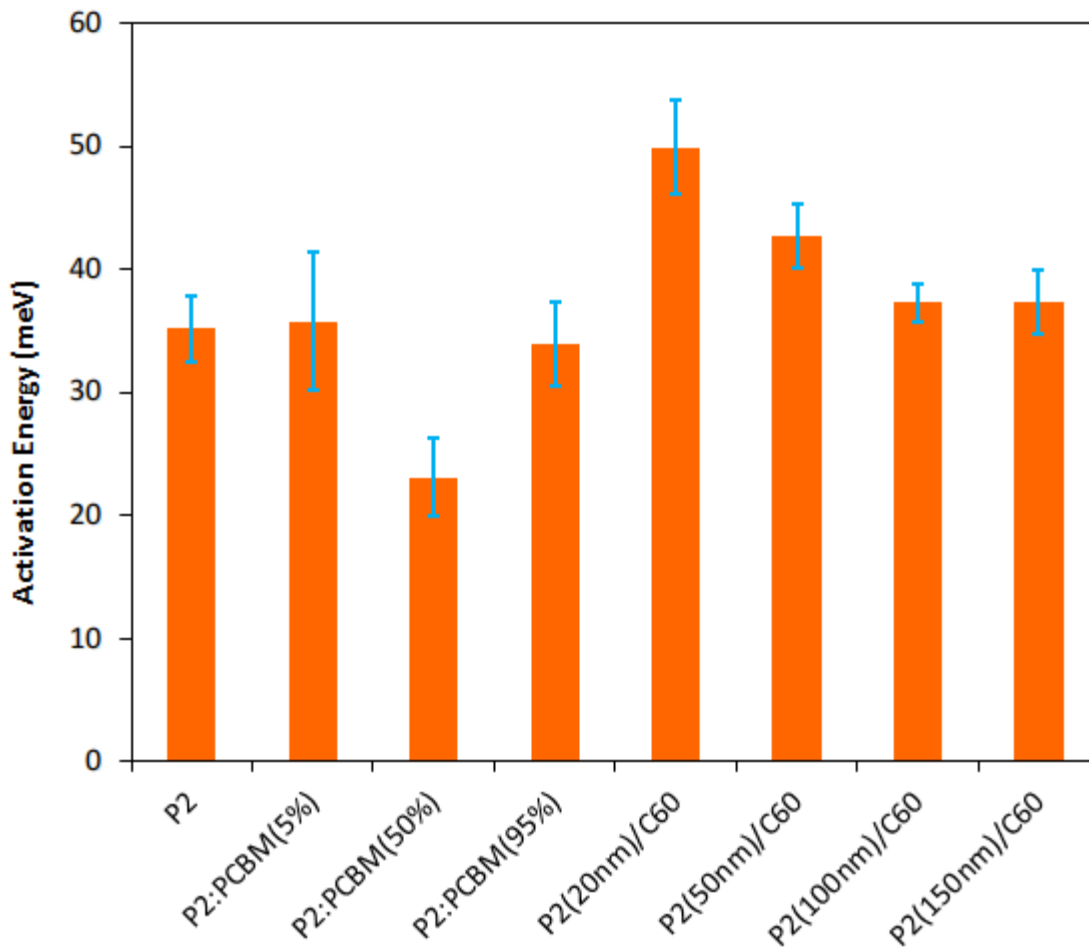


**Figure 6.11. Activation energy of FETs fabricated from PCDTPT:PCBM blend at different weight percentages of PCBM and PCDTPT/C60 bilayer with different thickness of PCDTPT (or P2)**

#### 6.4.3. Electron Transfer from PCDTPT to PCBM and C60

In this section, the electron transfer from the polymers to PCBM or C60 is proved. We use the organic solar cell concept of charge separation at the interface of an electron donor (P2 in this case) and an electron acceptor (C60 or PCBM) upon illumination of visible light.<sup>180–184</sup> The LUMO-LUMO offset of the donor and the acceptor drive charge separation

at the interface of the donor and the acceptor. It leads to an increase in carrier density and hence the device current.

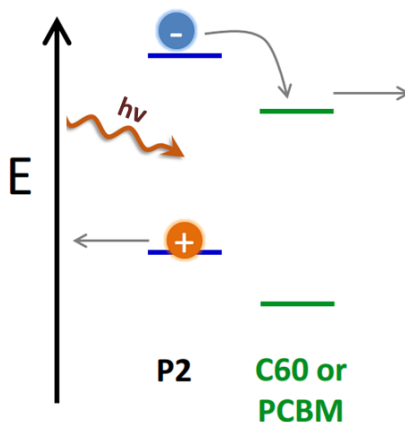


**Figure 6.12. Schematic of charge separation at the interface of an electron donor (P2 in this case) and an electron acceptor (C60 or PCBM) upon illumination of visible light**

In order to prove the electron transfer from PCDTPT to PCBM and C60, the hole and electron current are measured as the function of time with or without illumination by white light. Due to the low intensity of the camera light used in this study, the photogenerated current in the order of 100 nA. Therefore, it is important to control a low level of hole and electron current in the dark so that the increase of photogenerated current can be clearly observed. A transfer curve at low  $V_d$  is presented in **Figure 6.13** to show the well-defined and low OFF current ( $\sim 10$  pA) as well as low ON current ( $\sim 100$  nA). For time-dependent current measurements with light ON/OFF, electron current is measured at  $V_d=-2$  V and  $V_g=+10$  V; and hole current is measured at  $V_d=-2$  V and  $V_g=-20$  V.

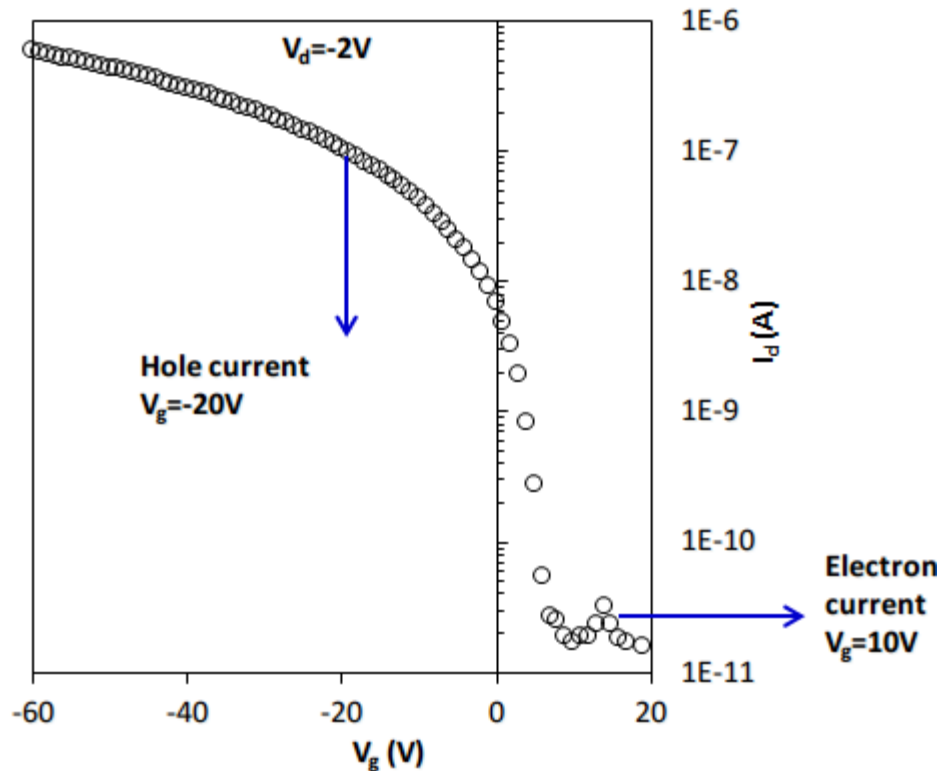


**Figure 6.13. Transfer curves of the device to determine the drain and gate voltage for monitoring electron and hole current as a function of time while turning the light ON/OFF**

Figure 6.14, 6.15 and 6.16 shows the current with and without illumination of PFETs fabricated from PCDTPT, PCDTPT:PCBM blend and PCDTPT/C60 bilayer, respectively. For PCDTPT devices, both hole and electron current remain relatively unchanged under illumination. On the contrary, the hole and electron current of PCDTPT:PCBM blend and PCDTPT/C60 bilayer devices increase under illumination. The change is more significant in PCDTPT/C60 bilayer devices, probably due to the higher electron affinity of C60 compared to PCBM. Remarkably, in PCDTPT/C60 bilayer devices, electron current increases more than two orders of magnitudes under white light. This might hint to an efficient organic photodetector with low and controllable dark current.

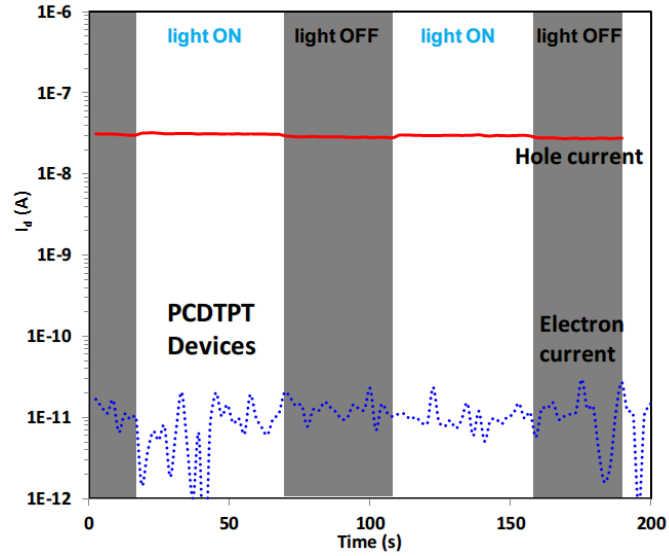


Figure 6.14. Electron and hole current of PCDTPT FETs as a function of time while turning the light ON/OFF

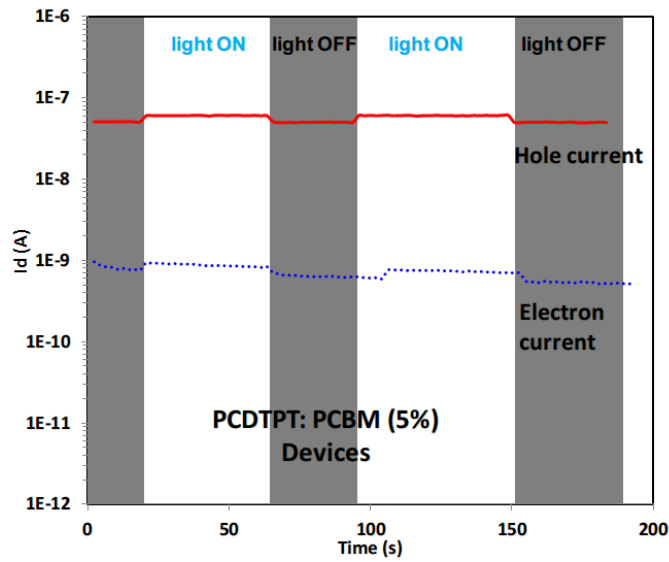
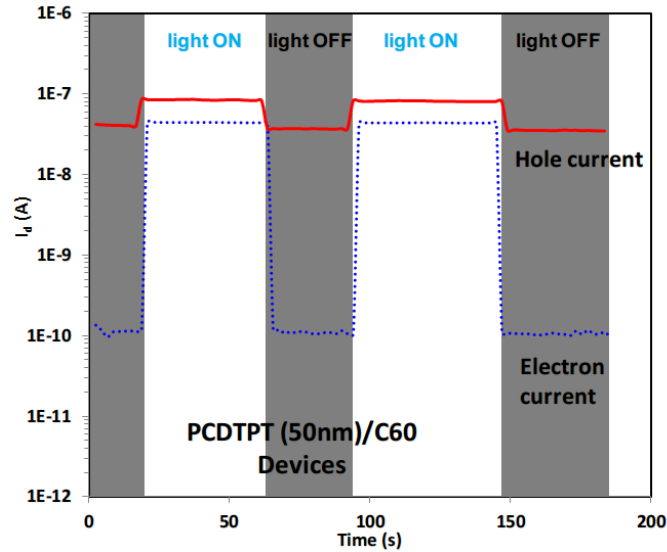


Figure 6.15. Electron and hole current of PCDTPT:PCBM blend FETs as a function of time while turning the light ON/OFF



**Figure 6.16. Electron and hole current of PCDTPT/C60 bilayer FETs as a function of time while turning the light ON/OFF**

#### 6.4.4. Lateral Electron Transport in C60 Layer in PCDTPT/C60 Devices

In this section, the higher OFF current of PCDTPT/C60 devices (**Figure 6.9**) is elucidated. We hypothesize that the continuous conduction pathway in the evaporated C60 can facilitate electron transport between source and drain contacts, resulting in the higher electron current at positive gate biases. Since the C60 domain is more than 30 nm far away from the dielectric interface, its electron current is significantly less dependent on gate voltages. In order to prove this, the electron current at positive biases as a function of temperature (**Figure 6.17**) is further examined. Because of the independence of electron current on gate biases, electron mobility cannot be extracted by common equations for OFETs. Therefore, activation energy of the electron transport is extracted by using the dependency of electron current on temperature (**Figure 6.17b**). The activation energy of electron current is c.a. 130 meV, which is similar to that of electron transport in n-type C60

OFET (**Figure 6.18**). It implies that the hypothesis of lateral electron transport in C60 layer is correct.

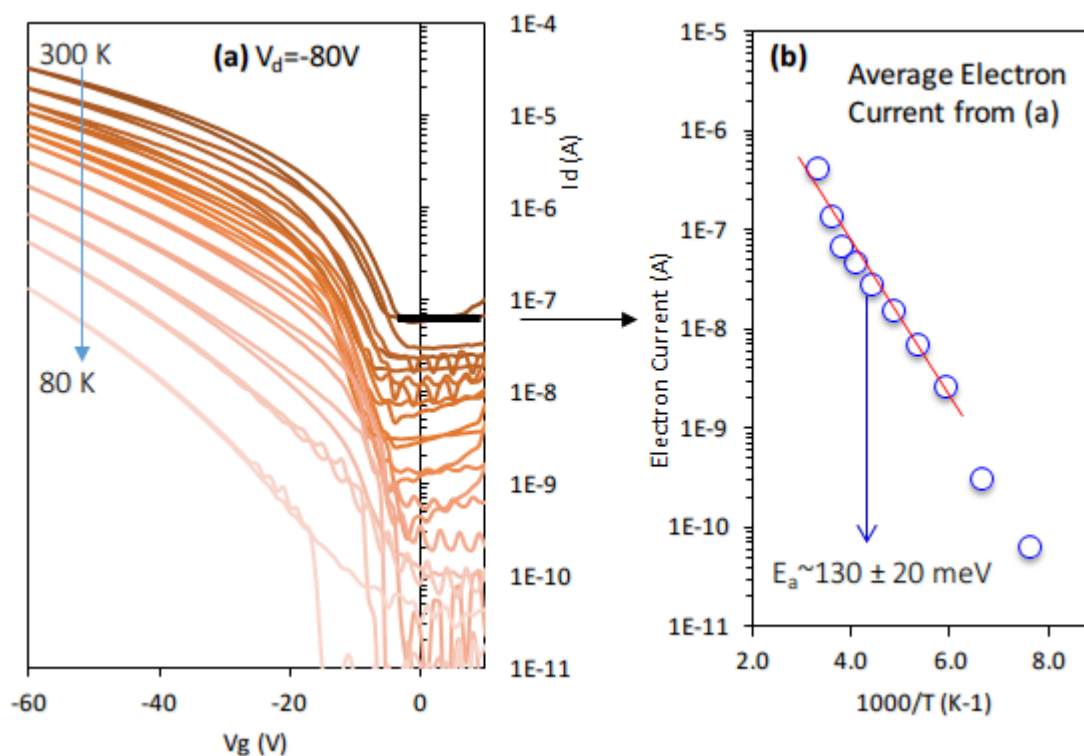


**Figure 6.17. Electron current at positive biases (highlighted by the red line in (a)) plotting as a function of temperature (b) to estimate the activation energy of electron transport in C60 layer in PCDTPT/C60 bilayer FETs**



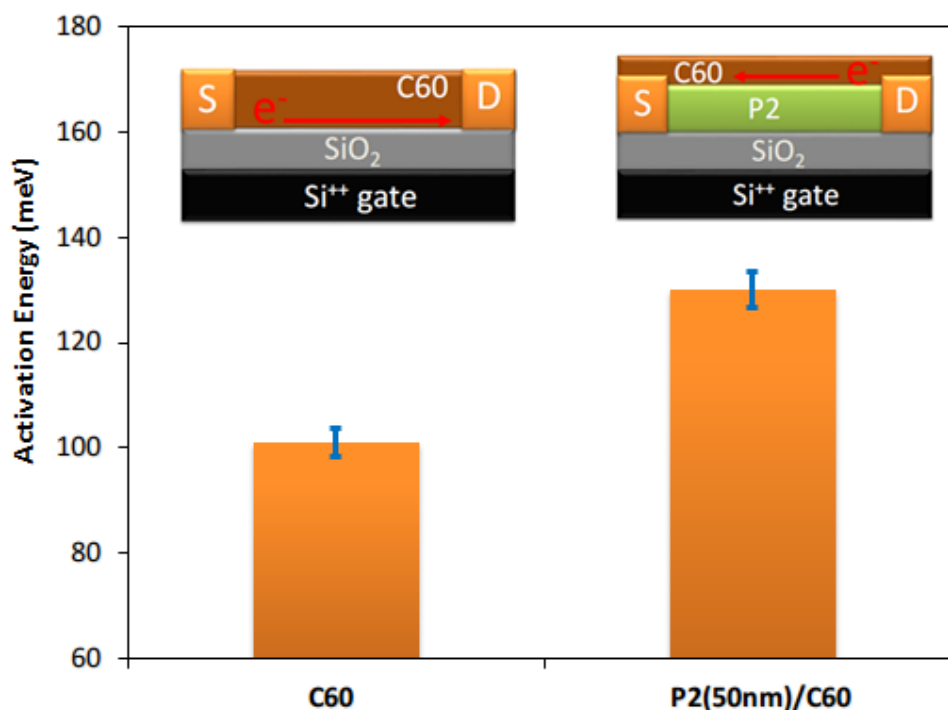


**Figure 6.18. Activation energy of electron transport in C60 layer in PCDTPT/C60 bilayer FETs and in C60 FETs.**

#### 6.4.5. Conclusion

The suppression of electron transport and hence device instability strongly supports the mechanism of the instability and double slope presented in chapter 5. The electrical instability and double slope happens when electrons get trapped at SiO<sub>2</sub> interface and SiO<sup>-</sup> is formed. As stronger electron acceptors (PCBM, C60) present in the device, electrons transfer to the acceptors rather than getting trapped at the SiO<sub>2</sub> interface. Most importantly, the polymer preferably resides at the interface of SiO<sub>2</sub> hence hole transport in the polymer is not disrupted by the acceptors. Negligible electron current observed in PCDTPT:PCBM blend FETs is due to the discontinuous PCBM domain from the source to the drain for electron transport. This is important to achieve low OFF current and high ON/OFF ratios.

## 7. Conclusion & Outlook

### 7.1. Conclusion

This thesis provides a comprehensive study of the structure-processing-property relationship of PFETs fabricated with low band gap D-A copolymers. The polymer chain alignment revealed by high-resolution AFM facilitates the fast charge transport along the polymer chains in PCDTPT FETs. This predominant intrachain charge transport explains the mobility anisotropy between parallel and perpendicular transport with respect to the alignment direction. The tight packing of the polymer chains in solid states, induced by the D-A motif and the rigid backbone, results in small  $\pi$ - $\pi$  stacking distance and hence the low activation energy. The polymer chain alignment and low activation energy explain the superior mobility of PCDTPT FETs.

The most important contribution of this thesis is the elucidation of the instability and double-slope of high mobility p-type FETs made from low band gaps polymers. It is unraveled that the electron trapping at the  $\text{SiO}_2$  interface and the consequent formation of  $-\text{SiO}^-$  result in the instability of hole current and the appearance of the double-slope. The double-slope has triggered a long debate without a solid explanation in the OFET research community. The double-slope makes it ambiguous to determine which slope should be used to calculate the mobility. As shown in chapter 3 of this thesis and in the literature, mobility of a double-slope device can be 10 times different depending on the range of gate voltage. Consequently, the intrinsic mobility of a material and/or a device cannot be properly determined. This thesis reveals that, for p-type OFETs made from low band gap polymers, the higher slope leading to the higher hole mobility at low gate voltage is an artifact caused

by electron trapping. In order to evaluate the intrinsic mobility of an OFET, the electrical instability and the double-slope should be eliminated, by either adding an appropriate electron acceptor or using a hydrophobic, electron-trap-free polymer dielectric material.

New findings in this thesis provide important guidelines for molecular design and device engineering of high-mobility and practical OFETs. These guidelines have been successfully demonstrated, as presented in chapter 6.

## ***7.2. Outlook***

Recently, a few studies suggested that the origin of the double slopes in OFETs is the high contact resistance at low gate voltage.<sup>185,186</sup> In our studies, we know that the double slopes happen only for ambipolar materials with SiO<sub>2</sub> dielectrics, and only occur after bias-stressing in electron conduction regime (or aging). Therefore, studying the contact resistance before and after aging will help to understand whether contact resistance is one of the causes of the double-slope. If the contact resistance remains the same after the bias stress and electron trapping, then one can rule out contact resistance as a cause. Proper measures of contact resistance before and after bias stresses using four-point probe or transfer line method are not reliable because the device is no longer in steady state after bias stresses. Scanning Kelvin Probe Microscopy (SKPM) can be used to probe in-situ the contact resistance in OFET devices right before and after bias stresses. In Nguyen's lab, we develop a set-up where potential drops from a source to a drain of an OFET can be measured by SKPM while drain current can be measured by an external semiconductor analyzer (an Keithley).<sup>187</sup> The resistance along the channel, including contact resistance, from the source to the drain can be calculated from the potential drop and the drain current. The resistance changes at the source/drain contact and along the channel before and after bias stresses will

allow us to investigate the effect of the contact resistance on the device instability and the double-slope. Fundamental understanding the causes of the double slope will help eliminate it and allow one to measure mobility that is intrinsic to the materials.

An emerging class of high-mobility polymers is realized from the fundamental work of this thesis: the high-mobility, wide band-gap non D-A polymers (**Figure 7.1**). The wide band-gap with much shallower LUMO inhibits the electron injection from untreated gold contact. This class of polymers is developed and synthesized by our collaborators, Dr. Ming Wang and Professor Guillermo Bazan, after we understand the origin of the high mobility and the cause of the instability and non-ideality.<sup>162</sup> FET mobility of ca. 3 cm<sup>2</sup>/Vs has been achieved for this class of polymers. Most importantly, those FETs are stable and have high ON-OFF ratio (>10<sup>6</sup>) (unpublished data).

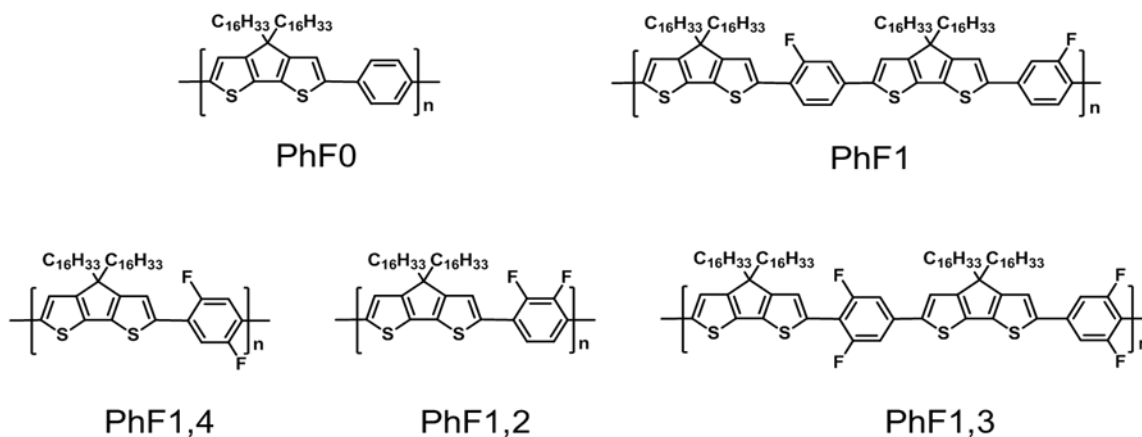


**Figure 7.1. Chemical structures of wide band gap CDT-Ph based polymers.**

Another important research topic originated from this thesis is the studying intrachain charge transport as a function of polymer molecular weight. For FETs fabricated from aligned polymers, this thesis shows that the charge carrier primarily transport along the polymer chains and occasionally hopping to another polymer chain. The length in which the charge moves continuously in a chain before hopping to another chain is not well

understood. Here, we define that length as effective conjugation length (ECL). For conjugated polymers, the ECL is determined by the chemical structure, the planarity of the backbone, and the rigidity of the backbone. For OFETs with aligned polymers, ECL also depends on how well the polymer chains are aligned in the devices.

An aligned conjugated polymer chain is not a perfect molecular-wire because of twists and kinks along the chain. Thus, intrachain charge transport can be disrupted by a certain degree of the imperfection of the alignment and the torsion or twists of the backbone. In such case, charge carrier will hop either to another segment of the same polymer chain or to another polymer chain when the polymer chains are longer than ECL (**Figure 7.2**).

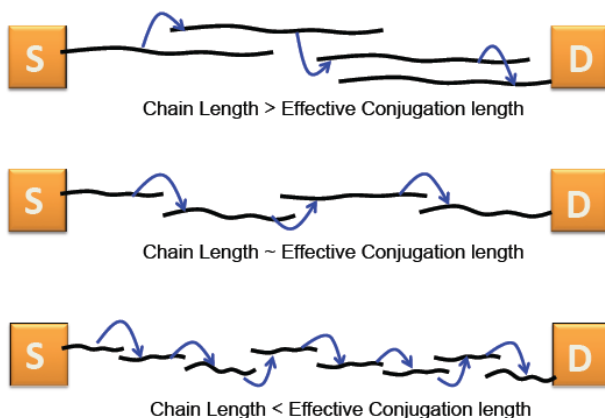


**Figure 7.2. Schematic drawings showing the correlation between polymer molecular weight or polymer chain length and hopping frequency.**

If polymer chains are well aligned, the activation energy, which reflects the interchain hopping, will not depend on MW. In that case, it is legitimate to hypothesize that mobility will depend mainly on the intrachain charge transport along the polymer chains, which is determined by the ECL as discussed above. Therefore, for FETs fabricated from aligned polymer chains, we expect to see an increase of mobility as a function of MWs when the chain length is shorter than the ECL (**Figure 7.2**). This is due to an increase in the distance

at which the charge moves along the chain before hopping. On the other hand, as MWs with chain length longer than ECL, the mobility remains constant because the intrachain charge transport is no longer improved. One can estimate the ECL by using the mobility and activation energy as a function of MW for FETs fabricated from aligned polymer chains. In addition, optical methods such as absorption and photoluminescence can be used to independently estimate the ECL and correlate with the electrically-measured ECL.<sup>188,189</sup> In optical methods, the shift in absorption and/or emission peaks as increasing MW is used to estimate the ECL.<sup>190-192</sup>

In chapter 3, it is shown that the performance of PCDTPT FETs fabricated with aligned polymer chains on nano-groove substrates do not depend on MW ranging from 30 kDa to 300 kDa. This observation may indicate that, for this MW range, the physical chain length does not matter because they are all longer than the ECL (**Figure 7.2**, top).

## 8. References

- (1) Wiley: Physics of Semiconductor Devices, 3rd Edition - Simon M. Sze, Kwok K. Ng.
- (2) Horowitz, G. (1998) Organic Field-Effect Transistors. *Adv. Mater.* 10, 365–377.
- (3) Lilienfeld, J. E. (1930) Method and Apparatus for Controlling Electric Current.
- (4) Edgar, L. J. (1933, March 7) Device for controlling electric current.
- (5) Bardeen, J., and Brattain, W. H. (1948) The Transistor, A Semi-Conductor Triode. *Phys. Rev.* 74, 230–231.
- (6) William, S. (1951, September 25) Circuit element utilizing semiconductive material.
- (7) Brattain, W. H., and John, B. (1952, March 18) Semiconductor amplifier and electrode structures therefor.
- (8) Shockley, W. (1976) The path to the conception of the junction transistor. *IEEE Trans. Electron Devices* 23, 597–620.
- (9) Dawon, K. (1963, August 27) Electric field controlled semiconductor device.
- (10) Arias, A. C., Ready, S. E., Lujan, R., Wong, W. S., Paul, K. E., Salleo, A., Chabinyc, M. L., Apte, R., Street, R. A., Wu, Y., Liu, P., and Ong, B. (2004) All jet-printed polymer thin-film transistor active-matrix backplanes. *Appl. Phys. Lett.* 85, 3304–3306.
- (11) Chabinyc, M. L., and Salleo, A. (2004) Materials Requirements and Fabrication of Active Matrix Arrays of Organic Thin-Film Transistors for Displays. *Chem. Mater.* 16, 4509–4521.
- (12) Xu, L., Gutbrod, S. R., Bonifas, A. P., Su, Y., Sulkin, M. S., Lu, N., Chung, H.-J., Jang, K.-I., Liu, Z., Ying, M., Lu, C., Webb, R. C., Kim, J.-S., Laughner, J. I., Cheng, H., Liu, Y., Ameen, A., Jeong, J.-W., Kim, G.-T., Huang, Y., Efimov, I. R., and Rogers, J. A. (2014) 3D multifunctional integumentary membranes for spatiotemporal cardiac measurements and stimulation across the entire epicardium. *Nat. Commun.* 5.
- (13) Brody, T. P., Asars, J. A., and Dixon, G. D. (1973) A 6 #215; 6 inch 20 lines-per-inch liquid-crystal display panel. *IEEE Trans. Electron Devices* 20, 995–1001.
- (14) Brody, T. P. (1984) The thin film transistor #8212;A late flowering bloom. *IEEE Trans. Electron Devices* 31, 1614–1628.

- (15) Brody, T. P. (1996) The birth and early childhood of active matrix — A personal memoir. *J. Soc. Inf. Disp.* 4, 113–127.
- (16) Chiang, C., Kanicki, J., and Takechi, K. (1998) Electrical Instability of Hydrogenated Amorphous Silicon Thin-Film Transistors for Active-Matrix Liquid-Crystal Displays. *Jpn. J. Appl. Phys.* 37, 4704.
- (17) Deane, S. C., Wehrspohn, R. B., and Powell, M. J. (1998) Unification of the time and temperature dependence of dangling-bond-defect creation and removal in amorphous-silicon thin-film transistors. *Phys. Rev. B* 58, 12625–12628.
- (18) Song, W., Kwon, S. Y., Myung, S., Jung, M. W., Kim, S. J., Min, B. K., Kang, M.-A., Kim, S. H., Lim, J., and An, K.-S. (2014) High-mobility ambipolar ZnO-graphene hybrid thin film transistors. *Sci. Rep.* 4.
- (19) Lin, Y.-H., Faber, H., Zhao, K., Wang, Q., Amassian, A., McLachlan, M., and Anthopoulos, T. D. (2013) High-Performance ZnO Transistors Processed Via an Aqueous Carbon-Free Metal Oxide Precursor Route at Temperatures Between 80–180 °C. *Adv. Mater.* 25, 4340–4346.
- (20) Fleischhaker, F., Wloka, V., and Hennig, I. (2010) ZnO based field-effect transistors (FETs): solution-processable at low temperatures on flexible substrates. *J. Mater. Chem.* 20, 6622–6625.
- (21) Jeong, J. K., Jeong, J. H., Yang, H. W., Park, J.-S., Mo, Y.-G., and Kim, H. D. (2007) High performance thin film transistors with cosputtered amorphous indium gallium zinc oxide channel. *Appl. Phys. Lett.* 91, 113505.
- (22) Park, J.-S., Kim, T.-W., Stryakhilev, D., Lee, J.-S., An, S.-G., Pyo, Y.-S., Lee, D.-B., Mo, Y. G., Jin, D.-U., and Chung, H. K. (2009) Flexible full color organic light-emitting diode display on polyimide plastic substrate driven by amorphous indium gallium zinc oxide thin-film transistors. *Appl. Phys. Lett.* 95, 13503.
- (23) Barbe, D. F., and Westgate, C. R. (1970) Surface state parameters of metal-free phthalocyanine single crystals. *J. Phys. Chem. Solids* 31, 2679–2687.
- (24) Ebisawa, F., Kurokawa, T., and Nara, S. (1983) Electrical properties of polyacetylene/polysiloxane interface. *J. Appl. Phys.* 54, 3255–3259.
- (25) Tsumura, A., Koezuka, H., and Ando, T. (1986) Macromolecular electronic device: Field-effect transistor with a polythiophene thin film. *Appl. Phys. Lett.* 49, 1210–1212.



- (26) Koezuka, H., Tsumura, A., and Ando, T. (1987) Field-effect transistor with polythiophene thin film. *Synth. Met.* 18, 699–704.
- (27) Tsumura, A., Koezuka, H., and Ando, T. (1988) Polythiophene field-effect transistor: Its characteristics and operation mechanism. *Synth. Met.* 25, 11–23.
- (28) Koezuka, H., and Tsumura, A. (1989) Field-effect transistor utilizing conducting polymers. *Synth. Met.* 28, 753–760.
- (29) Facchetti, A., Yoon, M.-H., and Marks, T. J. (2005) Gate Dielectrics for Organic Field-Effect Transistors: New Opportunities for Organic Electronics. *Adv. Mater.* 17, 1705–1725.
- (30) Bobbert, P. A., Sharma, A., Mathijssen, S. G. J., Kemerink, M., and de Leeuw, D. M. (2012) Operational Stability of Organic Field-Effect Transistors. *Adv. Mater.* 24, 1146–1158.
- (31) Baeg, K.-J., Facchetti, A., and Noh, Y.-Y. (2012) Effects of gate dielectrics and their solvents on characteristics of solution-processed N-channel polymer field-effect transistors. *J. Mater. Chem.* 22, 21138–21143.
- (32) Baeg, K.-J., Khim, D., Jung, S.-W., Kang, M., You, I.-K., Kim, D.-Y., Facchetti, A., and Noh, Y.-Y. (2012) Remarkable Enhancement of Hole Transport in Top-Gated N-Type Polymer Field-Effect Transistors by a High-k Dielectric for Ambipolar Electronic Circuits. *Adv. Mater.* 24, 5433–5439.
- (33) She, X.-J., Liu, J., Zhang, J.-Y., Gao, X., and Wang, S.-D. (2013) Operational stability enhancement of low-voltage organic field-effect transistors based on bilayer polymer dielectrics. *Appl. Phys. Lett.* 103, 133303.
- (34) Diao, Y., Tee, B. C.-K., Giri, G., Xu, J., Kim, D. H., Becerril, H. A., Stoltenberg, R. M., Lee, T. H., Xue, G., Mannsfeld, S. C. B., and Bao, Z. (2013) Solution coating of large-area organic semiconductor thin films with aligned single-crystalline domains. *Nat. Mater.* 12, 665–671.
- (35) Minemawari, H., Yamada, T., Matsui, H., Tsutsumi, J., Haas, S., Chiba, R., Kumai, R., and Hasegawa, T. (2011) Inkjet printing of single-crystal films. *Nature* 475, 364–367.
- (36) Li, J., Zhao, Y., Tan, H. S., Guo, Y., Di, C.-A., Yu, G., Liu, Y., Lin, M., Lim, S. H., Zhou, Y., Su, H., and Ong, B. S. (2012) A stable solution-processed polymer semiconductor with record high-mobility for printed transistors. *Sci. Rep.* 2.

- (37) Brown, A. R., Jarrett, C. P., de Leeuw, D. M., and Matters, M. (1997) Field-effect transistors made from solution-processed organic semiconductors. *Synth. Met.* 88, 37–55.
- (38) Kim, C.-H., Bonnassieux, Y., and Horowitz, G. (2014) Compact DC Modeling of Organic Field-Effect Transistors: Review and Perspectives. *IEEE Trans. Electron Devices* 61, 278–287.
- (39) Sirringhaus, H. (2005) Device Physics of Solution-Processed Organic Field-Effect Transistors. *Adv. Mater.* 17, 2411–2425.
- (40) Zaumseil, J., and Sirringhaus, H. (2007) Electron and Ambipolar Transport in Organic Field-Effect Transistors. *Chem. Rev.* 107, 1296–1323.
- (41) Horowitz, G., Hajlaoui, R., Bouchriha, H., Bourguiga, R., and Hajlaoui, M. (1998) The Concept of “Threshold Voltage” in Organic Field-Effect Transistors. *Adv. Mater.* 10, 923–927.
- (42) Abe, Y., Hasegawa, T., Takahashi, Y., Yamada, T., and Tokura, Y. (2005) Control of threshold voltage in pentacene thin-film transistors using carrier doping at the charge-transfer interface with organic acceptors. *Appl. Phys. Lett.* 87, 153506.
- (43) Mathijssen, S. G. J., Cölle, M., Gomes, H., Smits, E. C. P., de Boer, B., McCulloch, I., Bobbert, P. A., and de Leeuw, D. M. (2007) Dynamics of Threshold Voltage Shifts in Organic and Amorphous Silicon Field-Effect Transistors. *Adv. Mater.* 19, 2785–2789.
- (44) Siol, C., Melzer, C., and Seggern, H. von. (2008) Electron trapping in pentacene based p- and n-type organic field-effect transistors. *Appl. Phys. Lett.* 93, 133303.
- (45) Akamatu, H., Inokuchi, H., and Matsunaga, Y. (1956) Organic Semiconductors with High Conductivity. I. Complexes between Polycyclic Aromatic Hydrocarbons and Halogens. *Bull. Chem. Soc. Jpn.* 29, 213–218.
- (46) Kallmann, H., and Pope, M. (1960) Bulk Conductivity in Organic Crystals. *Nature* 186, 31–33.
- (47) Kallmann, H., and Pope, M. (1960) Positive Hole Injection into Organic Crystals. *J. Chem. Phys.* 32, 300–301.
- (48) Mark, P., and Helfrich, W. (1962) Space-Charge-Limited Currents in Organic Crystals. *J. Appl. Phys.* 33, 205–215.
- (49) Helfrich, W., and Schneider, W. G. (1965) Recombination Radiation in Anthracene Crystals. *Phys. Rev. Lett.* 14, 229–231.

- (50) Sano, M., Pope, M., and Kallmann, H. (1965) Electroluminescence and Band Gap in Anthracene. *J. Chem. Phys.* 43, 2920–2921.
- (51) Shirakawa, H., Louis, E. J., MacDiarmid, A. G., Chiang, C. K., and Heeger, A. J. (1977) Synthesis of electrically conducting organic polymers: halogen derivatives of polyacetylene, (CH)<sub>x</sub>. *J. Chem. Soc. Chem. Commun.* 578.
- (52) Su, W. P., Schrieffer, J. R., and Heeger, A. J. (1979) Solitons in Polyacetylene. *Phys. Rev. Lett.* 42, 1698–1701.
- (53) Tang, C. W. (1982, October 26) Organic electroluminescent cell.
- (54) Tang, C. W., and VanSlyke, S. A. (1987) Organic electroluminescent diodes. *Appl. Phys. Lett.* 51, 913–915.
- (55) Tang, C. W., and VanSlyke, S. A. (1989) Organic Electroluminescent Diodes, in *Electroluminescence* (Shionoya, P. S., and Kobayashi, P. H., Eds.), pp 356–357. Springer Berlin Heidelberg.
- (56) Reese, C., Roberts, M., Ling, M., and Bao, Z. (2004) Organic thin film transistors. *Mater. Today* 7, 20–27.
- (57) (2000) The Nobel Prize in Chemistry 2000 - Advanced Information. The Royal Swedish Academy of Sciences, Information Department.
- (58) Salzner, U., Pickup, P. G., Poirier, R. A., and Lagowski, J. B. (1998) Accurate Method for Obtaining Band Gaps in Conducting Polymers Using a DFT/Hybrid Approach. *J. Phys. Chem. A* 102, 2572–2578.
- (59) Allard, S., Forster, M., Souharce, B., Thiem, H., and Scherf, U. (2008) Organic Semiconductors for Solution-Processable Field-Effect Transistors (OFETs). *Angew. Chem. Int. Ed.* 47, 4070–4098.
- (60) Havinga, E., Tenhoeve, W., and Wynberg, H. (1993) Alternate Donor-Acceptor Small-Band-Gap Semiconducting Polymers - Polysquaraines and Polycroconaines. *Synth. Met.* 55, 299–306.
- (61) Deibel, C., Strobel, T., and Dyakonov, V. (2010) Role of the Charge Transfer State in Organic Donor-Acceptor Solar Cells. *Adv. Mater.* 22, 4097–4111.
- (62) Henson, Z. B., Müllen, K., and Bazan, G. C. (2012) Design strategies for organic semiconductors beyond the molecular formula. *Nat. Chem.* 4, 699–704.

- (63) Walker, B., Liu, J., Kim, C., Welch, G. C., Park, J. K., Lin, J., Zalar, P., Proctor, C. M., Seo, J. H., Bazan, G. C., and Nguyen, T.-Q. (2013) Optimization of energy levels by molecular design: evaluation of bis-diketopyrrolopyrrole molecular donor materials for bulk heterojunction solar cells. *Energy Environ. Sci.* 6, 952.
- (64) Sirringhaus, H. (2014) 25th Anniversary Article: Organic Field-Effect Transistors: The Path Beyond Amorphous Silicon. *Adv. Mater.* 26, 1319–1335.
- (65) Ying, L., Hsu, B. B. Y., Zhan, H., Welch, G. C., Zalar, P., Perez, L. A., Kramer, E. J., Nguyen, T.-Q., Heeger, A. J., Wong, W.-Y., and Bazan, G. C. (2011) Regioregular Pyridal[2,1,3]thiadiazole  $\pi$ -Conjugated Copolymers. *J. Am. Chem. Soc.* 133, 18538–18541.
- (66) Li, Y., Sonar, P., Murphy, L., and Hong, W. (2013) High mobility diketopyrrolopyrrole (DPP)-based organic semiconductor materials for organic thin film transistors and photovoltaics. *Energy Environ. Sci.* 6, 1684–1710.
- (67) Tsao, H. N., Cho, D. M., Park, I., Hansen, M. R., Mavrinskiy, A., Yoon, D. Y., Graf, R., Pisula, W., Spiess, H. W., and Müllen, K. (2011) Ultrahigh Mobility in Polymer Field-Effect Transistors by Design. *J. Am. Chem. Soc.* 133, 2605–2612.
- (68) Craciun, N. I., Wildeman, J., and Blom, P. W. M. (2008) Universal Arrhenius Temperature Activated Charge Transport in Diodes from Disordered Organic Semiconductors. *Phys. Rev. Lett.* 100, 56601.
- (69) Blom, P. W. M., and Vissenberg, M. (1998) Dispersive hole transport in poly (p-phenylene vinylene). *Phys. Rev. Lett.* 80, 3819.
- (70) Blom, P. W. M., and De Jong, M. J. M. (1998) Device operation of polymer light-emitting diodes. *Philips J. Res.* 51, 479–494.
- (71) Kuik, M., Wetzelaer, G.-J. A. H., Nicolai, H. T., Craciun, N. I., De Leeuw, D. M., and Blom, P. W. M. (2014) 25th Anniversary Article: Charge Transport and Recombination in Polymer Light-Emitting Diodes. *Adv. Mater.* 26, 512–531.
- (72) Zalar, P., and Nguyen, T.-Q. (2012) Charge Injection Mechanism in PLEDs and Charge Transport in Conjugated Polyelectrolytes, in *Conjugated Polyelectrolytes* (Liu, B., and Bazan, G. C., Eds.), pp 315–344. Wiley-VCH Verlag GmbH & Co. KGaA.
- (73) Zalar, P., Kuik, M., Henson, Z. B., Woellner, C., Zhang, Y., Sharenko, A., Bazan, G. C., and Nguyen, T.-Q. (2014) Increased Mobility Induced by Addition of a Lewis Acid to a Lewis Basic Conjugated Polymer. *Adv. Mater.* 26, 724–727.

- (74) Blom, P. W. M., Mihailetschi, V. D., Koster, L. J. A., and Markov, D. E. (2007) Device Physics of Polymer:Fullerene Bulk Heterojunction Solar Cells. *Adv. Mater.* *19*, 1551–1566.
- (75) Yu, G., and Heeger, A. J. (1995) Charge separation and photovoltaic conversion in polymer composites with internal donor/acceptor heterojunctions. *J. Appl. Phys.* *78*, 4510–4515.
- (76) Oelerich, J. O., Huemmer, D., and Baranovskii, S. D. (2012) How to Find Out the Density of States in Disordered Organic Semiconductors. *Phys. Rev. Lett.* *108*, 226403.
- (77) Albrecht, U., and Bässler, H. (1995) Langevin-Type Charge Carrier Recombination in a Disordered Hopping System. *Phys. Status Solidi B* *191*, 455–459.
- (78) Bässler, H. (1993) Charge Transport in Disordered Organic Photoconductors a Monte Carlo Simulation Study. *Phys. Status Solidi B* *175*, 15–56.
- (79) Arkhipov, V. I., Heremans, P., Emelianova, E. V., and Bässler, H. (2005) Effect of doping on the density-of-states distribution and carrier hopping in disordered organic semiconductors. *Phys. Rev. B* *71*, 45214.
- (80) Nenashev, A. V., Oelerich, J. O., and Baranovskii, S. D. (2015) Theoretical tools for the description of charge transport in disordered organic semiconductors. *J. Phys. Condens. Matter* *27*, 93201.
- (81) Monroe, D. (1985) Hopping in Exponential Band Tails. *Phys. Rev. Lett.* *54*, 146–149.
- (82) Fishchuk, I. I., Kadashchuk, A., Hoffmann, S. T., Athanasopoulos, S., Genoe, J., Bässler, H., and Köhler, A. (2013) Unified description for hopping transport in organic semiconductors including both energetic disorder and polaronic contributions. *Phys. Rev. B* *88*, 125202.
- (83) Stallinga, P. (2011) Electronic Transport in Organic Materials: Comparison of Band Theory with Percolation/(Variable Range) Hopping Theory. *Adv. Mater.* *23*, 3356–3362.
- (84) Coehoorn, R., and Bobbert, P. A. (2012) Effects of Gaussian disorder on charge carrier transport and recombination in organic semiconductors. *Phys. Status Solidi A* *209*, 2354–2377.
- (85) Salleo, A., Chen, T. W., Völkel, A. R., Wu, Y., Liu, P., Ong, B. S., and Street, R. A. (2004) Intrinsic hole mobility and trapping in a regioregular poly(thiophene). *Phys. Rev. B* *70*, 115311.

- (86) Horowitz, G., and Delannoy, P. (1991) An analytical model for organic-based thin-film transistors. *J. Appl. Phys.* 70, 469–475.
- (87) Horowitz, G., Hajlaoui, M. E., and Hajlaoui, R. (2000) Temperature and gate voltage dependence of hole mobility in polycrystalline oligothiophene thin film transistors. *J. Appl. Phys.* 87, 4456.
- (88) Letizia, J. A., Rivnay, J., Facchetti, A., Ratner, M. A., and Marks, T. J. (2010) Variable Temperature Mobility Analysis of n-Channel, p-Channel, and Ambipolar Organic Field-Effect Transistors. *Adv. Funct. Mater.* 20, 50–58.
- (89) Roelofs, W. S. C., Mathijssen, S. G. J., Janssen, R. A. J., de Leeuw, D. M., and Kemerink, M. (2012) Accurate description of charge transport in organic field effect transistors using an experimentally extracted density of states. *Phys. Rev. B* 85, 85202.
- (90) Dong, H., Fu, X., Liu, J., Wang, Z., and Hu, W. (2013) 25th Anniversary Article: Key Points for High-Mobility Organic Field-Effect Transistors. *Adv. Mater.* 25, 6158–6183.
- (91) Lee, W. H., Choi, H. H., Kim, D. H., and Cho, K. (2014) 25th Anniversary Article: Microstructure Dependent Bias Stability of Organic Transistors. *Adv. Mater.* n/a–n/a.
- (92) Sirringhaus, H. (2009) Reliability of Organic Field-Effect Transistors. *Adv. Mater.* 21, 3859–3873.
- (93) Sharma, A., Mathijssen, S. G. J., Kemerink, M., Leeuw, D. M. de, and Bobbert, P. A. (2009) Proton migration mechanism for the instability of organic field-effect transistors. *Appl. Phys. Lett.* 95, 253305.
- (94) Yan, Y., Sun, Q.-J., Gao, X., Deng, P., Zhang, Q., and Wang, S.-D. (2013) Probing bias stress effect and contact resistance in bilayer ambipolar organic field-effect transistors. *Appl. Phys. Lett.* 103, 73303.
- (95) Street, R. A., Salleo, A., and Chabinyc, M. L. (2003) Bipolaron mechanism for bias-stress effects in polymer transistors. *Phys. Rev. B* 68, 85316.
- (96) Sharma, A., Mathijssen, S. G. J., Smits, E. C. P., Kemerink, M., de Leeuw, D. M., and Bobbert, P. A. (2010) Proton migration mechanism for operational instabilities in organic field-effect transistors. *Phys. Rev. B* 82, 75322.
- (97) Sharma, A., Mathijssen, S. G. J., Cramer, T., Kemerink, M., Leeuw, D. M. de, and Bobbert, P. A. (2010) Anomalous current transients in organic field-effect transistors. *Appl. Phys. Lett.* 96, 103306.

- (98) Chua, L.-L., Zaumseil, J., Chang, J.-F., Ou, E. C.-W., Ho, P. K.-H., Sirringhaus, H., and Friend, R. H. (2005) General observation of n-type field-effect behaviour in organic semiconductors. *Nature* 434, 194–199.
- (99) Di Girolamo, F. V., Ciccullo, F., Barra, M., Carella, A., and Cassinese, A. (2012) Investigation on bias stress effects in n-type PDI8-CN2 thin-film transistors. *Org. Electron.* 13, 2281–2289.
- (100) Hu, Y., Lu, Q., Li, H., Zhang, N., and Liu, X. (2013) Low-Voltage, High-Mobility Air-Stable Ambipolar Organic Field-Effect Transistors with a Voltage-Dependent Off-Current State and Modest Operational Stability. *Appl. Phys. Express* 6, 51602.
- (101) Lei, T., Dou, J.-H., Cao, X.-Y., Wang, J.-Y., and Pei, J. (2013) A BDOPV-Based Donor–Acceptor Polymer for High-Performance n-Type and Oxygen-Doped Ambipolar Field-Effect Transistors. *Adv. Mater.* 25, 6589–6593.
- (102) Hamadani, B. H., and Natelson, D. (2004) Temperature-dependent contact resistances in high-quality polymer field-effect transistors. *Appl. Phys. Lett.* 84, 443–445.
- (103) Xu, Y., Gwoziecki, R., Chartier, I., Coppard, R., Balestra, F., and Ghibaudo, G. (2010) Modified transmission-line method for contact resistance extraction in organic field-effect transistors. *Appl. Phys. Lett.* 97, 63302.
- (104) Natali, D., and Caironi, M. (2012) Charge Injection in Solution-Processed Organic Field-Effect Transistors: Physics, Models and Characterization Methods. *Adv. Mater.* 24, 1357–1387.
- (105) Liu, C., Xu, Y., and Noh, Y.-Y. (2015) Contact engineering in organic field-effect transistors. *Mater. Today* 18, 79–96.
- (106) Duong, D. T., Wang, C., Antono, E., Toney, M. F., and Salleo, A. (2013) The chemical and structural origin of efficient p-type doping in P3HT. *Org. Electron.* 14, 1330–1336.
- (107) Duong, D. T., Phan, H., Hanifi, D., Jo, P. S., Nguyen, T.-Q., and Salleo, A. (2014) Direct Observation of Doping Sites in Temperature-Controlled, p-Doped P3HT Thin Films by Conducting Atomic Force Microscopy. *Adv. Mater.* 26, 6069–6073.
- (108) Méndez, H., Heimel, G., Opitz, A., Sauer, K., Barkowski, P., Oehzelt, M., Soeda, J., Okamoto, T., Takeya, J., Arlin, J.-B., Balandier, J.-Y., Geerts, Y., Koch, N., and Salzmann,

- I. (2013) Doping of Organic Semiconductors: Impact of Dopant Strength and Electronic Coupling. *Angew. Chem. Int. Ed.* 52, 7751–7755.
- (109) Kumaki, D., Umeda, T., and Tokito, S. (2008) Reducing the contact resistance of bottom-contact pentacene thin-film transistors by employing a MoO<sub>x</sub> carrier injection layer. *Appl. Phys. Lett.* 92, 13301.
- (110) Kumaki, D., Fujisaki, Y., and Tokito, S. (2013) Reduced contact resistance and highly stable operation in polymer thin-film transistor with aqueous MoO<sub>x</sub> solution contact treatment. *Org. Electron.* 14, 475–478.
- (111) Sun, Y., Takacs, C. J., Cowan, S. R., Seo, J. H., Gong, X., Roy, A., and Heeger, A. J. (2011) Efficient, Air-Stable Bulk Heterojunction Polymer Solar Cells Using MoO<sub>x</sub> as the Anode Interfacial Layer. *Adv. Mater.* 23, 2226–2230.
- (112) Greiner, M. T., and Lu, Z.-H. (2013) Thin-film metal oxides in organic semiconductor devices: their electronic structures, work functions and interfaces. *NPG Asia Mater.* 5, e55.
- (113) Greiner, M. T., Chai, L., Helander, M. G., Tang, W.-M., and Lu, Z.-H. (2013) Metal/Metal-Oxide Interfaces: How Metal Contacts Affect the Work Function and Band Structure of MoO<sub>3</sub>. *Adv. Funct. Mater.* 23, 215–226.
- (114) Malenfant, P. R. L., Dimitrakopoulos, C. D., Gelorme, J. D., Kosbar, L. L., Graham, T. O., Curioni, A., and Andreoni, W. (2002) N-type organic thin-film transistor with high field-effect mobility based on a N,N'-dialkyl-3,4,9,10-perylene tetracarboxylic diimide derivative. *Appl. Phys. Lett.* 80, 2517–2519.
- (115) Zhao, Y., Guo, Y., and Liu, Y. (2013) 25th Anniversary Article: Recent Advances in n-Type and Ambipolar Organic Field-Effect Transistors. *Adv. Mater.* 25, 5372–5391.
- (116) Tseng, H.-R., Ying, L., Hsu, B. B. Y., Perez, L. A., Takacs, C. J., Bazan, G. C., and Heeger, A. J. (2012) High Mobility Field Effect Transistors Based on Macroscopically Oriented Regioregular Copolymers. *Nano Lett.* 12, 6353–6357.
- (117) Tseng, H.-R., Phan, H., Luo, C., Wang, M., Perez, L. A., Patel, S. N., Ying, L., Kramer, E. J., Nguyen, T.-Q., Bazan, G. C., and Heeger, A. J. (2014) High-Mobility Field-Effect Transistors Fabricated with Macroscopic Aligned Semiconducting Polymers. *Adv. Mater.* 26, 2993–2998.
- (118) Iris Visoly-Fisher, S. S. (2011) Scanning Probe Microscopy in Inorganic Thin Films for Solar Cells, in *Advanced characterization techniques for Solar cells*. Wiley.



- (119) Pingree, L. S. C., Reid, O. G., and Ginger, D. S. (2009) Electrical Scanning Probe Microscopy on Active Organic Electronic Devices. *Adv. Mater.* 21, 19–28.
- (120) He, Z., Phan, H., Liu, J., Nguyen, T.-Q., and Tan, T. T. Y. (2013) Understanding TiO<sub>2</sub> Size-Dependent Electron Transport Properties of a Graphene-TiO<sub>2</sub> Photoanode in Dye-Sensitized Solar Cells Using Conducting Atomic Force Microscopy. *Adv. Mater.* 25, 6900–6904.
- (121) Liu, J., Zhang, Y., Phan, H., Sharenko, A., Moonsin, P., Walker, B., Promarak, V., and Nguyen, T.-Q. (2013) Effects of Stereoisomerism on the Crystallization Behavior and Optoelectrical Properties of Conjugated Molecules. *Adv. Mater.* 25, 3645-3650.
- (122) McCulloch, I., Heeney, M., Bailey, C., Genevicius, K., MacDonald, I., Shkunov, M., Sparrowe, D., Tierney, S., Wagner, R., Zhang, W., Chabinyc, M. L., Kline, R. J., McGehee, M. D., and Toney, M. F. (2006) Liquid-crystalline semiconducting polymers with high charge-carrier mobility. *Nat. Mater.* 5, 328–333.
- (123) Yan, H., Chen, Z., Zheng, Y., Newman, C., Quinn, J. R., Dötz, F., Kastler, M., and Facchetti, A. (2009) A high-mobility electron-transporting polymer for printed transistors. *Nature* 457, 679–686.
- (124) Chen, H., Guo, Y., Yu, G., Zhao, Y., Zhang, J., Gao, D., Liu, H., and Liu, Y. (2012) Highly  $\pi$ -Extended Copolymers with Diketopyrrolopyrrole Moieties for High-Performance Field-Effect Transistors. *Adv. Mater.* 24, 4618–4622.
- (125) Sirringhaus, H., Wilson, R. J., Friend, R. H., Inbasekaran, M., Wu, W., Woo, E. P., Grell, M., and Bradley, D. D. C. (2000) Mobility enhancement in conjugated polymer field-effect transistors through chain alignment in a liquid-crystalline phase. *Appl. Phys. Lett.* 77, 406–408.
- (126) Pisula, W., Menon, A., Stepputat, M., Lieberwirth, I., Kolb, U., Tracz, A., Sirringhaus, H., Pakula, T., and Müllen, K. (2005) A Zone-Casting Technique for Device Fabrication of Field-Effect Transistors Based on Discotic Hexa-peri-hexabenzocoronene. *Adv. Mater.* 17, 684–689.
- (127) Duffy, C. M., Andreasen, J. W., Breiby, D. W., Nielsen, M. M., Ando, M., Minakata, T., and Sirringhaus, H. (2008) High-Mobility Aligned Pentacene Films Grown by Zone-Casting. *Chem. Mater.* 20, 7252–7259.

- (128) DeLongchamp, D. M., Kline, R. J., Jung, Y., Germack, D. S., Lin, E. K., Moad, A. J., Richter, L. J., Toney, M. F., Heeney, M., and McCulloch, I. (2009) Controlling the Orientation of Terraced Nanoscale “Ribbons” of a Poly(thiophene) Semiconductor. *ACS Nano* 3, 780–787.
- (129) Li, L., Gao, P., Schuermann, K. C., Ostendorp, S., Wang, W., Du, C., Lei, Y., Fuchs, H., Cola, L. D., Müllen, K., and Chi, L. (2010) Controllable Growth and Field-Effect Property of Monolayer to Multilayer Microstripes of an Organic Semiconductor. *J. Am. Chem. Soc.* 132, 8807–8809.
- (130) Kim, B.-G., Jeong, E. J., Chung, J. W., Seo, S., Koo, B., and Kim, J. (2013) A molecular design principle of lyotropic liquid-crystalline conjugated polymers with directed alignment capability for plastic electronics. *Nat. Mater.* 12, 659–664.
- (131) Brinkmann, M., and Rannou, P. (2009) Molecular Weight Dependence of Chain Packing and Semicrystalline Structure in Oriented Films of Regioregular Poly(3-hexylthiophene) Revealed by High-Resolution Transmission Electron Microscopy. *Macromolecules* 42, 1125–1130.
- (132) Kline, R. J., McGehee, M. D., Kadnikova, E. N., Liu, J., Fréchet, J. M. J., and Toney, M. F. (2005) Dependence of Regioregular Poly(3-hexylthiophene) Film Morphology and Field-Effect Mobility on Molecular Weight. *Macromolecules* 38, 3312–3319.
- (133) Kline, R. j., McGehee, M. d., Kadnikova, E. n., Liu, J., and Fréchet, J. m. j. (2003) Controlling the Field-Effect Mobility of Regioregular Polythiophene by Changing the Molecular Weight. *Adv. Mater.* 15, 1519–1522.
- (134) Jimison, L. H., Toney, M. F., McCulloch, I., Heeney, M., and Salleo, A. (2009) Charge-Transport Anisotropy Due to Grain Boundaries in Directionally Crystallized Thin Films of Regioregular Poly(3-hexylthiophene). *Adv. Mater.* 21, 1568–1572.
- (135) Rivnay, J., Jimison, L. H., Northrup, J. E., Toney, M. F., Noriega, R., Lu, S., Marks, T. J., Facchetti, A., and Salleo, A. (2009) Large modulation of carrier transport by grain-boundary molecular packing and microstructure in organic thin films. *Nat. Mater.* 8, 952–958.
- (136) Noriega, R., Rivnay, J., Vandewal, K., Koch, F. P. V., Stingelin, N., Smith, P., Toney, M. F., and Salleo, A. (2013) A general relationship between disorder, aggregation and charge transport in conjugated polymers. *Nat. Mater.* advance online publication.

- (137) Grévin, B., Rannou, P., Payerne, R., Pron, A., and Travers, J.-P. (2003) Scanning Tunneling Microscopy Investigations of Self-Organized Poly(3-hexylthiophene) Two-Dimensional Polycrystals. *Adv. Mater.* *15*, 881–884.
- (138) Zhang, M., Tsao, H. N., Pisula, W., Yang, C., Mishra, A. K., and Müllen, K. (2007) Field-Effect Transistors Based on a Benzothiadiazole–Cyclopentadithiophene Copolymer. *J. Am. Chem. Soc.* *129*, 3472–3473.
- (139) Tsao, H. N., and Müllen, K. (2010) Improving polymer transistor performance via morphology control. *Chem. Soc. Rev.* *39*, 2372–2386.
- (140) Zhang, X., Bronstein, H., Kronemeijer, A. J., Smith, J., Kim, Y., Kline, R. J., Richter, L. J., Anthopoulos, T. D., Siringhaus, H., Song, K., Heeney, M., Zhang, W., McCulloch, I., and DeLongchamp, D. M. (2013) Molecular origin of high field-effect mobility in an indacenodithiophene–benzothiadiazole copolymer. *Nat. Commun.* *4*.
- (141) Sakanoue, T., and Siringhaus, H. (2010) Band-like temperature dependence of mobility in a solution-processed organic semiconductor. *Nat. Mater.* *9*, 736–740.
- (142) Minder, N. A., Ono, S., Chen, Z., Facchetti, A., and Morpurgo, A. F. (2012) Band-Like Electron Transport in Organic Transistors and Implication of the Molecular Structure for Performance Optimization. *Adv. Mater.* *24*, 503–508.
- (143) Stallinga, P., Gomes, H. L., Biscarini, F., Murgia, M., and Leeuw, D. M. de. (2004) Electronic transport in field-effect transistors of sexithiophene. *J. Appl. Phys.* *96*, 5277–5283.
- (144) Gomes, H. L., Stallinga, P., Cölle, M., de Leeuw, D. M., and Biscarini, F. (2006) Electrical instabilities in organic semiconductors caused by trapped supercooled water. *Appl. Phys. Lett.* *88*, 82101-82101–3.
- (145) Nicolai, H. T., Kuik, M., Wetzelaer, G. a. H., de Boer, B., Campbell, C., Risko, C., Brédas, J. L., and Blom, P. W. M. (2012) Unification of trap-limited electron transport in semiconducting polymers. *Nat. Mater.* *11*, 882–887.
- (146) Nicolai, H. T. (2012) Device physics of white polymer light-emitting diodes. s.n.] ; University Library Groningen] [Host], S.I.; Groningen.
- (147) Street, R. A., Northrup, J. E., and Salleo, A. (2005) Transport in polycrystalline polymer thin-film transistors. *Phys. Rev. B* *71*, 165202.

- (148) Mattias Andersson, L., Osikowicz, W., Jakobsson, F. L. E., Berggren, M., Lindgren, L., Andersson, M. R., and Inganäs, O. (2008) Intrinsic and extrinsic influences on the temperature dependence of mobility in conjugated polymers. *Org. Electron.* *9*, 569–574.
- (149) Hamadani, B. H., and Natelson, D. (2004) Temperature-dependent contact resistances in high-quality polymer field-effect transistors. *Appl. Phys. Lett.* *84*, 443–445.
- (150) Lee, M. J., Gupta, D., Zhao, N., Heeney, M., McCulloch, I., and Sirringhaus, H. (2011) Anisotropy of Charge Transport in a Uniaxially Aligned and Chain-Extended, High-Mobility, Conjugated Polymer Semiconductor. *Adv. Funct. Mater.* *21*, 932–940.
- (151) Ha, T.-J., Sonar, P., and Dodabalapur, A. (2013) Charge transport study of high mobility polymer thin-film transistors based on thiophene substituted diketopyrrolopyrrole copolymers. *Phys. Chem. Chem. Phys.* *15*, 9735–9741.
- (152) Perez, L. A., Zalar, P., Ying, L., Schmidt, K., Toney, M. F., Nguyen, T.-Q., Bazan, G. C., and Kramer, E. J. (2014) Effect of Backbone Regioregularity on the Structure and Orientation of a Donor-Acceptor Semiconducting Copolymer. *Macromolecules* *47*, 1403–1410.
- (153) Chabinyk, M. L. (2008) X-ray Scattering from Films of Semiconducting Polymers. *Polym. Rev.* *48*, 463–492.
- (154) Kim, G., Kang, S.-J., Dutta, G. K., Han, Y.-K., Shin, T. J., Noh, Y.-Y., and Yang, C. (2014) A Thienoisindigo-Naphthalene Polymer with Ultrahigh Mobility of 14.4 cm<sup>2</sup>/V·s That Substantially Exceeds Benchmark Values for Amorphous Silicon Semiconductors. *J. Am. Chem. Soc.* *136*, 9477–9483.
- (155) Luo, C., Kyaw, A. K. K., Perez, L. A., Patel, S., Wang, M., Grimm, B., Bazan, G. C., Kramer, E. J., and Heeger, A. J. (2014) General Strategy for Self-Assembly of Highly Oriented Nanocrystalline Semiconducting Polymers with High Mobility. *Nano Lett.* *14*, 2764–2771.
- (156) Guo, Y., Yu, G., and Liu, Y. (2010) Functional Organic Field-Effect Transistors. *Adv. Mater.* *22*, 4427–4447.
- (157) Kang, M. S., and Frisbie, C. D. (2013) A Pedagogical Perspective on Ambipolar FETs. *ChemPhysChem* *14*, 1547–1552.
- (158) Kang, I., An, T. K., Hong, J., Yun, H.-J., Kim, R., Chung, D. S., Park, C. E., Kim, Y.-H., and Kwon, S.-K. (2013) Effect of Selenophene in a DPP Copolymer Incorporating a

Vinyl Group for High-Performance Organic Field-Effect Transistors. *Adv. Mater.* 25, 524–528.

(159) Smits, E. C. P., Anthopoulos, T. D., Setayesh, S., van Veenendaal, E., Coehoorn, R., Blom, P. W. M., de Boer, B., and de Leeuw, D. M. (2006) Ambipolar charge transport in organic field-effect transistors. *Phys. Rev. B* 73, 205316.

(160) Aguirre, C. M., Levesque, P. L., Paillet, M., Lapointe, F., St-Antoine, B. C., Desjardins, P., and Martel, R. (2009) The Role of the Oxygen/Water Redox Couple in Suppressing Electron Conduction in Field-Effect Transistors. *Adv. Mater.* 21, 3087–3091.

(161) Mathijssen, S. G. J., Spijkman, M.-J., Andringa, A.-M., van Hal, P. A., McCulloch, I., Kemerink, M., Janssen, R. A. J., and de Leeuw, D. M. (2010) Revealing Buried Interfaces to Understand the Origins of Threshold Voltage Shifts in Organic Field-Effect Transistors. *Adv. Mater.* 22, 5105–5109.

(162) Phan, H., Wang, M., Bazan, G. C., and Nguyen, T.-Q. (2015) Electrical Instability Induced by Electron Trapping in Low-Bandgap Donor–Acceptor Polymer Field-Effect Transistors. *Adv. Mater.* 27, 7004–7009.

(163) Barra, M., Girolamo, F. V. D., Chiarella, F., Salluzzo, M., Chen, Z., Facchetti, A., Anderson, L., and Cassinese, A. (2010) Transport Property and Charge Trap Comparison for N-Channel Perylene Diimide Transistors with Different Air-Stability†. *J. Phys. Chem. C* 114, 20387–20393.

(164) Ford, M., Phan, H., Wang, M., Bazan, G. C., and Nguyen, T.-Q. (2016) Fullerenes improve the stability of high mobility p-type organic field-effect transistors. *Submitted*.

(165) Ford, M. J., Wang, M., Patel, S. N., Phan, H., Segalman, R. A., Nguyen, T.-Q., and Bazan, G. C. (2016) High Mobility Organic Field-Effect Transistors from Majority Insulator Blends. *Chem. Mater.*

(166) Wang, M., Ford, M., Phan, H., Coughlin, J., Nguyen, T.-Q., and Bazan, G. C. (2016) Fluorine substitution influence on benzo[2,1,3]thiadiazole based polymers for field-effect transistor applications. *Chem. Commun.* 52, 3207–3210.

(167) Chiu, C.-Y., Wang, H., Phan, H., Shiratori, K., Nguyen, T.-Q., and Hawker, C. J. (2016) Twisted olefinic building blocks for low bandgap polymers in solar cells and ambipolar field-effect transistors. *J. Polym. Sci. Part Polym. Chem.* 54, 889–899.

- (168) Bronstein, H., Chen, Z., Ashraf, R. S., Zhang, W., Du, J., Durrant, J. R., Shakya Tuladhar, P., Song, K., Watkins, S. E., Geerts, Y., Wienk, M. M., Janssen, R. A. J., Anthopoulos, T., Sirringhaus, H., Heeney, M., and McCulloch, I. (2011) Thieno[3,2-b]thiophene–Diketopyrrolopyrrole-Containing Polymers for High-Performance Organic Field-Effect Transistors and Organic Photovoltaic Devices. *J. Am. Chem. Soc.* *133*, 3272–3275.
- (169) Kang, I., Yun, H.-J., Chung, D. S., Kwon, S.-K., and Kim, Y.-H. (2013) Record High Hole Mobility in Polymer Semiconductors via Side-Chain Engineering. *J. Am. Chem. Soc.* *135*, 14896–14899.
- (170) Nketia-Yawson, B., Lee, H.-S., Seo, D., Yoon, Y., Park, W.-T., Kwak, K., Son, H. J., Kim, B., and Noh, Y.-Y. (2015) A Highly Planar Fluorinated Benzothiadiazole-Based Conjugated Polymer for High-Performance Organic Thin-Film Transistors. *Adv. Mater.* *27*, 3045–3052.
- (171) Lee, J., Han, A.-R., Yu, H., Shin, T. J., Yang, C., and Oh, J. H. (2013) Boosting the Ambipolar Performance of Solution-Processable Polymer Semiconductors via Hybrid Side-Chain Engineering. *J. Am. Chem. Soc.* *135*, 9540–9547.
- (172) Han, A.-R., Dutta, G. K., Lee, J., Lee, H. R., Lee, S. M., Ahn, H., Shin, T. J., Oh, J. H., and Yang, C. (2015)  $\epsilon$ -Branched Flexible Side Chain Substituted Diketopyrrolopyrrole-Containing Polymers Designed for High Hole and Electron Mobilities. *Adv. Funct. Mater.* *25*, 247–254.
- (173) Choi, H. H., Baek, J. Y., Song, E., Kang, B., Cho, K., Kwon, S.-K., and Kim, Y.-H. (2015) A Pseudo-Regular Alternating Conjugated Copolymer Using an Asymmetric Monomer: A High-Mobility Organic Transistor in Nonchlorinated Solvents. *Adv. Mater.* *27*, 3626–3631.
- (174) He, M., Li, W., Gao, Y., Tian, H., Zhang, J., Tong, H., Yan, D., Geng, Y., and Wang, F. (2016) Donor–Acceptor Conjugated Polymers Based on Dithieno[3,2-b:3',2'-b']naphtho[1,2-b:5,6-b']dithiophene: Synthesis and Semiconducting Properties. *Macromolecules* *49*, 825–832.
- (175) Bobbert, P. A., Sharma, A., Mathijssen, S. G. J., Kemerink, M., and de Leeuw, D. M. (2012) Operational Stability of Organic Field-Effect Transistors. *Adv. Mater.* *24*, 1146–1158.

- (176) Hartmann, L., Tremel, K., Uttiya, S., Crossland, E., Ludwigs, S., Kayunkid, N., Vergnat, C., and Brinkmann, M. (2011) 2D Versus 3D Crystalline Order in Thin Films of Regioregular Poly(3-hexylthiophene) Oriented by Mechanical Rubbing and Epitaxy. *Adv. Funct. Mater.* 21, 4047–4057.
- (177) Biniek, L., Leclerc, N., Heiser, T., Bechara, R., and Brinkmann, M. (2013) Large Scale Alignment and Charge Transport Anisotropy of pBTTT Films Oriented by High Temperature Rubbing. *Macromolecules* 46, 4014–4023.
- (178) Brinkmann, M., Hartmann, L., Biniek, L., Tremel, K., and Kayunkid, N. (2014) Orienting Semi-Conducting  $\pi$ -Conjugated Polymers. *Macromol. Rapid Commun.* 35, 9–26.
- (179) Hoogboom, J., Rasing, T., Rowan, A. E., and Nolte, R. J. M. (2006) LCD alignment layers. Controlling nematic domain properties. *J. Mater. Chem.* 16, 1305–1314.
- (180) Chamberlain, G. A. (1983) Organic solar cells: a review. *Sol. Cells* 8, 47–83.
- (181) Zhang, Y., Liu, J., and Nguyen, T.-Q. (2013) Photoresponse of Donor/Acceptor Blends in Organic Transistors: A Tool for Understanding Field-Assisted Charge Separation in Small Molecule Bulk Heterojunction Solar Cells. *ACS Appl. Mater. Interfaces* 5, 2347–2353.
- (182) Love, J. A., Proctor, C. M., Liu, J., Takacs, C. J., Sharenko, A., van der Poll, T. S., Heeger, A. J., Bazan, G. C., and Nguyen, T.-Q. (2013) Film Morphology of High Efficiency Solution-Processed Small-Molecule Solar Cells. *Adv. Funct. Mater.* n/a–n/a.
- (183) Walker, B., Tamayo, A. B., Dang, X., Zalar, P., Seo, J. H., Garcia, A., Tantiwiwat, M., and Nguyen, T. (2009) Nanoscale Phase Separation and High Photovoltaic Efficiency in Solution-Processed, Small-Molecule Bulk Heterojunction Solar Cells. *Adv. Funct. Mater.* 19, 3063–3069.
- (184) Kippelen, B., and Bredas, J.-L. (2009) Organic photovoltaics. *Energy Env. Sci* 2, 251–261.
- (185) Bittle, E. G., Basham, J. I., Jackson, T. N., Jurchescu, O. D., and Gundlach, D. J. (2016) Mobility overestimation due to gated contacts in organic field-effect transistors. *Nat. Commun.* 7, 10908.
- (186) Uemura, T., Rolin, C., Ke, T.-H., Fesenko, P., Genoe, J., Heremans, P., and Takeya, J. (2016) On the Extraction of Charge Carrier Mobility in High-Mobility Organic Transistors. *Adv. Mater.* 28, 151–155.

- (187) Mikhnenko, O. V., Collins, S. D., and Nguyen, T.-Q. (2015) Rectifying Electrical Noise with an Ionic-Organic Ratchet. *Adv. Mater.* 27, 2007–2012.
- (188) Meier, H., Stalmach, U., and Kolshorn, H. (1997) Effective conjugation length and UV/vis spectra of oligomers. *Acta Polym.* 48, 379–384.
- (189) Rissler, J. (2004) Effective conjugation length of  $\pi$ -conjugated systems. *Chem. Phys. Lett.* 395, 92–96.
- (190) Klaerner, G., and Miller, R. D. (1998) Polyfluorene Derivatives: Effective Conjugation Lengths from Well-Defined Oligomers. *Macromolecules* 31, 2007–2009.
- (191) Izumi, T., Kobashi, S., Takimiya, K., Aso, Y., and Otsubo, T. (2003) Synthesis and Spectroscopic Properties of a Series of  $\beta$ -Blocked Long Oligothiophenes up to the 96-mer: Reevaluation of Effective Conjugation Length. *J. Am. Chem. Soc.* 125, 5286–5287.
- (192) Asada, K., Kobayashi, T., and Naito, H. (2006) Control of Effective Conjugation Length in Polyfluorene Thin Films. *Jpn. J. Appl. Phys.* 45, L247–L249.



## 9. Appendix

### *9.1. New program to measure the hole current dynamic under different bias stresses at different time intervals*

```
int i,k,t;

clock_t tStart;

double ExpTime;

//initiate output parameters

for (i=0; i<NumSam+NumRe; i++){

    Idt_arr[i]=0;

    Igt_arr[i]=0;

    Time[i]=0;

}

// applying initial biases from input Vst, Vdt, Vgt

forcev(SMU4,Vst);

forcev(SMU2,Vdt);

forcev(SMU3,Vgt);

//measuring initial current

tStart=clock();

TimeClock[0]=(clock()-tStart)*1.0/CLOCKS_PER_SEC;

Time[0]=0*(interval_ms+500)/1000;
```

```

intgi(SMU2,&Idt_arr[0]);

intgi(SMU3,&Igt_arr[0]);

//measuring current as stressing

for (k=1;k<NumSam;k++){

    delay(interval_ms);

    TimeClock[k]=(clock()-tStart)*1.0/CLOCKS_PER_SEC;

    Time[k]=k*(interval_ms+500)/1000;

    intgi(SMU2,&Idt_arr[k]);

    intgi(SMU3,&Igt_arr[k]);

}

//measure current as the device is recovered

forcev(SMU2,Vdr);//Apply recovery bias to the drain

forcev(SMU3,Vgr);//Apply recovery bias to the gate

//this part is for using an exponentially increase time interval with measuring time

t=0;//set the counting for exponential time interval

for (k=NumSam;k<NumSam+NumRe;k++){

    t=t+1;

    ExpTime=ExpConst*1000+exp(ExpCoeff*sqrt(t));

    delay((long)ExpTime);//ground the electrode in ExpTime (ms)

//for a constant time interval, a constant interval can be set as an input parameter instead
of ExpTime above

```

```

forcev(SMU2,Vdt);//set back the drain

forcev(SMU3,Vgt);//set back the gate

delay(TransTime);//Pulse bias to measure current

TimeClock[k]=(clock()-tStart)*1.0/CLOCKS_PER_SEC;

Time[k]=Time[k-1]+(ExpTime+TransTime+500.0)/1000.0;

intgi(SMU2,&Idt_arr[k]);

intgi(SMU3,&Igt_arr[k]);

    forcev(SMU2,Vdr);//Apply recovery bias to the drain

    forcev(SMU3,Vgr);//Apply recovery bias to the gate
}

return;

```

## 9.2. *Structural and optoelectronic properties of hybrid bulk-heterojunction materials based on conjugated small molecules and mesostructured TiO<sub>2</sub>*

### 9.2.1. Introduction

Hybrid systems comprising of organic semiconductors (OSc) and wide band-gap inorganic nanocrystals (i.e ZnO, TiO<sub>2</sub>) have great potentials for both scientific studies and the creation of practical optoelectronic materials. Among different inorganic materials, TiO<sub>2</sub> has been intensively studied in hybrid devices since early 1990's.<sup>1-5</sup> TiO<sub>2</sub> is an attractive material, due to its environmental stability, low-cost, and non-toxic properties. For most  $\pi$ -conjugated OSc, the electron affinity ( $\sim 3.0 - 4.0$  eV) is less than that of TiO<sub>2</sub> ( $\sim 4.2$  eV). Therefore, photoexcited electrons through  $\pi$ - $\pi^*$  transition of OSc are thermodynamically allowed to transfer to the conduction band of TiO<sub>2</sub>, leaving holes in the OSc. The

photoinduced charge transfer at the interface of TiO<sub>2</sub>-organic hybrid materials enables it to be applicable in photo-sensing devices, such as photoconductors and photovoltaics. Upon charge transfer, electrons and holes transport in TiO<sub>2</sub> and organic material, respectively, then being collected at electrodes. There are three critical factors affecting the performance of such hybrid TiO<sub>2</sub>-OSc devices: photon absorption, charge separation and charge transport. Mesoporous TiO<sub>2</sub> has been utilized efficiently in different devices, especially in dye-sensitized solar cells (DSSC)<sup>6</sup>, due to its high interfacial area for efficient charge separation. It should be noted that DSSC employs a third material as the hole transporter while dyes are used for light absorbing only. In another type of mesoporous TiO<sub>2</sub> hybrid devices, a single organic component is loaded into mesopores for both functions: absorbing light and conducting holes.<sup>5,7</sup> In that case, high loading of OSc is desired to absorb more light and result in more photogenerated carriers. In addition, the organic domain, which is presumably the mesopore domain, should be continuous for hole transport and small enough (~5-20 nm)<sup>5,8</sup> for excitons created in OSc to diffuse to the interface and undergo charge separation.

Conjugated polymers (CPs) are the most widely studied materials to combine with mesoporous TiO<sub>2</sub> due to their high absorption coefficients and hole mobilities.<sup>4</sup> In the TiO<sub>2</sub>-conjugated polymer (TiO<sub>2</sub>-CP) hybrid system, difficulty arises in gaining efficient infiltration into the pores using viscous polymer solutions that contain long polymer chains.<sup>9,10</sup> Additionally, the hydrophilic nature of TiO<sub>2</sub> repels the hydrophobic CPs, leading to reduced polymer loadings and inefficient charge transfer from photo-excited conjugated polymers to TiO<sub>2</sub>.<sup>11</sup> For example, it has been shown that the low loading of CPs in TiO<sub>2</sub>-CP hybrid solar cells results in low short circuit current.<sup>12,13</sup> Numerous efforts have been made to improve the loading and charge transfer of polymers to mesoporous TiO<sub>2</sub>. One approach involves treating the surface of TiO<sub>2</sub> with interfacial modifiers, such as common dyes<sup>9,11,14,15</sup>

used in DSSCs or carboxylated oligothiophene derivatives<sup>7,15</sup>, thus making it more energetically compatible with conjugated polymers. Using this method, charge transfer to the TiO<sub>2</sub> can be enhanced drastically.<sup>7,11,15</sup> Even still, the infiltration of conjugated polymers into mesoporous TiO<sub>2</sub> is still challenging since the majority of loadings reported in literature without further surface treatment of TiO<sub>2</sub> is less than 10%.<sup>9,10</sup>

We proposed an improved hybrid system comprises of mesostructured TiO<sub>2</sub> and small conjugated molecules. Firstly, mesostructured TiO<sub>2</sub> has high surface area and continuous mesopores for efficient charge separation and charge transport. In addition, its well-defined structure provides an appealing platform for both theoretical predictions and then experimental validation of the performance of HSCs and OSCs.<sup>16</sup> Secondly, SMs may be able to achieve higher loadings into mesoporous TiO<sub>2</sub>, compared to conjugated polymers, due to their smaller size, resulting in less viscous solutions and facile diffusion into the mesopores. In addition, incorporation of heteroatoms like oxygen and nitrogen in the backbone of SMs makes them more hydrophilic than most conjugated polymers. This is expected to yield improved loadings and more efficient charge transfer to the hydrophilic TiO<sub>2</sub> network.<sup>17</sup> To test our hypothesis, we used a benzofuran substituted diketopyrrolopyrrole, DPP(TBFu)<sub>2</sub>,<sup>18</sup> as a model small molecule; owing to its relatively low molecular weight and the presence of oxygen atoms in the benzofuran units, which makes it relatively more hydrophilic. DPP(TBFu)<sub>2</sub> has already achieved PCEs of around 5% using conventional bulk-heterojunction (BHJ) device architectures that use a fullerene derivative as the acceptor.<sup>18</sup> In addition, it has been extensively characterized to understand the nanoscale morphology and optoelectronic properties of BHJ OSCs.<sup>18,19</sup> In this study, we show that the hybrid TiO<sub>2</sub>-small molecule system is a promising candidate for optoelectronic devices.

### 9.2.2. Material Fabrication and Small Molecule Loading Calculations

Mesostructured TiO<sub>2</sub> films were prepared following a method developed by Frey and coworkers and applied in polymer HSCs.<sup>20-22</sup> The mesostructured TiO<sub>2</sub> films were prepared from a solution of THF in concentrated HCl (12.1 M) containing the TiO<sub>2</sub> precursor, tetraethylorthotitanate, and the triblock copolymer Pluronic™ F127.<sup>20</sup> The films were spin-cast from solution onto glass or patterned indium-tin-oxide (ITO) substrates. Subsequently the films were dried for several days and then calcined in air at 350 °C for 12 hrs to introduce porosity. Small-angle X-ray scattering (SAXS) was used to confirm the presence of mesostructural order before and after calcination and the resulting patterns are shown in **Figure 9.1**. In both cases, a single reflection was observed at a 2θ angle of 0.7°, corresponding to a *d*-spacing of 12.5 nm, a value consistent with the cubic phase reported in the literature.<sup>20</sup> The lack of framework contraction upon calcination is likely due to the low temperature of the calcination. Porosimetry data of mesostructured TiO<sub>2</sub> film were also collected, and the films were found to have a surface area of 170 m<sup>2</sup>/g with a void fraction of 0.43 (**Figure 9.2**).<sup>23</sup> The calcined, spin-coated films were found to have thickness of ca. 400 nm, as measured by profilometry and SIMS. After calcination, a 10 mg/mL solution of DPP(TBFu)<sub>2</sub> dissolved in chloroform was then spin-coated onto the TiO<sub>2</sub> film. The hybrid film was then annealed at 130 °C before characterizations.

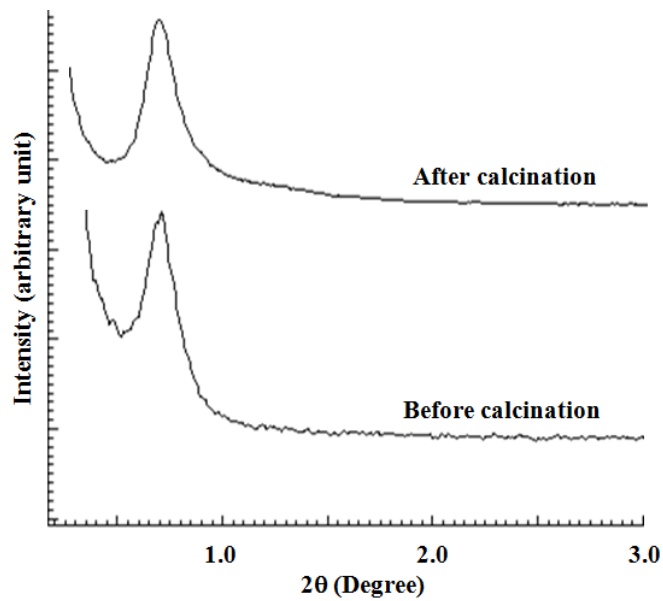


Figure 9.1. SAXS patterns of mesostructured TiO<sub>2</sub> film (a) before and (b) after calcinations.

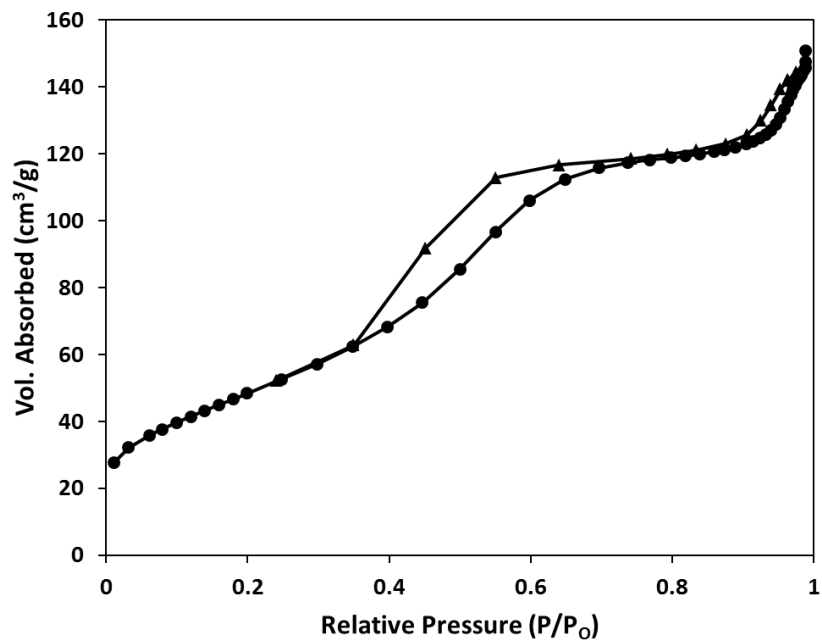
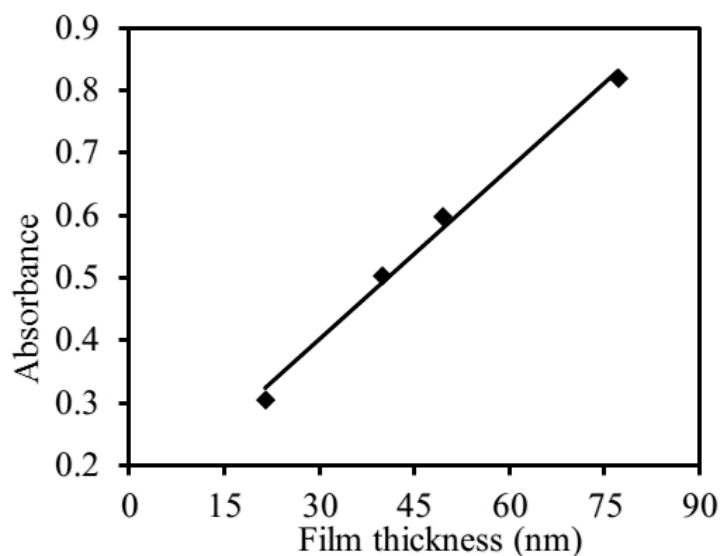


Figure 9.2. Nitrogen adsorption (circles) and desorption (triangles) isotherms of mesostructured TiO<sub>2</sub> film, measured using a TriStar 3000 Micromeritics Gas Absorption Analyzer.

### Loading calculation of absorption method

A series of neat DPP(TBFu)<sub>2</sub> films at different thicknesses were prepared by spin-coating DPP(TBFu)<sub>2</sub> solutions at different concentration on glass substrate. The absorbance of these films at 600 nm (maximum absorption wavelength) was plotted against their thicknesses to get a calibration curve, presented in **Figure 9.3**. The relative thickness of DPP(TBFu)<sub>2</sub> in hybrid TiO<sub>2</sub>-DPP(BTFu)<sub>2</sub> films was extrapolated by fitting its absorbance at 600 nm to the calibration curve. The average relative thickness of DPP(TBFu)<sub>2</sub> was 43.9 nm. The average thickness of hybrid film was 400 nm, with its void volume having an equivalent thickness of 400 nm × 0.43 (void fraction) = 172 nm. The loading is  $(43.9/172) \times 100=25\%$  of the pore volume.



**Figure 9.3.** Calibration curve of absorbance at 600 nm at different thicknesses of neat DPP(TBFu)<sub>2</sub> films.



## Loading calculation by SIMS method

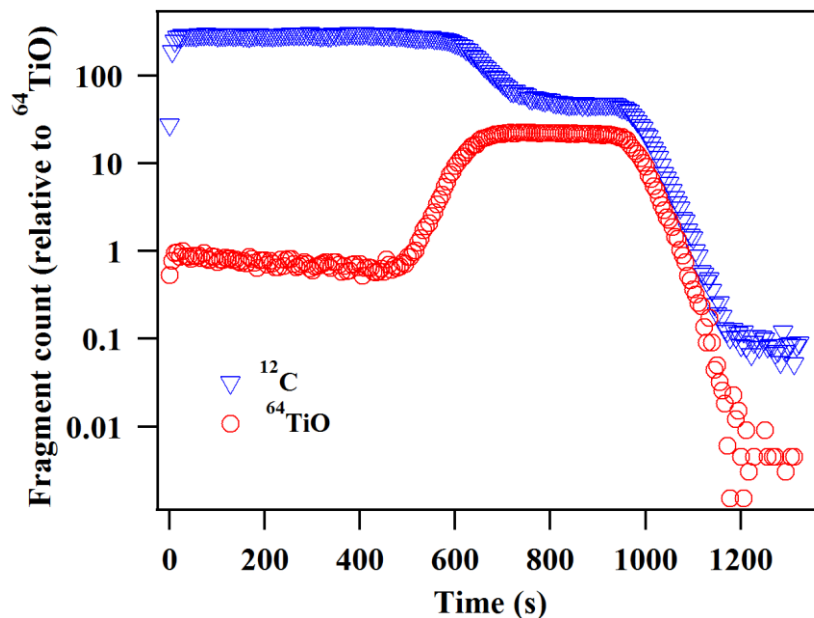


**Figure 9.4. SIMS traces of hybrid  $\text{TiO}_2$ -DPP(TBFu) $_2$  drop-cast film.**

In this method, we drop-casted the small molecule solution on mesostructured  $\text{TiO}_2$  films and characterized it by SIMS. Drop-casting results in a neat small molecule layer formed on top of hybrid layer. The  $^{12}\text{C}$  intensity is much higher than  $^{64}\text{TiO}$  for the top surface which comprises of mostly DPP(TBFu) $_2$  (**Figure 9.4**). As it reaches to the interface of the hybrid layer,  $^{12}\text{C}$  intensity drops and  $^{64}\text{TiO}$  intensity enhances significantly. The  $^{12}\text{C}$  signal from the hybrid layer is 12% of its signal from neat top layer. By assuming the etching rate among different elements is similar, we conclude that DPP(TBFu) $_2$  comprised of 12 vol. % of the hybrid film, corresponding to an overall loading of approximately 29% of the total  $\text{TiO}_2$  pore volume ( $=12/0.43$ , the void fraction of the mesostructured  $\text{TiO}_2$  film).

### 9.2.3. Results and Discussions

Dynamic secondary ion mass spectrometry (SIMS) was used to characterize the infiltration depth and uniformity of DPP(TBFu)<sub>2</sub> within the mesostructured TiO<sub>2</sub> films. Elemental fragments of the film are ejected from the sputtering of the sample by primary ion beam; and detected by a mass spectrometer as a function of time. The depth-profiling traces of different m/z fragments are shown in **Figure 9.5**.

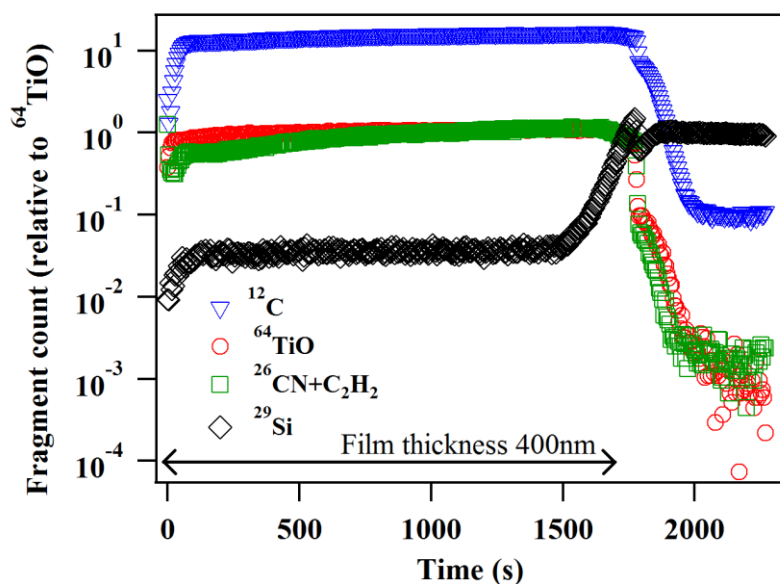


**Figure 9.5. SIMS traces of a hybrid TiO<sub>2</sub>-DPP(TBFu)<sub>2</sub> spin-coat film. The arrow indicates the approximate film thickness up to the interface determined by profilometry after the SIMS measurements.**

The m/z at 12, 26, 29 and 64 represent C, CN+C<sub>2</sub>H<sub>2</sub>, Si and TiO, respectively (hereafter <sup>12</sup>C, <sup>26</sup>CN, <sup>29</sup>Si and <sup>64</sup>TiO). The <sup>12</sup>C and <sup>26</sup>CN signals are attributed to DPP(TBFu)<sub>2</sub> in the hybrid film while <sup>64</sup>TiO arises from the mesostructured TiO<sub>2</sub>, and <sup>29</sup>Si is from glass substrate. It is clear that the relative counts from <sup>12</sup>C, <sup>26</sup>CN, and <sup>64</sup>TiO remain constant until the interface with glass substrate is reached, at which point the <sup>29</sup>Si count significantly

increases. This demonstrates that DPP(TBFu)<sub>2</sub> was infiltrated uniformly (within the sensitivity of the measurement) throughout the mesostructured TiO<sub>2</sub> film. This is a significant improvement compared to polymers, which usually efficiently infiltrate only after surface-modification of TiO<sub>2</sub>.<sup>9,10</sup> As a result, all of the surface area of the mesostructured TiO<sub>2</sub> is expected to be available to form heterojunctions with DPP(TBFu)<sub>2</sub>, which is vital for charge separation.

A high loading of DPP(TBFu)<sub>2</sub> is as important as achieving uniform and deep infiltration because DPP(TBFu)<sub>2</sub> is the only visible-light absorber in this hybrid structure. We quantify the loading of DPP(TBFu)<sub>2</sub> in mesoporous TiO<sub>2</sub> by means of film absorption and SIMS. In the absorption method, the loading of DPP(TBFu)<sub>2</sub> was estimated to be around 25% of total TiO<sub>2</sub> pore volume, by comparing the optical density at maximum absorption wavelength of hybrid TiO<sub>2</sub>-DPP(TBFu)<sub>2</sub> film to that of a series of known-thickness neat DPP(TBFu)<sub>2</sub> films (section 9.2.2).<sup>23</sup> In the other method, we drop-casted the small molecule solution on mesostructured TiO<sub>2</sub> film and characterized it by SIMS. Drop-casting results in a neat small molecule layer formed on top of hybrid layer. By comparing the <sup>12</sup>C intensity from the top neat DPP(TBFu)<sub>2</sub> layer and the hybrid layer, we estimated the loading of DPP(TBFu)<sub>2</sub> to be around 29% of the total TiO<sub>2</sub> pore volume (section 9.2.2).<sup>23</sup> The higher loading of DPP(TBFu)<sub>2</sub> in the drop-cast film relative to the spin-cast film is likely, because drop-casting allows the molecules to infiltrate into the mesopores for a longer time compared to the spin-cast film. This is a notable result, given that the loading of polymer reported in literature without further surface treatment of TiO<sub>2</sub> is less than 10%.<sup>9,10</sup> This validates our hypothesis that less hydrophobic small molecules in low viscosity solutions can be more easily introduced into hydrophilic mesoporous TiO<sub>2</sub> films and with significantly higher loadings than polymeric molecules.

Having established the excellent infiltration and loading of DPP(TBFu)<sub>2</sub> into mesostructured TiO<sub>2</sub>, we now consider optical and electrical characterization of the hybrid TiO<sub>2</sub>-DPP(TBFu)<sub>2</sub> film. Firstly, the absorption spectra of neat DPP(TBFu)<sub>2</sub> and hybrid films are comparable (**Figure 9.6**),<sup>23</sup> suggesting that there is no chemical change of DPP(TBFu)<sub>2</sub> in the hybrid film.

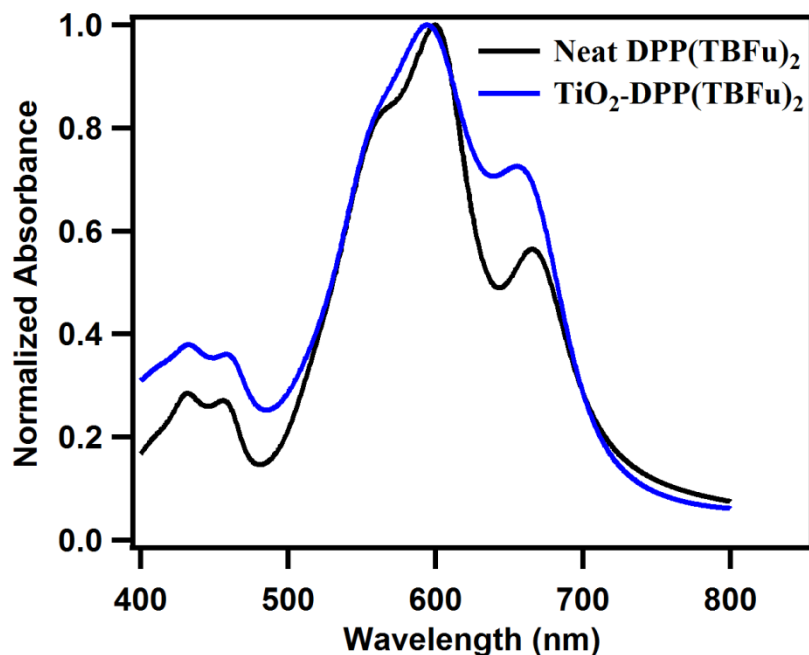


**Figure 9.6.** Absorption spectra of neat DPP(TBFu)<sub>2</sub> and hybrid TiO<sub>2</sub>-DPP(TBFu)<sub>2</sub>.

Steady-state and transient photoluminescence (PL) quenching were then used to probe the efficiency of charge transfer from DPP(TBFu)<sub>2</sub> to TiO<sub>2</sub> in the hybrid system, as these techniques have been widely used to establish the electron transfer from photo-excited conjugated polymer moieties to TiO<sub>2</sub>.<sup>24,25</sup> The steady-state PL of neat DPP(TBFu)<sub>2</sub> film and hybrid DPP(TBFu)<sub>2</sub> film of comparable optical density are shown in **Figure 9.7**. The PL quenching efficiency of DPP(TBFu)<sub>2</sub> by TiO<sub>2</sub> was estimated, from both the steady-state and transient PL, to be around 70%, reflecting efficient electron transfer from excited state DPP(TBFu)<sub>2</sub> to TiO<sub>2</sub>. Transient PL of neat DPP(TBFu)<sub>2</sub> (inset of Figure 9.7) exhibited

monoexponentially decaying intensity with a lifetime of 1.0 ns. By comparison, analogous measurements of transient PL intensity for a hybrid TiO<sub>2</sub>-DPP(TBFu)<sub>2</sub> film decayed biexponentially with two lifetimes of 230 ps and 1.0 ns. The former lifetime may reflect the excitons formed within their diffusion lengths near TiO<sub>2</sub> interface that are quenched immediately by electron transfer to TiO<sub>2</sub>. The latter lifetime corresponds to the excitons formed further away from TiO<sub>2</sub>, which decayed in local environments that are similar to those in neat DPP(TBFu)<sub>2</sub>. The PL quenching can likely be improved by adsorption of interfacial modifiers onto the TiO<sub>2</sub> surface, as has been demonstrated for other hybrid TiO<sub>2</sub>-conjugated polymer materials.<sup>7,9,11,14,15,26</sup>

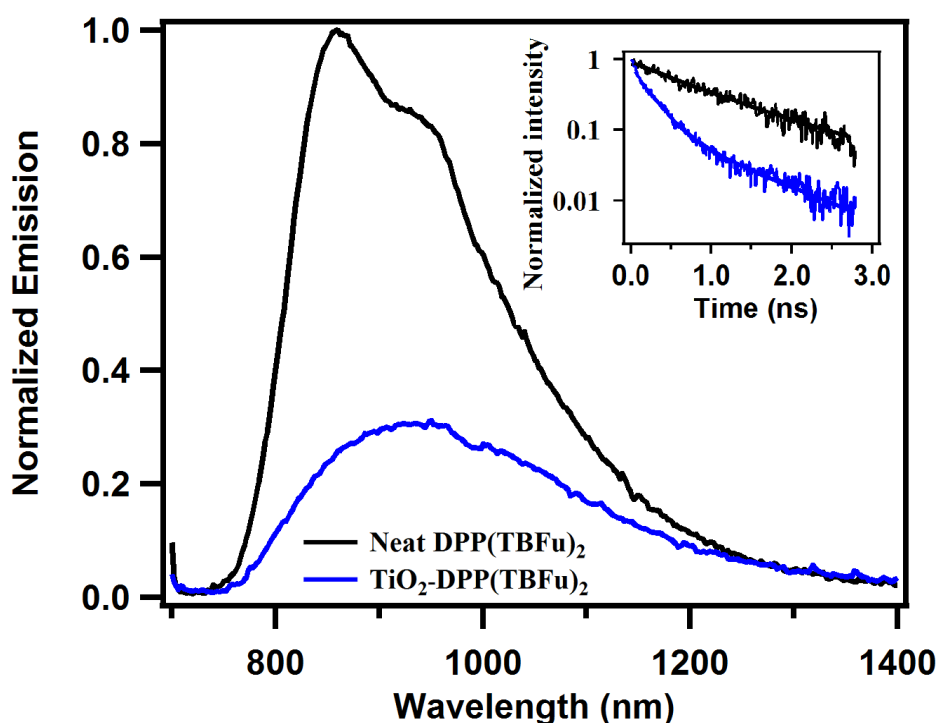


**Figure 9.7.** Steady-state photoluminescence and transient photoluminescence (the inset) of neat DPP(TBFu)<sub>2</sub> and hybrid TiO<sub>2</sub>-DPP(TBFu)<sub>2</sub>.

Conducting and photoconducting atomic force microscopy (c-AFM and pc-AFM, respectively) were employed to simultaneously probe morphology, charge extraction and photosensitivity of the hybrid TiO<sub>2</sub>-DPP(TBFu)<sub>2</sub> system. These are powerful techniques to characterize and correlate the nanoscale morphologies and electrical properties the film materials.<sup>19,27-29</sup> Hybrid TiO<sub>2</sub>-DPP(TBFu)<sub>2</sub> and TiO<sub>2</sub>-P3HT films were prepared by spin-coating the donor materials into mesostructured TiO<sub>2</sub> for c-AFM and pc-AFM characterization. Though the hybrid TiO<sub>2</sub>-P3HT system has been intensively studied, nanoscale electrical properties have not been investigated using c-AFM and pc-AFM. In our c-AFM experiments, the gold-coated silicon AFM tip is scanning the sample in contact mode, to map out topography and current images. The structure of the devices ITO/TiO<sub>2</sub>: DPP(TBFu)<sub>2</sub> or P3HT/Au-tip resembles the structure of hole-only diode devices, since the work function of Au (~5.1 eV) and ITO (~4.8 eV) is much closer to the HOMO of P3HT (~5.0 eV) and DPP(TBFu)<sub>2</sub> (~5.2 eV). As negative bias is applied to the ITO substrate, holes are injected from the Au tip and collected at the substrate. The pc-AFM experiment set-up is similar to c-AFM, except the fact that the sample is illuminated by a Xe-lamp light source with a light spot approximately 160 μm in diameter.<sup>19,30</sup>

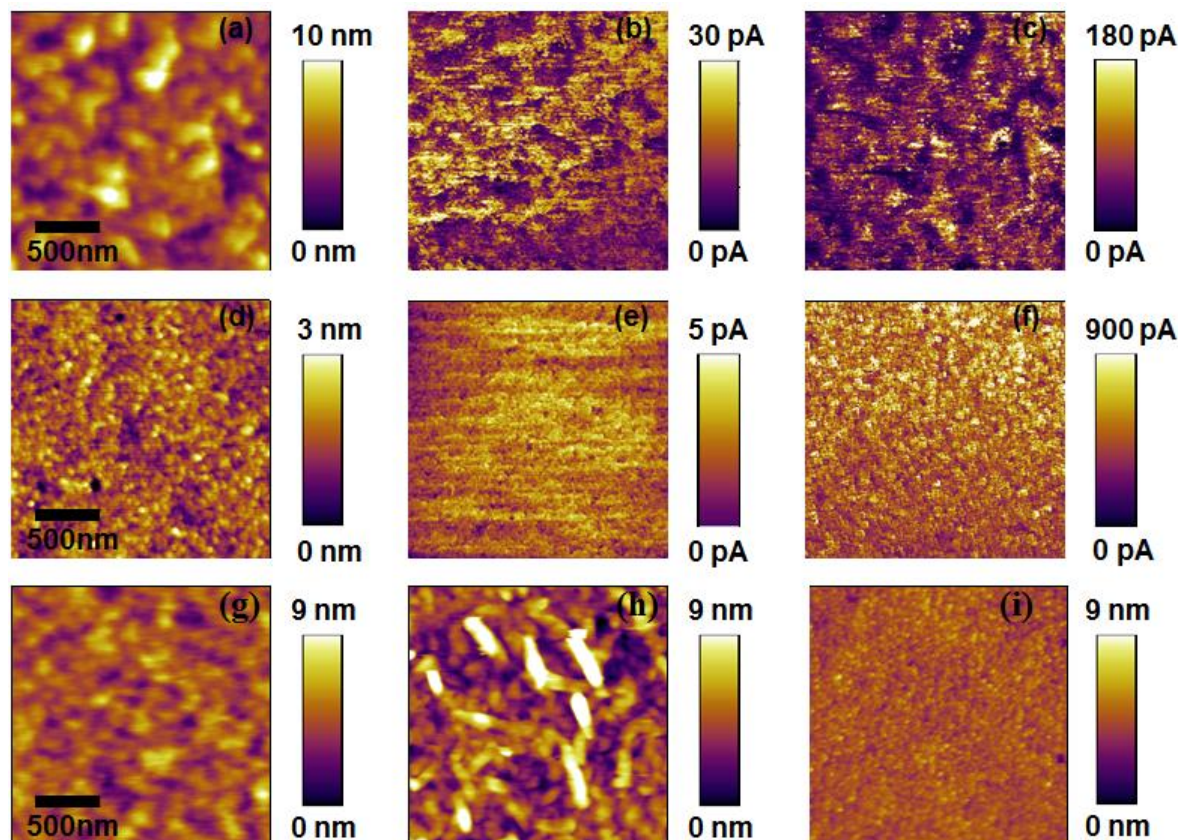


**Figure 9.8.** (a-f) Surface morphology, dark-current and photo-current images from conducting and photoconducting atomic force microscopy of (a, b, c) TiO<sub>2</sub>-P3HT film and (d, e, f) TiO<sub>2</sub>-DPP(TBFu)<sub>2</sub> film, respectively. (g-i) The morphology of neat P3HT (g), DPP(TBFu)<sub>2</sub> (h) and mesostructured TiO<sub>2</sub> (i).

**Figure 9.8** shows the morphology, dark conductivity and photoconductivity collected at the ITO bias of -3 V for TiO<sub>2</sub>-DPP(TBFu)<sub>2</sub> (a, b, c) and TiO<sub>2</sub>-P3HT (d, e, f). The surface morphology of TiO<sub>2</sub>-P3HT shows coarser features compared to that of TiO<sub>2</sub>-DPP(TBFu)<sub>2</sub>. While the TiO<sub>2</sub>-P3HT surface more closely resembles that of neat P3HT morphology (g), the TiO<sub>2</sub>-DPP(TBFu)<sub>2</sub> surface is more similar to that of TiO<sub>2</sub> (i). This suggests that more P3HT remains on top of TiO<sub>2</sub> surface as a neat P3HT layer. Compared to TiO<sub>2</sub>-P3HT, the dark and

photo-currents of the  $\text{TiO}_2\text{-DPP(TBFu)}_2$  hybrid are quite homogeneous throughout the surface, which can lead to more continuous conduction pathways for carrier transport in solar cells. Most interestingly, the increase from dark to photocurrent of  $\text{TiO}_2\text{-DPP(TBFu)}_2$  (e to f) is around 200 times while that of  $\text{TiO}_2\text{-P3HT}$  (b to c) is only around six times. It implies that the carrier density of  $\text{TiO}_2\text{-DPP(TBFu)}_2$  is much higher than that of  $\text{TiO}_2\text{-P3HT}$  under illumination. This can be attributed to the higher loading of  $\text{DPP(TBFu)}_2$  in the mesostructured  $\text{TiO}_2$  film and more efficient charge transfer between the two, resulting in more photo-generated carriers and hence higher photoconductivity. The intense photoresponse of  $\text{TiO}_2\text{-DPP(TBFu)}_2$  system suggests that this structure may be utilized in a hybrid photoconductor device. The further modification of  $\text{TiO}_2$  surface and/or using higher compatible small molecules can be utilized to improve the photocurrent at zero bias which is more relevant for solar cells operation.

#### 9.2.4. Conclusion

In summary, we have demonstrated an important step toward using hybrid  $\text{TiO}_2\text{-SM}$  in optoelectronic devices. Improved hybrid bulk-heterojunction materials was fabricated by spin-casting a benchmark conjugated small molecule,  $\text{DPP(TBFu)}_2$  into mesostructured  $\text{TiO}_2$ . Due to both a reduced molecular size and less hydrophobic nature of the conjugated molecules (relative to conjugated polymers), homogeneous and improved infiltration into the mesoporous  $\text{TiO}_2$  is achieved without the need for pre-treatment of the  $\text{TiO}_2$ . Remarkably, this small molecule can realize loadings of up to 25% of the total pore volume –  $2.5\times$  the typical loadings achieved for conjugated polymers. Charge transfer from photo-excited  $\text{DPP(TBFu)}_2$  to  $\text{TiO}_2$  is efficient and promising for solar cell and photoconductor applications. Both the loading and charge transfer efficiency could be further improved by



modifying TiO<sub>2</sub> surface and functionalizing small molecules so that they would interact with TiO<sub>2</sub> more favorably. Interestingly, the intense photoresponse of TiO<sub>2</sub>-DPP(TBFu)<sub>2</sub> hints to a high performance hybrid TiO<sub>2</sub>-SM photoconductors. In a broader context, with high loading, efficient charge transfer and intense photo-response, hybrid TiO<sub>2</sub>-SM system are useful for assessing the effects of interfacial interactions between TiO<sub>2</sub> and non-metal organic dyes on their optoelectronic properties. For instance, these properties and the relatively simple small molecular structure of SMs facilitate the use high resolution characterization technique, such as solid-state 2D NMR, to gain molecular-level understanding of the chemical composition and structure of inorganic-organic interface.<sup>20</sup>

#### 9.2.5. References

- (1) Takada, J., Awaji, H., Koshioka, M., Nakajima, A., and Nevin, W. A. (1992) Organic–inorganic multilayers: A new concept of optoelectronic material. *Appl. Phys. Lett.* *61*, 2184–2186.
- (2) Koichi Kajihara, Katsuhisa Tanaka, Kazuyuki Hirao, and Naohiro Soga. (1996) Photovoltaic Effect in Titanium Dioxide/Zinc Phthalocyanine Cell. *Jpn. J. Appl. Phys.* *35*, 6110–6116.
- (3) Koichi Kajihara, Katsuhisa Tanaka, Kazuyuki Hirao, and Naohiro Soga. (1997) Photovoltaic Effect in Titanium Dioxide/Polythiophene Cell. *Jpn. J. Appl. Phys.* *36*, 5537–5542.
- (4) Savenije, T. J., Warman, J. M., and Goossens, A. (1998) Visible light sensitisation of titanium dioxide using a phenylene vinylene polymer. *Chem. Phys. Lett.* *287*, 148–153.
- (5) van Hal, P. A., Christiaans, M. P. T., Wienk, M. M., Kroon, J. M., and Janssen, R. A. J. (1999) Photoinduced Electron Transfer from Conjugated Polymers to TiO<sub>2</sub>. *J Phys Chem B* *103*, 4352–4359.
- (6) O'Regan, B., and Grätzel, M. (1991) A low-cost, high-efficiency solar cell based on dye-sensitized colloidal TiO<sub>2</sub> films. *Nature* *353*, 737–740.

- (7) Yu, J., Shen, T., Weng, W., Huang, Y., Huang, C., Su, W., Rwei, S., Ho, K., and Wang, L. (2012) Molecular Design of Interfacial Modifiers for Polymer-Inorganic Hybrid Solar Cells. *Adv. Energy Mater.* 2, 245–252.
- (8) Lin, J. D. A., Mikhnenko, O. V., Chen, J., Masri, Z., Ruseckas, A., Mikhailovsky, A., Raab, R. P., Liu, J., Blom, P. W. M., Loi, M. A., García-Cervera, C. J., Samuel, I. D. W., and Nguyen, T.-Q. (2014) Systematic study of exciton diffusion length in organic semiconductors by six experimental methods. *Mater. Horiz.* 1, 280–285.
- (9) Abrusci, A., Ding, I.-K., Al-Hashimi, M., Segal-Peretz, T., McGehee, M. D., Heeney, M., Frey, G. L., and Snaith, H. J. (2011) Facile infiltration of semiconducting polymer into mesoporous electrodes for hybrid solar cells. *Energy Env. Sci* 4, 3051–3058.
- (10) Bartholomew, G. P., and Heeger, A. J. (2005) Infiltration of Regioregular Poly[2,2'-(3-hexylthiophene)] into Random Nanocrystalline TiO<sub>2</sub> Networks. *Adv. Funct. Mater.* 15, 677–682.
- (11) Moon, S.-J., Baranoff, E., Zakeeruddin, S. M., Yeh, C.-Y., Diau, E. W.-G., Grätzel, M., and Sivula, K. (2011) Enhanced light harvesting in mesoporous TiO<sub>2</sub>/P3HT hybrid solar cells using a porphyrin dye. *Chem Commun* 47, 8244–8246.
- (12) Gao, F., Ren, S., and Wang, J. (2013) The renaissance of hybrid solar cells: progresses, challenges, and perspectives. *Energy Environ. Sci.* 6, 2020–2040.
- (13) Xu, T., and Qiao, Q. (2011) Conjugated polymer–inorganic semiconductor hybrid solar cells. *Energy Env. Sci* 4, 2700–2720.
- (14) Zhu, R., Jiang, C., Liu, B., and Ramakrishna, S. (2009) Highly Efficient Nanoporous TiO<sub>2</sub>-Polythiophene Hybrid Solar Cells Based on Interfacial Modification Using a Metal-Free Organic Dye. *Adv. Mater.* 21, 994–1000.
- (15) Huang, Y.-C., Hsu, J.-H., Liao, Y.-C., Yen, W.-C., Li, S.-S., Lin, S.-T., Chen, C.-W., and Su, W.-F. (2011) Employing an amphiphilic interfacial modifier to enhance the performance of a poly(3-hexyl thiophene)/TiO<sub>2</sub> hybrid solar cell. *J. Mater. Chem.* 21, 4450.
- (16) Koster, L. J. A., Stenzel, O., Oosterhout, S. D., Wienk, M. M., Schmidt, V., and Janssen, R. A. J. (2013) Morphology and Efficiency: The Case of Polymer/ZnO Solar Cells. *Adv. Energy Mater.* 3, 615–621.

- (17) Ravirajan, P., Haque, S. A., Durrant, J. R., Bradley, D. D. C., and Nelson, J. (2005) The Effect of Polymer Optoelectronic Properties on the Performance of Multilayer Hybrid Polymer/TiO<sub>2</sub> Solar Cells. *Adv. Funct. Mater.* *15*, 609–618.
- (18) Walker, B., Tamayo, A. B., Dang, X., Zalar, P., Seo, J. H., Garcia, A., Tantiwiwat, M., and Nguyen, T. (2009) Nanoscale Phase Separation and High Photovoltaic Efficiency in Solution-Processed, Small-Molecule Bulk Heterojunction Solar Cells. *Adv. Funct. Mater.* *19*, 3063–3069.
- (19) Dang, X.-D., Tamayo, A. B., Seo, J., Hoven, C. V., Walker, B., and Nguyen, T.-Q. (2010) Nanostructure and Optoelectronic Characterization of Small Molecule Bulk Heterojunction Solar Cells by Photoconductive Atomic Force Microscopy. *Adv. Funct. Mater.* *20*, 3314–3321.
- (20) Neyshadt, S., Jahnke, J. P., Messinger, R. J., Rawal, A., Segal Peretz, T., Huppert, D., Chmelka, B. F., and Frey, G. L. (2011) Understanding and Controlling Organic–Inorganic Interfaces in Mesostructured Hybrid Photovoltaic Materials. *J Am Chem Soc* *133*, 10119–10133.
- (21) Segal-Peretz, T., Leman, O., Nardes, A. M., and Frey, G. L. (2011) On the Origin of Charge Generation in Hybrid TiO<sub>x</sub>/Conjugated Polymer Photovoltaic Devices. *J Phys Chem C* *116*, 2024–2032.
- (22) Neyshadt, S., Kalina, M., and Frey, G. L. (2008) Self-Organized Semiconducting Polymer-Incorporated Mesostructured Titania for Photovoltaic Applications. *Adv. Mater.* *20*, 2541–2546.
- (23) See supplemental material at [URL will be inserted by AIP] for porosimetry data of mesostructured TiO<sub>2</sub> and loading calculation of DPP(TBFu)<sub>2</sub> in hybrid film.
- (24) van Hal, P. A., Wienk, M. M., Kroon, J. M., and Janssen, R. A. J. (2003) TiO<sub>2</sub> sensitized with an oligo(p-phenylenevinylene) carboxylic acid: a new model compound for a hybrid solar cell. *J. Mater. Chem.* *13*, 1054–1057.
- (25) Bouclé, J., Chyla, S., Shaffer, M. S. P., Durrant, J. R., Bradley, D. D. C., and Nelson, J. (2008) Hybrid Solar Cells from a Blend of Poly(3-hexylthiophene) and Ligand-Capped TiO<sub>2</sub> Nanorods. *Adv. Funct. Mater.* *18*, 622–633.
- (26) Liu, J., Kadnikova, E. N., Liu, Y., McGehee, M. D., and Fréchet, J. M. J. (2004) Polythiophene Containing Thermally Removable Solubilizing Groups Enhances the

Interface and the Performance of Polymer–Titania Hybrid Solar Cells. *J. Am. Chem. Soc.* *126*, 9486–9487.

(27) Douhéret, O., Lutsen, L., Swinnen, A., Bresselge, M., Vandewal, K., Goris, L., and Manca, J. (2006) Nanoscale electrical characterization of organic photovoltaic blends by conductive atomic force microscopy. *Appl. Phys. Lett.* *89*, 32107-32107–3.

(28) Coffey, D. C., Reid, O. G., Rodovsky, D. B., Bartholomew, G. P., and Ginger, D. S. (2007) Mapping Local Photocurrents in Polymer/Fullerene Solar Cells with Photoconductive Atomic Force Microscopy. *Nano Lett.* *7*, 738–744.

(29) He, Z., Phan, H., Liu, J., Nguyen, T.-Q., and Tan, T. T. Y. (2013) Understanding TiO<sub>2</sub> Size-Dependent Electron Transport Properties of a Graphene-TiO<sub>2</sub> Photoanode in Dye-Sensitized Solar Cells Using Conducting Atomic Force Microscopy. *Adv. Mater.* *25*, 6900–6904.

(30) Guide, M., Dang, X.-D., and Nguyen, T.-Q. (2011) Nanoscale Characterization of Tetrabenzoporphyrin and Fullerene-Based Solar Cells by Photoconductive Atomic Force Microscopy. *Adv. Mater.* *23*, 2313–2319.